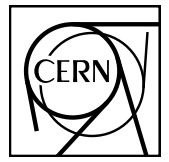


EUROPEAN ORGANIZATION FOR NUCLEAR RESEARCH



ALICE-ANA-2016-xxx
August 9, 2018

ΛK and ΞK Femtoscopy in Pb-Pb Collisions at $\sqrt{s_{NN}} = 2.76$ TeV from the LHC ALICE Experiment

Jesse T. Buxton¹

1. Department of Physics, The Ohio State University, Columbus, Ohio, USA

Email: jesse.thomas.buxton@cern.ch

Abstract

We present results from a femtoscopic analysis of ΛK and $\Xi^- K^\pm$ correlations in Pb-Pb collisions at $\sqrt{s_{NN}} = 2.76$ TeV by the ALICE experiment at the LHC. All pair combinations of Λ and $\bar{\Lambda}$ with K^+ , K^- and K_S^0 are analyzed. The femtoscopic correlations are the result of strong final-state interactions, and are fit with a parametrization based on a model by R. Lednicky and V. L. Lyuboshitz [1]. This allows us to both characterize the emission source and measure the scattering parameters for the particle pairs. We observe a large difference in the $\Lambda K^+ (\bar{\Lambda} K^-)$ and $\Lambda K^- (\bar{\Lambda} K^+)$ correlations in pairs with low relative momenta ($k^* \lesssim 100$ MeV). The results suggest an effect arising from different quark-antiquark interactions in the pairs, i.e. $s\bar{s}$ in $\Lambda K^+ (\bar{\Lambda} K^-)$ and $u\bar{u}$ in $\Lambda K^- (\bar{\Lambda} K^+)$, or from different net strangeness for each system. To gain further insight into this hypothesis, we currently are conducting a ΞK femtoscopic analysis.

Contents

1	Introduction	6
2	Data Sample and Software	6
2.1	Data Sample	6
2.2	Software	6
3	Data Selection	6
3.1	Event Selection and Mixing	6
3.2	K^\pm Track Selection	7
3.3	V0 Selection	8
3.3.1	Λ Reconstruction	9
3.3.2	K_S^0 Reconstruction	11
3.3.3	V0 Purity Background Estimation	13
3.4	Ξ Reconstruction	14
3.5	Pair Selection	16
4	Correlation Functions	20
4.1	Typical Correlation Function Construction	20
4.2	Stavinsky Correlation Function Construction	22
5	Fitting	25
5.1	Model: ΛK_S^0 , ΛK^\pm , $\Xi^- K_S^0$	25
5.2	Model: $\Xi^- K^\pm$	25
5.3	Momentum Resolution Corrections	26
5.4	Residual Correlations	31
5.5	Non-Flat Background	38
5.6	LednickyFitter	41
5.7	Coulomb Fitter	44
6	Systematic Errors	45
6.1	Systematic Errors: ΛK_S^0	45
6.1.1	Particle and Pair Cuts	45
6.1.2	Non-Flat Background	45
6.1.3	Fit Range	45

6.2	Systematic Errors: ΛK^\pm	46
6.2.1	Particle and Pair Cuts	46
6.2.2	Non-Flat Background	46
6.2.3	Fit Range	46
6.3	Systematic Errors: ΞK^\pm	46
6.3.1	Particle and Pair Cuts	46
7	Results and Discussion	48
7.1	Results: ΛK_S^0 and ΛK^\pm	48
7.1.1	Results: ΛK_S^0 and ΛK^\pm : No Residual Correlations Included in Fit	50
7.1.2	Results: ΛK_S^0 and ΛK^\pm : 3 Residual Correlations Included in Fit	56
7.1.3	Results: ΛK_S^0 and ΛK^\pm : 10 Residual Correlations Included in Fit	63
7.1.4	Results: ΛK_S^0 and ΛK^\pm : Fit Method Comparisons	70
7.2	Results: ΞK^\pm	75
8	To Do	76
9	Additional Figures	81
9.1	Residuals	81
9.1.1	ΛK^+ Residuals	81
9.1.2	ΛK^- Residuals	87
9.1.3	ΛK_S^0 Residuals	93

List of Figures

1	V0 Reconstruction	9
2	K_S^0 contamination in $\Lambda(\bar{\Lambda})$ collection	10
3	Λ and $\bar{\Lambda}$ Purity	11
4	$\Lambda(\bar{\Lambda})$ contamination in K_S^0 collection	12
5	K_S^0 Purity	13
6	V0 Purity Background Estimation	14
7	Ξ Reconstruction	16
8	$\Xi^-(\bar{\Xi}^+)$ Purity	16
9	Average Separation of $\Lambda(\bar{\Lambda})$ and K_S^0 Daughters	18
10	Average Separation of $\Lambda(\bar{\Lambda})$ Daughter and K^\pm	18
11	Average Separation of Ξ Daughters and K^\pm	19
12	ΛK Correlation Functions	21
13	Correlation Functions: ΛK^+ vs ΛK^- for 0-10% Centrality	21
14	ΛK Stavinsky Correlation Functions (Correct)	23
15	ΛK Stavinsky Correlation Functions (Correct and Incorrect)	24
16	Momentum Resolution: Sample k_{True}^* vs. k_{Rec}^*	27
17	Particle Contaminations Visible in k_{True}^* vs. k_{Rec}^*	28
18	Momentum Resolution Corrections: Methods Comparison	30
19	Residual Contributions Cartoon	31
20	Sample Transform Matrices for ΛK^+ Analysis	32
21	Sample Transform Matrices for $\bar{\Lambda} K^+$ Analysis	33
22	$\Sigma^0 K^+$ Transform	36
23	ΛK^{*0} Transform	37
24	Compare Non-Femtoscopic Backgrounds	38
25	Backgrounds with THERMINATOR, K_S^0 Tweak	39
26	Backgrounds with THERMINATOR	40
27	Correlation with background decomposition (THERM)	41
28	Background reduction methods with THERMINATOR	42
29	Extracted Scattering Parameters: 3 Residuals in Fit	49
30	Extracted Scattering Parameters: No Residuals in Fit	50
31	m_T Scaling of Radii: No Residuals in Fit	51
32	$\Lambda K_S^0(\bar{\Lambda} K_S^0)$ Fits with No Residuals	52

33	$\Lambda K^+(\bar{\Lambda}K^-)$ Fits, with NO residual correlations included, with No Residuals	53
34	$\Lambda K^-(\bar{\Lambda}K^+)$ Fits with No Residuals	54
35	Extracted Scattering Parameters: 3 Residuals in Fit	56
36	m_T Scaling of Radii: 3 Residuals in Fit	56
37	$\Lambda(\bar{\Lambda})K_S^0$ Fits with 3 Residuals	57
38	$\Lambda K^+(\bar{\Lambda}K^-)$ Fits with 3 Residuals	58
39	$\Lambda K^-(\bar{\Lambda}K^+)$ Fits with 3 Residuals	59
40	$\Lambda(\bar{\Lambda})K_S^0$ Fits showing 3 Residuals	60
41	$\Lambda K^+(\bar{\Lambda}K^-)$ and $\Lambda K^-(\bar{\Lambda}K^+)$ Fits with 3 Residuals	61
42	Extracted Scattering Parameters: 3 Residuals in Fit	63
43	m_T Scaling of Radii: 10 Residuals in Fit	63
44	$\Lambda K_S^0(\bar{\Lambda}K_S^0)$ Fits with 10 Residuals	64
45	$\Lambda K^+(\bar{\Lambda}K^-)$ Fits with 10 Residuals	65
46	$\Lambda K^-(\bar{\Lambda}K^+)$ Fits with 10 Residuals	66
47	$\Lambda(\bar{\Lambda})K_S^0$ Fits showing 10 Residuals	67
48	$\Lambda K^+(\bar{\Lambda}K^-)$ and $\Lambda K^-(\bar{\Lambda}K^+)$ Fits with 10 Residuals	68
49	Compare Fit Parameters: Background treatment	70
50	Compare Fit Parameters: Number of residuals	71
51	Compare Fit Parameters: Free vs fixed λ	72
52	Compare Fit Parameters: Shared vs unique λ	73
53	Compare Fit Parameters: Shared vs. Separate Radii	74
54	ΞK^\pm Results	75
55	ΞK^\pm Data with Coulomb-Only Bands, 0-10% Centrality	76
56	Effect of Strong Force Inclusion on Coulomb-Only Curve for ΞK^\pm systems	77
57	ΞK^\pm Global Coulomb-Only Fit (Set 1)	78
58	ΞK^\pm Global Coulomb-Only Fit (Set 2)	79
59	$\Xi^- K^+$ Coulomb-Only Fit	79
60	$\Xi^- K^-$ Coulomb-Only Fit	80
61	Residuals: $\Sigma^0 K^+$ to ΛK^+ (0-10% Centrality)	81
62	Residuals: $\Xi^0 K^+$ to ΛK^+ (0-10% Centrality)	82
63	Residuals: $\Xi^- K^+$ to ΛK^+ (0-10% Centrality)	82
64	Residuals: $\Sigma^{*+} K^+$ to ΛK^+ (0-10% Centrality)	83
65	Residuals: $\Sigma^{*-} K^+$ to ΛK^+ (0-10% Centrality)	83

66	Residuals: $\Sigma^{*0} K^+$ to ΛK^+ (0-10% Centrality)	84
67	Residuals: ΛK^{*0} to ΛK^+ (0-10% Centrality)	84
68	Residuals: $\Sigma^0 K^{*0}$ to ΛK^+ (0-10% Centrality)	85
69	Residuals: $\Xi^0 K^{*0}$ to ΛK^+ (0-10% Centrality)	85
70	Residuals: $\Xi^- K^{*0}$ to ΛK^+ (0-10% Centrality)	86
71	Residuals: $\Sigma^0 K^-$ to ΛK^- (0-10% Centrality)	87
72	Residuals: $\Xi^0 K^-$ to ΛK^- (0-10% Centrality)	88
73	Residuals: $\Xi^- K^-$ to ΛK^- (0-10% Centrality)	88
74	Residuals: $\Sigma^{*+} K^-$ to ΛK^- (0-10% Centrality)	89
75	Residuals: $\Sigma^{*-} K^-$ to ΛK^- (0-10% Centrality)	89
76	Residuals: $\Sigma^{*0} K^-$ to ΛK^- (0-10% Centrality)	90
77	Residuals: $\Lambda \bar{K}^{*0}$ to ΛK^- (0-10% Centrality)	90
78	Residuals: $\Sigma^0 \bar{K}^{*0}$ to ΛK^- (0-10% Centrality)	91
79	Residuals: $\Xi^0 \bar{K}^{*0}$ to ΛK^- (0-10% Centrality)	91
80	Residuals: $\Xi^- \bar{K}^{*0}$ to ΛK^- (0-10% Centrality)	92
81	Residuals: $\Sigma^0 K_S^0$ to ΛK_S^0 (0-10% Centrality)	93
82	Residuals: $\Xi^0 K_S^0$ to ΛK_S^0 (0-10% Centrality)	94
83	Residuals: $\Xi^- K_S^0$ to ΛK_S^0 (0-10% Centrality)	94
84	Residuals: $\Sigma^{*+} K_S^0$ to ΛK_S^0 (0-10% Centrality)	95
85	Residuals: $\Sigma^{*-} K_S^0$ to ΛK_S^0 (0-10% Centrality)	95
86	Residuals: $\Sigma^{*0} K_S^0$ to ΛK_S^0 (0-10% Centrality)	96
87	Residuals: ΛK^{*0} to ΛK_S^0 (0-10% Centrality)	96
88	Residuals: $\Sigma^0 K^{*0}$ to ΛK_S^0 (0-10% Centrality)	97
89	Residuals: $\Xi^0 K^{*0}$ to ΛK_S^0 (0-10% Centrality)	97
90	Residuals: $\Xi^- K^{*0}$ to ΛK_S^0 (0-10% Centrality)	98

11 1 Introduction

12 We present results from a femtoscopic analysis of ΛK and $\Xi^- K^\pm$ correlations in Pb-Pb collisions at
 13 $\sqrt{s_{\text{NN}}} = 2.76$ TeV by the ALICE experiment at the LHC. All pair combinations of Λ and $\bar{\Lambda}$ with K^+ ,
 14 K^- and K_S^0 are analyzed. The femtoscopic correlations are the result of strong final-state interactions,
 15 and are fit with a parametrization based on a model by R. Lednicky and V. L. Lyuboshitz [1]. This
 16 allows us to both characterize the emission source and measure the scattering parameters for the particle
 17 pairs. We observe a large difference in the $\Lambda K^+(\bar{\Lambda} K^-)$ and $\Lambda K^-(\bar{\Lambda} K^+)$ correlations in pairs with low
 18 relative momenta ($k^* \lesssim 100$ MeV). The results suggest an effect arising from different quark-antiquark
 19 interactions in the pairs, i.e. $s\bar{s}$ in $\Lambda K^+(\bar{\Lambda} K^-)$ and $u\bar{u}$ in $\Lambda K^-(\bar{\Lambda} K^+)$, or from different net strangeness for
 20 each system. To gain further insight into this hypothesis, we currently are conducting a ΞK femtoscopic
 21 analysis.

22 2 Data Sample and Software

23 2.1 Data Sample

24 The analysis used “pass 2” reconstructed Pb-Pb data from LHC11h (AOD145). The runlist was selected
 25 from runs with global quality tag “1” in the ALICE Run Condition Table. Approximately 40 million
 26 combined central, semi-central, and minimum bias events were analyzed. Runs from both positive (++)
 27 and negative (--) magnetic field polarity settings were used.

28 Run list: 170593, 170572, 170388, 170387, 170315, 170313, 170312, 170311, 170309, 170308, 170306,
 29 170270, 170269, 170268, 170230, 170228, 170207, 170204, 170203, 170193, 170163, 170159, 170155,
 30 170091, 170089, 170088, 170085, 170084, 170083, 170081, 170040, 170027, 169965, 169923, 169859,
 31 169858, 169855, 169846, 169838, 169837, 169835, 169591, 169590, 169588, 169587, 169586, 169557,
 32 169555, 169554, 169553, 169550, 169515, 169512, 169506, 169504, 169498, 169475, 169420, 169419,
 33 169418, 169417, 169415, 169411, 169238, 169167, 169160, 169156, 169148, 169145, 169144, 169138,
 34 169099, 169094, 169091, 169045, 169044, 169040, 169035, 168992, 168988, 168826, 168777, 168514,
 35 168512, 168511, 168467, 168464, 168460, 168458, 168362, 168361, 168342, 168341, 168325, 168322,
 36 168311, 168310, 168115, 168108, 168107, 168105, 168076, 168069, 167988, 167987, 167985, 167920,
 37 167915

38 Analysis was also performed on the LHC12a17a_fix (AOD149) Monte Carlo HIJING events for certain
 39 checks. THERMINATOR2 was also used for certain aspects, such as generation of transform matrices
 40 describing feed-down contributions, estimation of λ parameters, and non-femtoscopic background
 41 modeling.

42 2.2 Software

43 The analysis was performed on the PWGCF analysis train using AliRoot v5-09-29-1 and AliPhysics
 44 vAN-20180505-1.

45 The main classes utilized include: AliFemtoVertexMultAnalysis, AliFemtoEventCutEstimators, AliFem-
 46 toESDTrackCutNSigmaFilter, AliFemtoV0TrackCutNSigmaFilter, AliFemtoXiTrackCut, AliFemtoV0PairCut,
 47 AliFemtoV0TrackPairCut, AliFemtoXiTrackPairCut, and AliFemtoAnalysisLambdaKaon. All of these
 48 classes are contained in /AliPhysics/PWGCF/FEMTOSCOPY/AliFemto and .../AliFemtoUser.

49 3 Data Selection

50 3.1 Event Selection and Mixing

51 The events used in this study were selected with the class AliFemtoEventCutEstimators according to the
 52 following criteria:

- 53 – Triggers
- 54 – minimum bias (kMB)
- 55 – central (kCentral)
- 56 – semi-central (kSemiCentral)
- 57 – z-position of reconstructed event vertex must be within 10 cm of the center of the ALICE detector
- 58 – the event must contain at least one particle of each type from the pair of interest
- 59 The event mixing was handled by the AliFemtoVertexMultAnalysis class, which only mixes events with
- 60 like vertex position and centrality. The following criteria were used for event mixing:
- 61 – Number of events to mix = 5
- 62 – Vertex position bin width = 2 cm
- 63 – Centrality bin width = 5
- 64 The AliFemtoEventReaderAODChain class is used to read the events. Event flattening is not currently
- 65 used. FilterBit(7). The centrality is determined by the “V0M” method of AliCentrality, set by calling
- 66 AliFemtoEventReaderAOD::SetUseMultiplicity(kCentrality). We utilize the SetPrimaryVertexCorrec-
- 67 tionTPCPoints switch, which causes the reader to shift all TPC points to be relative to the event vertex.
- 68 **3.2 K[±] Track Selection**
- 69 Charged kaons are identified using the AliFemtoESDTrackCutNSigmaFilter class. The specific cuts used
- 70 in this analysis are as follows:
- 71 Track Selection:
- 72 – Kinematic range:
- 73 – $0.14 < p_T < 1.5 \text{ GeV}/c$
- 74 – $|\eta| < 0.8$
- 75 – FilterBit(7)
- 76 – TPC tracks
- 77 – Track Quality
- 78 – Minimum number of clusters in the TPC (fminTPCncls) = 80
- 79 – Maximum allowed χ^2/N_{DOF} for ITS clusters = 3.0
- 80 – Maximum allowed χ^2/N_{DOF} for TPC clusters = 4.0
- 81 – Primary Particle Selection:
- 82 – Maximum XY impact parameter = 2.4 cm
- 83 – Maximum Z impact parameter = 3.0 cm
- 84 – Remove particles with any kink labels (fRemoveKinks = true)
- 85 – Maximum allowed sigma to primary vertex (fMaxSigmaToVertex) = 3.0

86 K $^\pm$ Identification:

87 – PID Probabilities:

- 88 – K: > 0.2
- 89 – π : < 0.1
- 90 – μ : < 0.8
- 91 – p: < 0.1

92 – Most probable particle type must be Kaon (fMostProbable=3)

93 – TPC and TOF N $_\sigma$ cuts:

- 94 – $p < 0.4 \text{ GeV}/c$: N $_{\sigma K, \text{TPC}} < 2$
- 95 – $0.4 < p < 0.45 \text{ GeV}/c$: N $_{\sigma K, \text{TPC}} < 1$
- 96 – $0.45 < p < 0.8 \text{ GeV}/c$: N $_{\sigma K, \text{TPC}} < 3 \& N_{\sigma K, \text{TOF}} < 2$
- 97 – $0.8 < p < 1.0 \text{ GeV}/c$: N $_{\sigma K, \text{TPC}} < 3 \& N_{\sigma K, \text{TOF}} < 1.5$
- 98 – $p > 1.0 \text{ GeV}/c$: N $_{\sigma K, \text{TPC}} < 3 \& N_{\sigma K, \text{TOF}} < 1$

99 – Electron Rejection: Reject if N $_{\sigma e^-, \text{TPC}} < 3$

100 – Pion Rejection: Reject if:

- 101 – $p < 0.65 \text{ GeV}/c$
 - 102 * if TOF and TPC available: N $_{\sigma \pi, \text{TPC}} < 3 \& N_{\sigma \pi, \text{TOF}} < 3$
 - 103 * else
 - 104 · $p < 0.5 \text{ GeV}/c$: N $_{\sigma \pi, \text{TPC}} < 3$
 - 105 · $0.5 < p < 0.65 \text{ GeV}/c$: N $_{\sigma \pi, \text{TPC}} < 2$
- 106 – $0.65 < p < 1.5 \text{ GeV}/c$: N $_{\sigma \pi, \text{TPC}} < 5 \& N_{\sigma \pi, \text{TOF}} < 3$
- 107 – $p > 1.5 \text{ GeV}/c$: N $_{\sigma \pi, \text{TPC}} < 5 \& N_{\sigma \pi, \text{TOF}} < 2$

108 The purity of the K $^\pm$ collections was estimated using the HIJING MC data, for which the true identity
109 of each reconstructed K $^\pm$ particle is known. Therefore, the purity may be estimated as:

$$\text{Purity}(K^\pm) = \frac{N_{\text{true}}}{N_{\text{reconstructed}}} \quad (1)$$

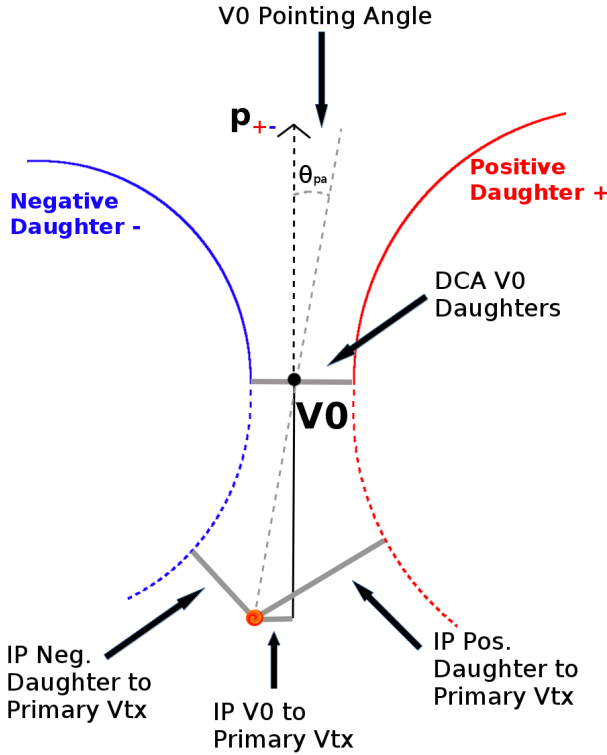
110 Purity(K $^+$) \approx Purity(K $^-$) \approx 97%

111 3.3 V0 Selection

112 $\Lambda(\bar{\Lambda})$ and K $_S^0$ are neutral particles which cannot be directly detected, but must instead be reconstructed
113 through detection of their decay products, or daughters. This process is illustrated in Figure 1. In
114 general, particles which are topologically reconstructed in this fashion are called V0 particles. The
115 class AliFemtoV0TrackCutNSigmaFilter (which is an extension of AliFemtoV0TrackCut) is used to
116 reconstruct the V0s.

117 In order to ensure a true and reliable signal, one must ensure good purity of the V0 collection. The purity
118 of the collection is calculated as:

$$\text{Purity} = \frac{\text{Signal}}{\text{Signal} + \text{Background}} \quad (2)$$

**Fig. 1:** V0 Reconstruction

119 To obtain both the signal and background, the invariant mass distribution (m_{inv}) of all V0 candidates must
 120 be constructed immediately before the final invariant mass cut. Examples of such distributions can be
 121 found in Figures 3 and 5. It is vital that the distribution be constructed immediately before the final m_{inv}
 122 cut, otherwise, it would be impossible to estimate the background. As demonstrated in Figures 3 and 5,
 123 the background is fit with a polynomial outside of the peak region of interest in order to extrapolate an
 124 estimate for the background within the region. Within the m_{inv} cut limits, the background is the region
 125 below the fit while the signal is the region above the fit.

126 3.3.1 **Λ Reconstruction**

127 The following cuts were used to select good $\Lambda(\bar{\Lambda})$ candidates:

128 1. Daughter Particle Cuts

129 (a) Cuts Common to Both Daughters

- 130 i. $|\eta| < 0.8$
- 131 ii. SetTPCnclsDaughters(80)
- 132 iii. SetStatusDaughters(AliESDtrack::kTPCrefit)
- 133 iv. DCA πp Daughters < 0.4 cm

134 (b) Pion Specific Daughter Cuts

- 135 i. $p_T > 0.16$ GeV/c
- 136 ii. DCA to prim vertex > 0.3 cm
- 137 iii. TPC and TOF N σ Cuts
 - 138 A. $p < 0.5$ GeV/c : N $\sigma_{\text{TPC}} < 3$
 - 139 B. $p > 0.5$ GeV/c :

- if TOF & TPC available: $N\sigma_{\text{TPC}} < 3$ & $N\sigma_{\text{TOF}} < 3$
- else $N\sigma_{\text{TOF}} < 3$

142 (c) Proton Specific Daughter Cuts

- i. $p_T > 0.5(p)[0.3(\bar{p})] \text{ GeV}/c$
- ii. DCA to prim vertex $> 0.1 \text{ cm}$
- iii. TPC and TOF $N\sigma$ Cuts
 - A. $p < 0.8 \text{ GeV}/c : N\sigma_{\text{TPC}} < 3$
 - B. $p > 0.8 \text{ GeV}/c :$
 - if TOF & TPC available: $N\sigma_{\text{TPC}} < 3$ & $N\sigma_{\text{TOF}} < 3$
 - else $N\sigma_{\text{TOF}} < 3$

150 2. V0 Cuts

- (a) $|\eta| < 0.8$
- (b) $p_T > 0.4 \text{ GeV}/c$
- (c) $|m_{\text{inv}} - m_{\text{PDG}}| < 3.8 \text{ MeV}$
- (d) DCA to prim. vertex $< 0.5 \text{ cm}$
- (e) Cosine of pointing angle > 0.9993
- (f) OnFlyStatus = false
- (g) Decay Length $< 60 \text{ cm}$

155 3. Shared Daughter Cut for V0 Collection

- Iterate through V0 collection to ensure that no daughter is used in more than one V0 candidate

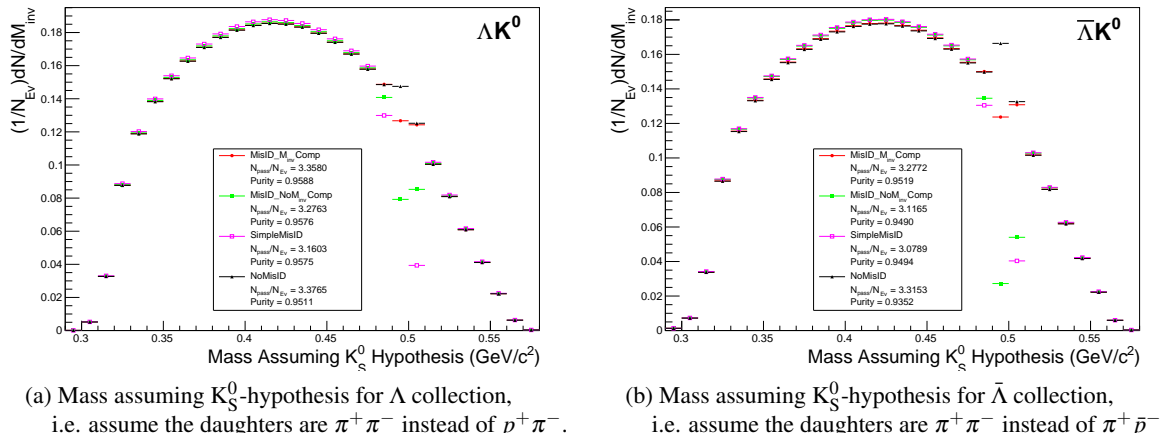


Fig. 2: Mass assuming K_S^0 -hypothesis for V0 candidates passing all Λ (2a) and $\bar{\Lambda}$ (2b) cuts. The “NoMisID” distribution (black triangles) uses the V0 finder without any attempt to remove misidentified K_S^0 . The slight peak in the “NoMisID” distribution around $m_{\text{inv}} = 0.5 \text{ GeV}/c^2$ contains misidentified K_S^0 particles in our $\Lambda(\bar{\Lambda})$ collection. “SimpleMisID” (pink squares) simply cuts out the entire peak, which throws away some good Λ and $\bar{\Lambda}$ particles. “MisID_NoM_{inv}Comp” (green squares) uses the misidentification cut outlined in the text, but does not utilize the final invariant mass comparison step. “MisID_M_{inv}Comp” (red circles) utilizes the full misidentification methods, and is currently used for this analysis. “ $N_{\text{pass}}/N_{\text{ev}}$ ” is the total number of $\Lambda(\bar{\Lambda})$ particles found, normalized by the total number of events. The purity of the collection is also listed.

Figure 2a shows the mass assuming K_S^0 hypothesis for the Λ collection, i.e. assume the daughters are $\pi^+\pi^-$ instead of $p^+\pi^-$. Figure 2b is a similar plot, but is for the $\bar{\Lambda}$ collection, i.e. assume the daughters are $\pi^+\pi^-$ instead of π^+p^- . The K_S^0 contamination is visible, although not profound, in both, in the slight peaks around $m_{\text{inv}} = 0.497 \text{ GeV}/c^2$. If one simply cuts out the entire peak, good Λ particles will be lost. Ideally, the Λ selection and K_S^0 misidentification cuts are selected such that the peak is removed from this plot while leaving the underlying distribution continuous. To attempt to remove these K_S^0 contaminations without throwing away good Λ and $\bar{\Lambda}$ particles, the following misidentification cuts are imposed; a $\Lambda(\bar{\Lambda})$ candidate is rejected if all of the following criteria are satisfied:

- $|m_{\text{inv}, K_S^0 \text{ Hypothesis}} - m_{\text{PDG}, K_S^0}| < 9.0 \text{ MeV}/c^2$
- Positive and negative daughters pass π daughter cut implemented for K_S^0 reconstruction
- $|m_{\text{inv}, K_S^0 \text{ Hypothesis}} - m_{\text{PDG}, K_S^0}| < |m_{\text{inv}, \Lambda(\bar{\Lambda}) \text{ Hypothesis}} - m_{\text{PDG}, \Lambda(\bar{\Lambda})}|$

Figure 3 shows the invariant mass (m_{inv}) distribution of all $\Lambda(\bar{\Lambda})$ candidates immediately before the final invariant mass cut. These distributions are used to calculate the collection purities. The Λ and $\bar{\Lambda}$ purities are found to be: $\text{Purity}(\Lambda) \approx \text{Purity}(\bar{\Lambda}) \approx 95\%$.

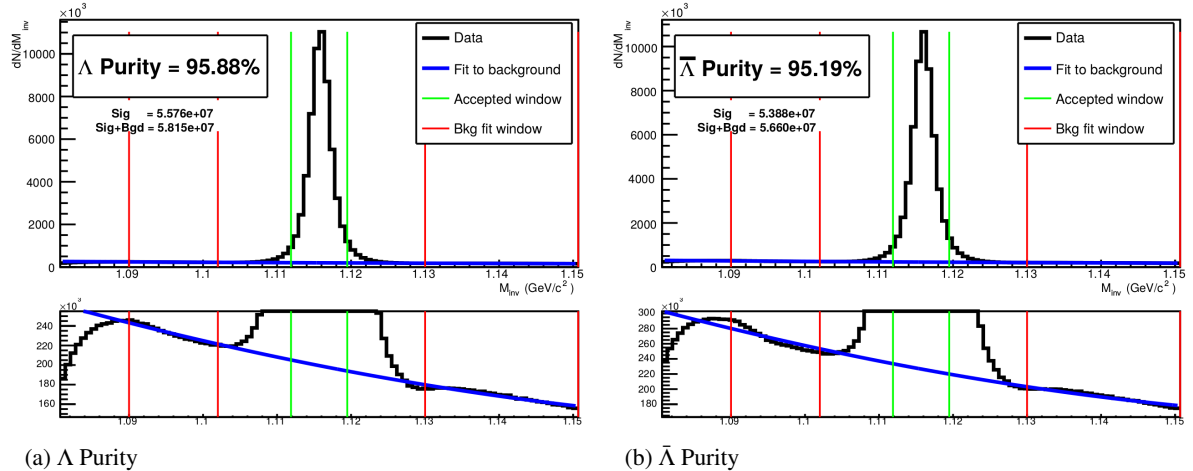


Fig. 3: Invariant mass (m_{inv}) distribution for all Λ (a) and $\bar{\Lambda}$ (b) candidates immediately before the final invariant mass cut. The bottom figures are zoomed to show the background with fit. The vertical green lines represent the m_{inv} cuts used in the analyses, the red vertical lines delineate the regions over which the background was fit, and the blue line shows the background fit. These distributions are used to calculate the collection purities, $\text{Purity}(\Lambda) \approx \text{Purity}(\bar{\Lambda}) \approx 95\%$.

3.3.2 K_S^0 Reconstruction

The following cuts were used to select good K_S^0 candidates:

1. Pion Daughter Cuts

- (a) $|\eta| < 0.8$
- (b) SetTPCnclsDaughters(80)
- (c) SetStatusDaughters(AliESDtrack::kTPCrefic)
- (d) DCA $\pi^+\pi^-$ Daughters $< 0.3 \text{ cm}$

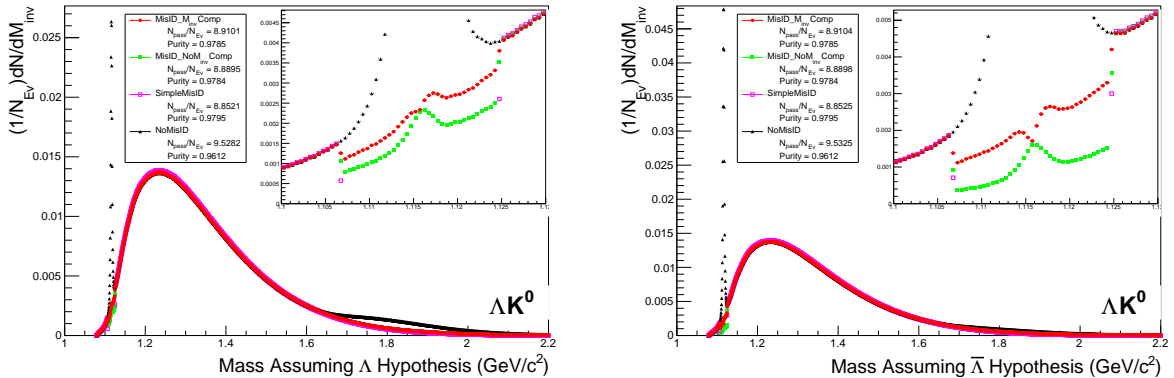
- (e) $p_T > 0.15 \text{ GeV}/c$
 (f) DCA to prim vertex $> 0.3 \text{ cm}$
 (g) TPC and TOF $N\sigma$ Cuts
 i. $p < 0.5 \text{ GeV}/c : N\sigma_{\text{TPC}} < 3$
 ii. $p > 0.5 \text{ GeV}/c :$
 – if TOF & TPC available: $N\sigma_{\text{TPC}} < 3 \& N\sigma_{\text{TOF}} < 3$
 – else $N\sigma_{\text{TOF}} < 3$

2. K_S^0 Cuts

- (a) $|\eta| < 0.8$
 (b) $p_T > 0.2 \text{ GeV}/c$
 (c) $m_{\text{PDG}} - 13.677 \text{ MeV} < m_{\text{inv}} < m_{\text{PDG}} + 2.0323 \text{ MeV}$
 (d) DCA to prim. vertex $< 0.3 \text{ cm}$
 (e) Cosine of pointing angle > 0.9993
 (f) OnFlyStatus = false
 (g) Decay Length $< 30 \text{ cm}$

3. Shared Daughter Cut for V0 Collection

- Iterate through V0 collection to ensure that no daughter is used in more than one V0 candidate



(a) Mass assuming Λ -hypothesis for K_S^0 collection, i.e. assume the daughters are $p^+ \pi^-$ instead of $\pi^+ \pi^-$.

(b) Mass assuming $\bar{\Lambda}$ -hypothesis for K_S^0 collection, i.e. assume the daughters are $\pi^+ \bar{p}^-$ instead of $\pi^+ \pi^-$.

Fig. 4: Mass assuming Λ -hypothesis (4a) and $\bar{\Lambda}$ -hypothesis (4b) for K_S^0 collection. The “NoMisID” distribution (black triangles) uses the V0 finder without any attempt to remove misidentified Λ and $\bar{\Lambda}$. The peak in the “NoMisID” distribution around $m_{\text{inv}} = 1.115 \text{ GeV}/c^2$ contains misidentified Λ (4a) and $\bar{\Lambda}$ (4b) particles in our K_S^0 collection. “SimpleMisID” (pink squares) simply cuts out the entire peak, which throws away some good K_S^0 particles. “MisID_NoM_{inv}Comp” (green squares) uses the misidentification cut outlined in the text, but does not utilize the final invariant mass comparison step. “MisID_M_{inv}Comp” (red circles) utilizes the full misidentification methods, and is currently used for this analysis. “ $N_{\text{pass}}/N_{\text{ev}}$ ” is the total number of K_S^0 particles found, normalized by the total number of events. The purity of the collection is also listed. Also note, the relative excess of the “NoMisID” distribution around $1.65 < m_{\text{inv}} < 2.1 \text{ GeV}/c^2$ shows misidentified $\bar{\Lambda}$ (4a) and Λ (4b) particles in our K_S^0 collection.

As can be seen in Figure 4, some misidentified Λ and $\bar{\Lambda}$ particles contaminate our K_S^0 sample. Figure 4a shows the mass assuming Λ -hypothesis for the K_S^0 collection, i.e. assume the daughters are $p^+ \pi^-$

instead of $\pi^+\pi^-$. Figure 4b is similar, but shows the mass assuming $\bar{\Lambda}$ -hypothesis for the collection, i.e. assume the daughters are $\pi^+\bar{p}^-$ instead of $\pi^+\pi^-$. The Λ contamination can be seen in 4a, and the $\bar{\Lambda}$ contamination in 4b, in the peaks around $m_{\text{inv}} = 1.115 \text{ GeV}/c^2$. Additionally, the $\bar{\Lambda}$ contamination is visible in Figure 4a, and the Λ contamination visible in Figure 4b, in the region of excess around $1.65 < m_{\text{inv}} < 2.1 \text{ GeV}/c^2$. This is confirmed as the number of misidentified Λ particles in the sharp peak of Figure 4a (misidentified $\bar{\Lambda}$ particles in the sharp peak of Figure 4b) approximately equals the excess found in the $1.65 < m_{\text{inv}} < 2.1 \text{ GeV}/c^2$ region of Figure 4a (Figure 4b).

The peaks around $m_{\text{inv}} = 1.115 \text{ GeV}/c^2$ in Figure 4 contain both misidentified $\Lambda(\bar{\Lambda})$ particles and good K_S^0 . If one simply cuts out the entire peak, some good K_S^0 particles will be lost. Ideally, the K_S^0 selection and $\Lambda(\bar{\Lambda})$ misidentification cuts can be selected such that the peak is removed from this plot while leaving the underlying distribution continuous. To attempt to remove these Λ and $\bar{\Lambda}$ contaminations without throwing away good K_S^0 particles, the following misidentification cuts are imposed; a K_S^0 candidate is rejected if all of the following criteria are satisfied (for either Λ - or $\bar{\Lambda}$ -hypothesis):

- $|m_{\text{inv}, \Lambda(\bar{\Lambda}) \text{ Hypothesis}} - m_{\text{PDG}, \Lambda(\bar{\Lambda})}| < 9.0 \text{ MeV}/c^2$
- Positive daughter passes $p^+(\pi^+)$ daughter cut implemented for $\Lambda(\bar{\Lambda})$ reconstruction
- Negative daughter passes $\pi^-(\bar{p}^-)$ daughter cut implemented by $\Lambda(\bar{\Lambda})$ reconstruction
- $|m_{\text{inv}, \Lambda(\bar{\Lambda}) \text{ Hypothesis}} - m_{\text{PDG}, \Lambda(\bar{\Lambda})}| < |m_{\text{inv}, K_S^0 \text{ Hypothesis}} - m_{\text{PDG}, K_S^0}|$

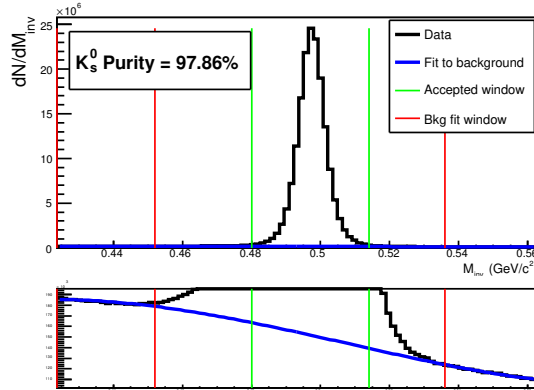


Fig. 5: Invariant mass (m_{inv}) distribution for all K_S^0 candidates immediately before the final invariant mass cut. The bottom figure is zoomed to show the background with fit. The vertical green lines represent the m_{inv} cut used in the analyses, the red vertical lines delineate the regions over which the background was fit, and the blue line shows the background fit. This distribution is used to calculate the collection purity, $\text{Purity}(K_S^0) \approx 98\%$.

3.3.3 V0 Purity Background Estimation

As previously stated, the backgrounds in the m_{inv} distributions are modeled by a polynomial which is fit outside of the final cut region in an attempt to estimate the background within the cut region. As this estimate of the background under the mass peak is vital for our estimate of our V0 purity, it is important for us to ensure that our estimate is accurate. More specifically, it is necessary that we ensure the background is well described by a polynomial fit within the cut region.

To better understand our background, we studied V0 candidates reconstructed with daughters from different events. These mixed-event V0s certainly do not represent real, physical V0s (a single V0 cannot have daughters living in two different events!), but, rather, represent a large portion of the background creeping into our analysis.

The standard AliFemto framework is not equipped to handle this situation, as most are not interested in these fake-V0s. Therefore, we built the AliFemtoV0PurityBgdEstimator class to handle our needs. In addition to finding fake-V0s using mixed-event daughters, we also used our AliFemtoV0PurityBgdEstimator class to find real-V0s using same-event daughters. The purpose here was to compare our simple V0 finder (in AliFemtoV0PurityBgdEstimator) to the established V0 finder used in standard AliFemto analyses.

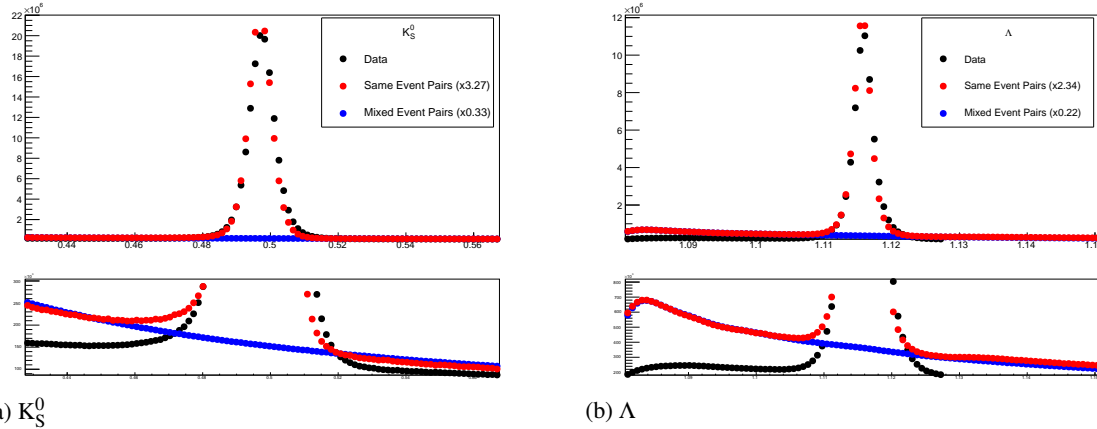


Fig. 6: V0 Purity Background Estimation. The black points, marked "Data", correspond to real V0s found using the standard V0-finder (i.e. the V0s used in my analyses). The red points, marked "Same Event Pairs", show real V0s reconstructed with our personal V0-finder in AliFemtoV0PurityBgdEstimator. These data are scaled by a factor (listed in the legend) to match their *Signal + Background* value in the cut region with that of the data. The blue points, marked "Mixed Event Pairs", show fake-V0s reconstructed with our personal V0-finder using mixed-event daughters. The blue points are scaled by a factor (listed in the legend) to closely match the red points in the side-band region.

Figure 6 shows the results of our study. In the figures, the black points, marked "Data", correspond to V0s found using the standard V0-finder, and to the V0s used in my analyses. The red points show real V0s reconstructed with our personal V0-finder (in AliFemtoV0PurityBgdEstimator) using same-event daughters, and the blue points show fake-V0s reconstructed with our personal V0-finder using mixed-event daughters. Both the red and blue points have been scaled by different factors (listed in the figure's legends) to nicely align all three data on a single plot.

Figure 6 shows that our personal V0-finder does a good, but not perfect, job of matching the shape of the m_{inv} plots obtained from the data. The scale factor listed in the legend reveals that we are only finding 1/3 - 1/2 of the V0s found by the standard V0-finder. These two points are not of concern, as our purpose here was to gain a sense of the broad shape of the background. It is revealed in Fig. 6, when studying the red and blue points, that the background distribution within the mass peak region is simply a smooth connection of the backgrounds outside of the cut region, as we assumed. Therefore, our method of fitting the background outside of the cut region, fitting with a smooth polynomial, and extrapolating to the cut region is justified.

3.4 Ξ Reconstruction

Our motivation for studying $\Xi^- K^\pm$ systems is to attempt to better understand the striking difference in the ΛK^+ and ΛK^- data at low k^* (Figure 13).

The reconstruction of Ξ particles is one level above V0 reconstruction. V0 particles are topologically reconstructed by searching for the charged daughters' tracks into which they decay. With Ξ particles, we search for the V0 particle and charged daughter into which the Ξ decays. In the case of Ξ^- , we search for the Λ (V0) and π^- (track) daughters. We will refer to this π as the "bachelor π ".

253 The following cuts were used to select good Ξ^- ($\bar{\Xi}^+$) candidates:

254 1. V0 Daughter Reconstruction

255 (a) V0 Daughter Particle Cuts

256 i. Cuts Common to Both Daughters

257 A. $|\eta| < 0.8$

258 B. SetTPCnclsDaughters(80)

259 C. SetStatusDaughters(AliESDtrack::kTPCrefic)

260 D. SetMaxDcaV0Daughters(0.4)

261 ii. Pion Specific Daughter Cuts

262 A. $p_T > 0.16$

263 B. DCA to prim vertex > 0.3

264 iii. Proton Specific Daughter Cuts

265 A. $p_T > 0.5(p) [0.3(\bar{p})] \text{ GeV}/c$

266 B. DCA to prim vertex > 0.1

267 (b) V0 Cuts

268 i. $|\eta| < 0.8$

269 ii. $p_T > 0.4 \text{ GeV}/c$

270 iii. $|m_{inv} - m_{PDG}| < 3.8 \text{ MeV}$

271 iv. DCA to prim. vertex $> 0.2 \text{ cm}$

272 v. Cosine of pointing angle to Ξ decay vertex > 0.9993

273 vi. OnFlyStatus = false

274 vii. Decay Length $< 60 \text{ cm}$

275 viii. The misidentification cuts described in Section 3.3.1 are utilized

276 2. Bachelor π Cuts

277 (a) $|\eta| < 0.8$

278 (b) $p_T < 100 \text{ GeV}/c$

279 (c) DCA to prim vertex $> 0.1 \text{ cm}$

280 (d) SetTPCnclsDaughters(70)

281 (e) SetStatusDaughters(AliESDtrack::kTPCrefic)

282 3. Ξ Cuts

283 (a) $|\eta| < 0.8$

284 (b) $0.8 < p_T < 100 \text{ GeV}/c$

285 (c) $|m_{inv} - m_{PDG}| < 3.0 \text{ MeV}$

286 (d) DCA to prim. vertex $< 0.3 \text{ cm}$

287 (e) Cosine of pointing angle > 0.9992

288 4. Shared Daughter Cut for Ξ Collection

- 289 – Iterate through Ξ collection to ensure that no daughter is used in more than one Ξ candidate
- 290 – Remove any candidate in which the bachelor π is also a daughter of the Λ (implemented in
- 291 AliFemtoXiTrackPairCut class)

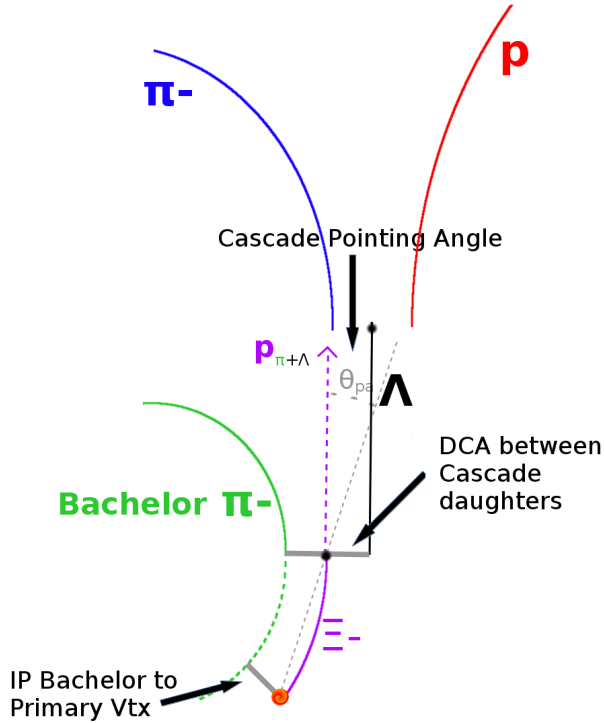


Fig. 7: Ξ Reconstruction

292 The purity of our Ξ and $\bar{\Xi}$ collections are calculated just as those of our V0 collections 3.3. Figure 8,
 293 which is used to calculate the purity, shows the m_{inv} distribution of our $\Xi(\bar{\Xi})$ candidates just before the
 294 final m_{inv} cut. Currently, we have Purity(Ξ^-) $\approx 90\%$ and Purity($\bar{\Xi}^+$) $\approx 92\%$.

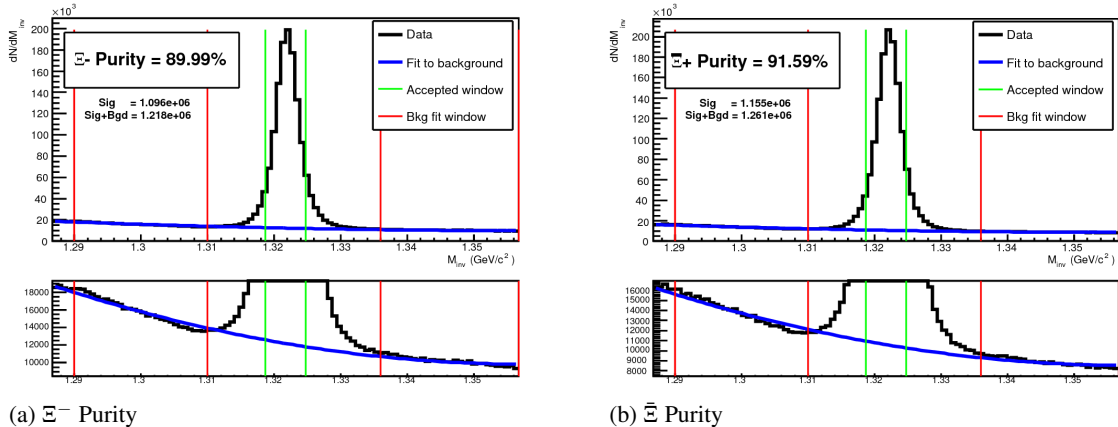


Fig. 8: Invariant mass (m_{inv}) distribution for all Ξ^- (a) and $\bar{\Xi}^+$ (b) candidates immediately before the final invariant mass cut. The bottom figures are zoomed to show the background with fit. The vertical green lines represent the m_{inv} cuts used in the analyses, the red vertical lines delineate the regions over which the background was fit, and the blue line shows the background fit. These distributions are used to calculate the collection purities, Purity(Ξ^-) $\approx 90\%$ and Purity($\bar{\Xi}^+$) $\approx 92\%$.

295 3.5 Pair Selection

296 It is important to obtain true particle pairs in the analysis. In particular, contamination from pairs con-
 297 structed with split or merged tracks, and pairs sharing daughters, can introduce an artificial signal into
 298 the correlation function, obscuring the actual physics. We impose the following pair cuts to combat these

299 issues:

300 1. Shared Daughter Cut for Pairs

301 (a) V0-V0 Pairs (i.e. ΛK_S^0 analyses)

- 302 – Remove all pairs which share a daughter

303 – Ex. Λ and K_S^0 particles which share a π^- daughter are not included

304 (b) V0-Track Pairs (i.e. ΛK^\pm analyses)

- 305 – Remove pairs if Track is also used as a daughter of the V0

306 – In these analyses, this could only occur if, for instance, a K is misidentified as a π
307 or p in the V0 reconstruction

308 (c) Ξ -Track Pairs

- 309 – Remove pairs if Track is also used as a daughter of the Ξ

310 – In these analyses, this could only occur if, for instance, a K is misidentified as a π
311 or p in the V0 reconstruction, or misidentified as bachelor π .

312 2. Average Separation Cuts (AvgSep)

- 313 – Used to cut out splitting and merging effects

314 – The motivation for these cuts can be seen in Figures 9, 10, and 11, in which average separation
315 correlation functions are presented

316 (a) ΛK_S^0 Analyses

- 317 – AvgSep > 6.0 cm for like charge sign daughters

318 – ex. p daughter of Λ and π^+ daughter of K_S^0

- 319 – No cut for unlike-sign daughters

320 (b) ΛK^\pm Analyses

- 321 – AvgSep > 8.0 cm for daughter of $\Lambda(\bar{\Lambda})$ sharing charge sign of K^\pm

322 – ex. in ΛK^+ analysis, p daughter of Λ with K^+

- 323 – No cut for unlike signs

324 (c) $\Xi^- K^\pm$ Analyses

- 325 – AvgSep > 8.0 cm for any daughter of Ξ sharing charge sign of K^\pm

326 – ex. in $\Xi^- K^-$ analysis, π^- daughter of Λ daughter with K^- , and bachelor π^- daughter with K^-

- 327 – No cut for unlike signs

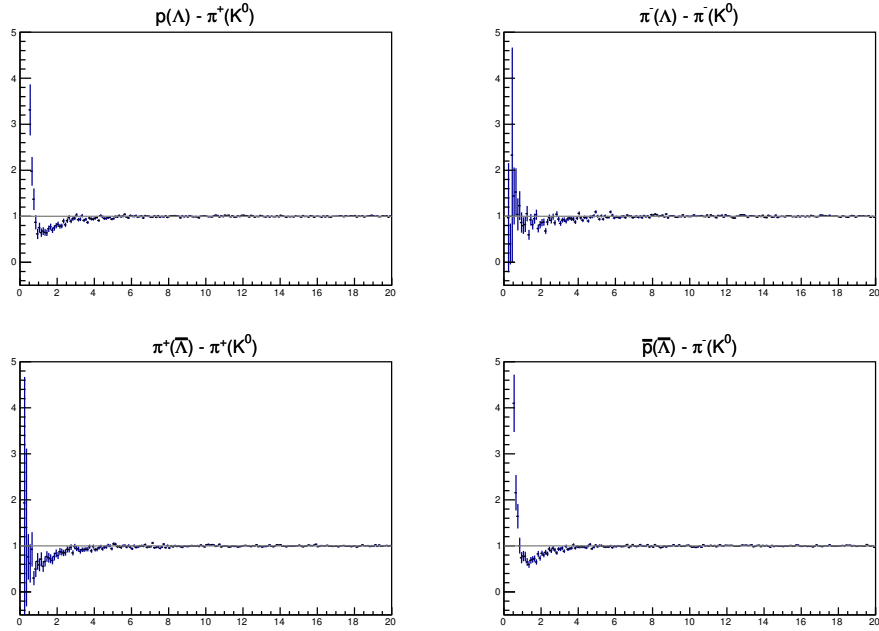


Fig. 9: Average separation (cm) correlation functions of $\Lambda(\bar{\Lambda})$ and K_S^0 Daughters. Only like-sign daughter pairs are shown (the distributions for unlike-signs were found to be flat). The title of each subfigure shows the daughter pair, as well as the mother of each daughter (in “()”), ex. top left is p from Λ with π^+ from K_S^0 .

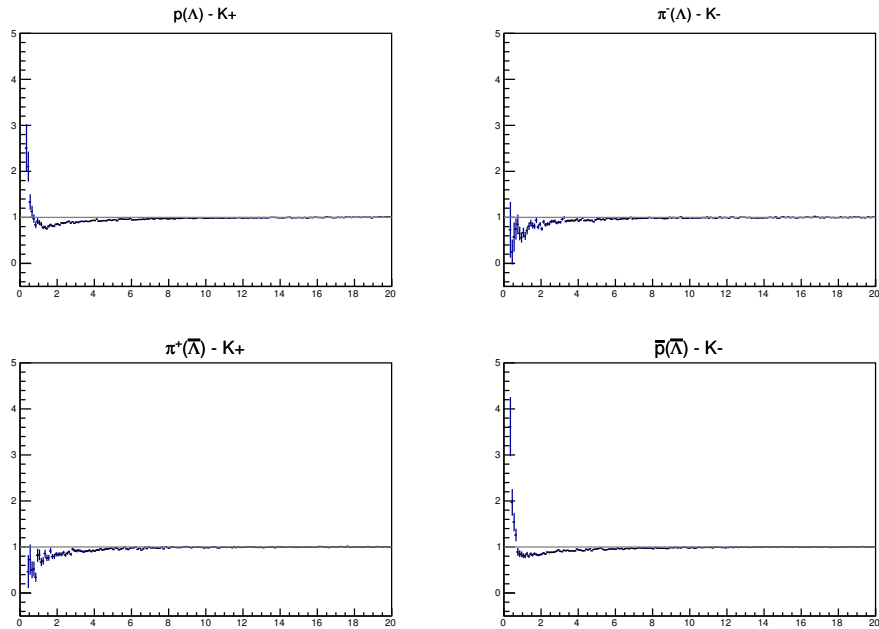


Fig. 10: Average separation (cm) correlation functions of $\Lambda(\bar{\Lambda})$ Daughter and K^\pm . Only like-sign pairs are shown (unlike-signs were flat). In the subfigure titles, the particles in “()” represent the mothers, ex. top left is p from Λ with K^+ .

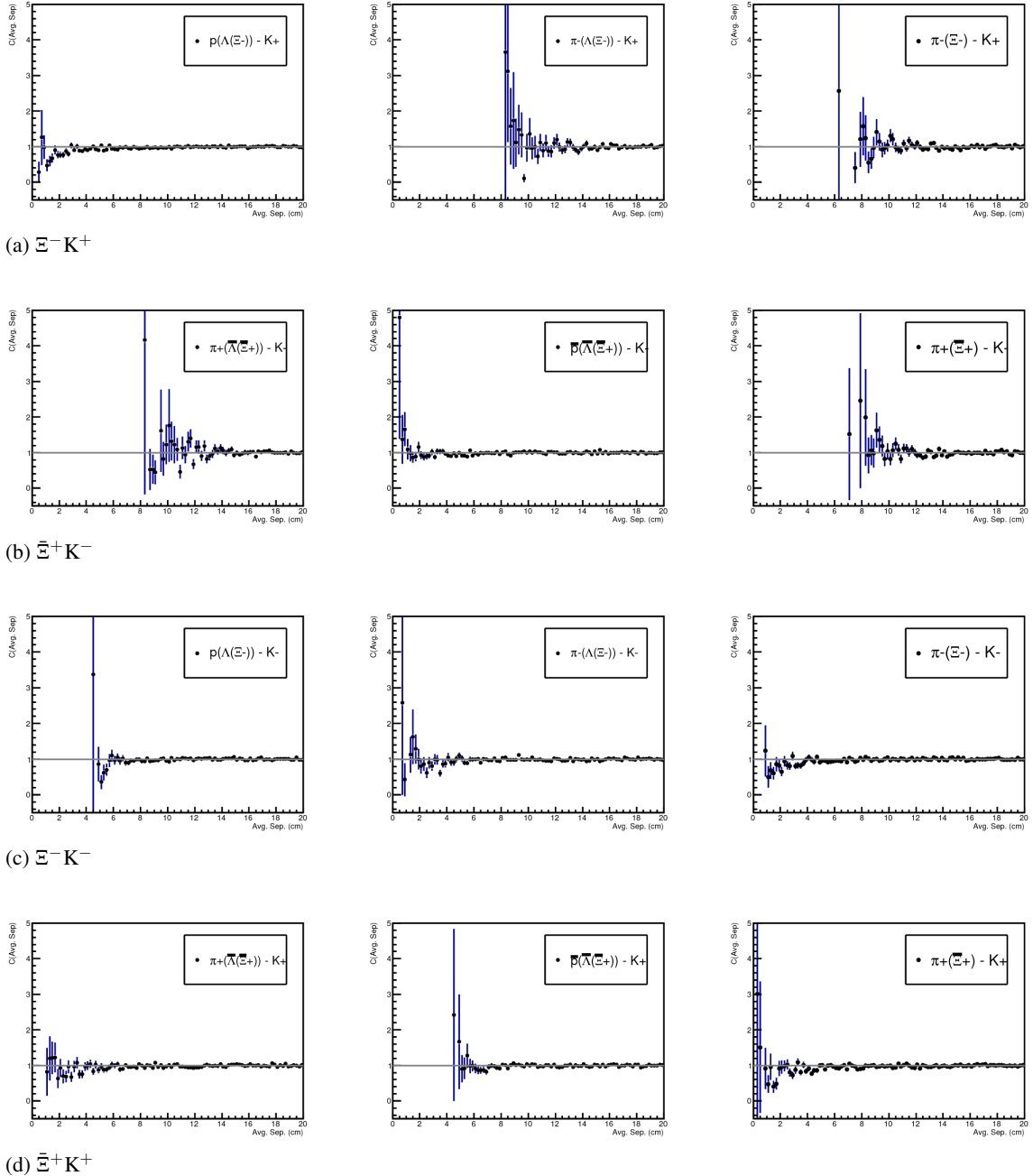


Fig. 11: Average separation (cm) correlation functions of Ξ Daughter and K^\pm . In the subfigure titles, the particles in “()” represent the mothers, ex. top left is p from Λ from Ξ^- with K^+ .

329 **4 Correlation Functions**

330 This analysis studies the momentum correlations of both ΛK and $\Xi^- K^\pm$ pairs using the two-particle
 331 correlation function, defined as $C(k^*) = A(k^*)/B(k^*)$, where $A(k^*)$ is the signal distribution, $B(k^*)$ is the
 332 reference (or background) distribution, and k^* is the momentum of one of the particles in the pair rest
 333 frame. In practice, $A(k^*)$ is constructed by binning in k^* pairs from the same event. Ideally, $B(k^*)$ is
 334 similar to $A(k^*)$ in all respects excluding the presence of femtoscopic correlations [2]; as such, $B(k^*)$
 335 is used to divide out the phase-space effects, leaving only the femtoscopic effects in the correlation
 336 function.

337 This analysis presents correlation functions for three centrality bins (0-10%, 10-30%, and 30-50%), and
 338 is currently pair transverse momentum ($k_T = 0.5|\mathbf{p}_{T,1} + \mathbf{p}_{T,2}|$) integrated (i.e. not binned in k_T). The
 339 correlation functions are constructed separately for the two magnetic field configurations, and, after
 340 assuring consistency, are combined using a weighted average:

$$C_{combined}(k^*) = \frac{\sum_i w_i C_i(k^*)}{\sum_i w_i} \quad (3)$$

341 where the sum runs over the correlation functions to be combined, and the weight, w_i , is the number of
 342 numerator pairs in $C_i(k^*)$. Here, the sum is over the two field configurations (++ and - -).

343 **4.1 Typical Correlation Function Construction**

344 In practice, $B(k^*)$ is typically obtained by forming mixed-event pairs, i.e. particles from a given event
 345 are paired with particles from N_{mix} (= 5) other events, and these pairs are then binned in k^* . In forming
 346 the background distribution, it is important to mix only similar events; mixing events with different
 347 phase-spaces can result in an unreliable background distribution, and can introduce artificial signals in
 348 the correlation function. Therefore, in this analysis, we bin our events both in primary vertex location (2
 349 cm bin width) and in centrality (5% bin width), and we only mix events within a given bin; i.e. we only
 350 mix events of like centrality and of like primary vertex location. Also note, a vertex correction is also
 351 applied to each event, which essentially recenters the the primary vertices to $z = 0$.

352 Figures 12a, 12b, 12c show the correlation functions for all centralities studied for $\Lambda K^+(\bar{\Lambda} K^-)$, $\Lambda K^-(\bar{\Lambda} K^+)$,
 353 and $\Lambda(\bar{\Lambda})K_S^0$, respectively. All were normalized in the range $0.32 < k^* < 0.4$ GeV/c. It is interesting to
 354 note that the average of the $\Lambda K^+(\bar{\Lambda} K^-)$ and $\Lambda K^-(\bar{\Lambda} K^+)$ correlation functions is consistent with our
 355 $\Lambda K_S^0(\bar{\Lambda} K_S^0)$ measurement.

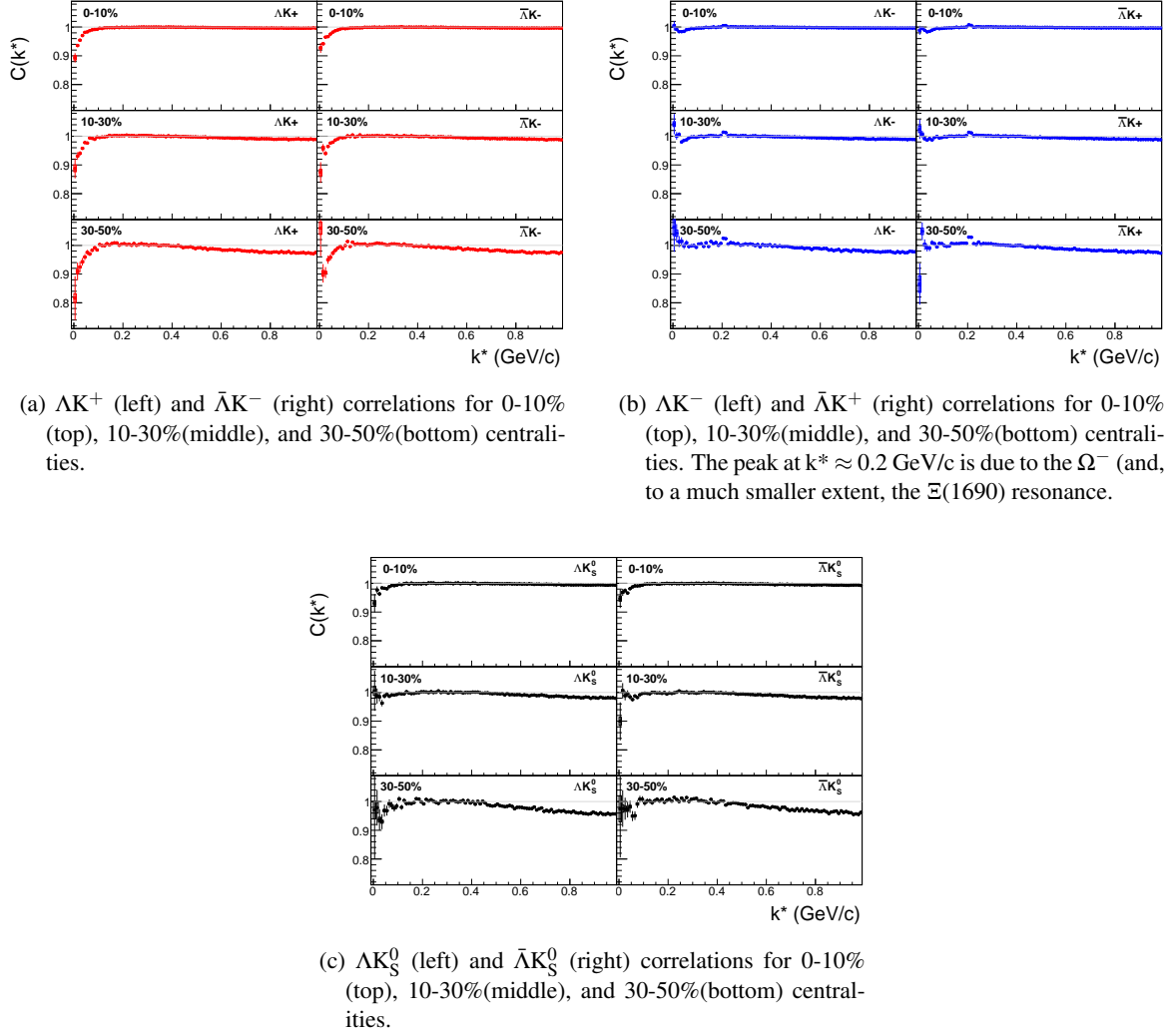


Fig. 12: ΛK and $\bar{\Lambda}K$ correlation functions for 0-10%, 10-30%, and 30-50% centralities. The lines represent the statistical errors, while the boxes represent the systematic errors.

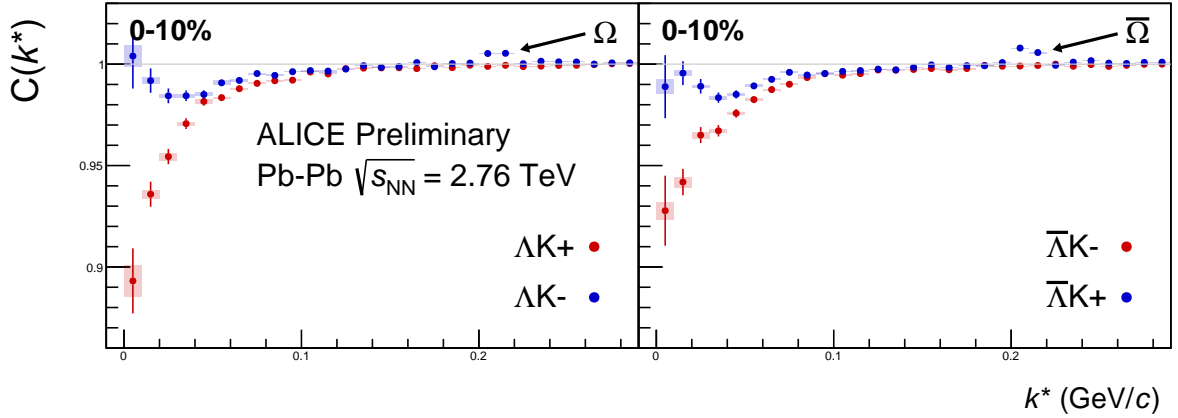


Fig. 13: Correlation Functions: ΛK^+ vs ΛK^- ($\bar{\Lambda}K^+$ vs $\bar{\Lambda}K^-$) for 0-10% centrality. The peak in ΛK^- ($\bar{\Lambda}K^+$) at $k^* \approx 0.2 \text{ GeV}/c$ is due to the Ω^- (and, to a much smaller extent, the $\Xi(1690)$ resonance. The lines represent the statistical errors, while boxes represent systematic errors.

356 4.2 Stavinsky Correlation Function Construction

357 The purpose of the Stavinsky method is to rid the correlation functions of the non-femtoscopic back-
358 ground. More specifically, this method is intended to handle background contributions from elliptic
359 flow, and other sources having reflection symmetry in the transverse plane. With the Stavinsky method,
360 mixed-event pairs are not used for the background ($B(k^*)$); instead, same-event pseudo-pairs, formed
361 by rotating one particle in a real pair by 180° in the transverse plane, are used as a background. This
362 rotation rids the pairs of any femtoscopic correlation, while maintaining correlations due to elliptic flow
363 (and other suitably symmetric contributors).

364 The results of correctly implementing such a procedure are shown in Figure 14. The figure shows the
365 Stavinsky method does a very good job of ridding the ΛK^\pm correlations of their non-femtoscopic back-
366 grounds. We also see the procedure does not work as well on the ΛK_S^0 system.

367 Now, one must be somewhat careful when applying this Stavinsky method. We found that, in order to
368 obtain correct results, we had to run our pseudo-pairs through the same pair cuts used in our analyses.
369 In an ideal world, our pair cut would only remove truly bad pairs results from splitting, merging, etc. In
370 the real world, the pair cut always throws out some of the good with the bad. For the pseudo-pairs to
371 form a reliable background, they too must experience the pair cut, and the loss of “good” pseudo-pairs.
372 We found this issue affected mainly our ΛK^+ & $\bar{\Lambda} K^-$ analysis, as can be seen in Figure 15, which shows
373 both a correct implementation of the Stavinsky method, and an incorrect implementation lacking the
374 additional pair cut on the pseudo-pairs.

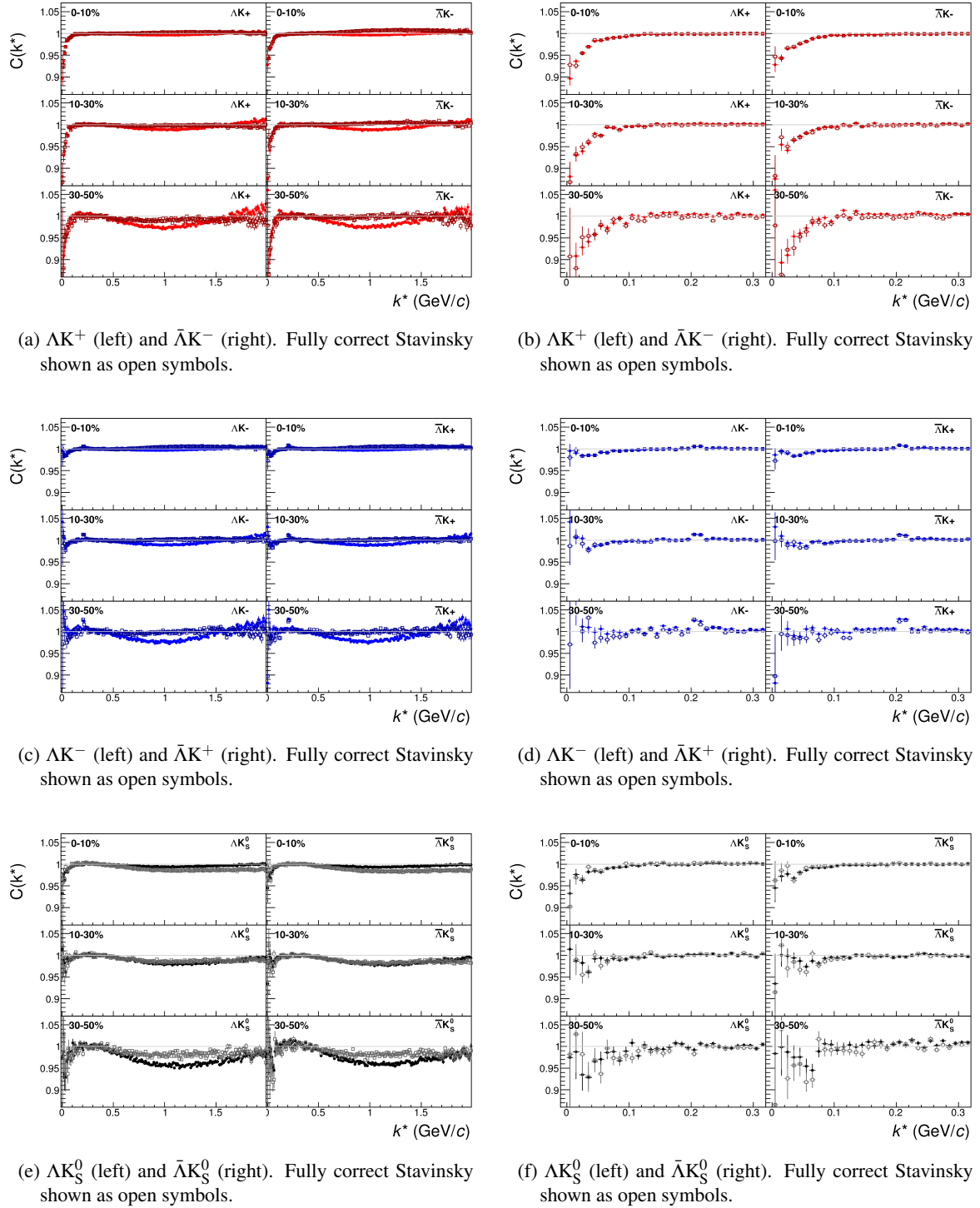
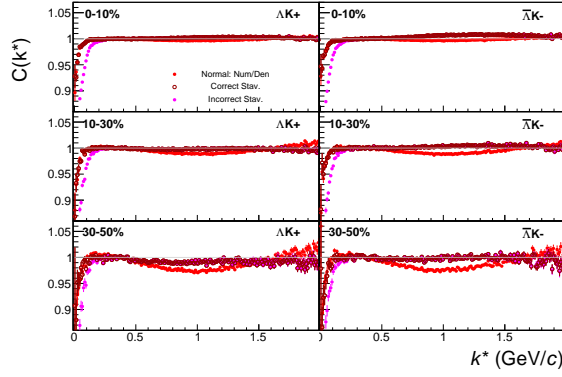
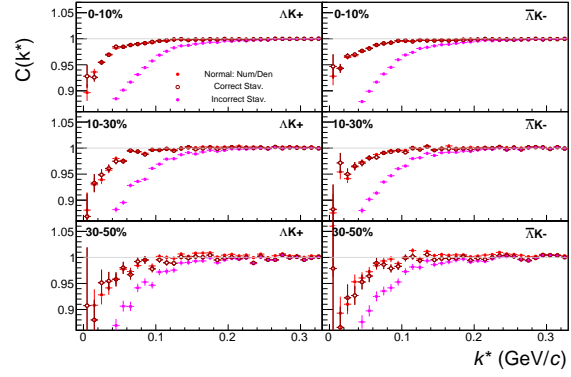


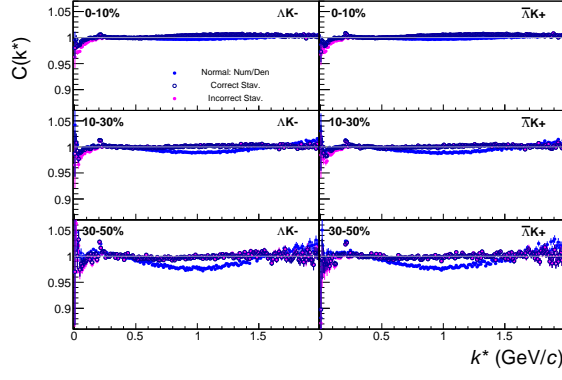
Fig. 14: ΛK and $\bar{\Lambda} \bar{K}$ correlation functions built using the fully correct Stavinsky method for 0-10%, 10-30%, and 30-50% centralities. In the fully correct method, the pseudo-pairs (same-event pairs with one particle rotated by 180° in the transverse plane) are also run through the pair cuts used in the analysis (an example of an incorrect implementation is shown in Fig. 15). Closed symbols represent correlations built using the normal mixed-event background, while open symbols represent correlations formed using the Stavinsky same-event pseudo-pairs as a background. Figures in the right column are zoomed-in versions of figures in the left column.



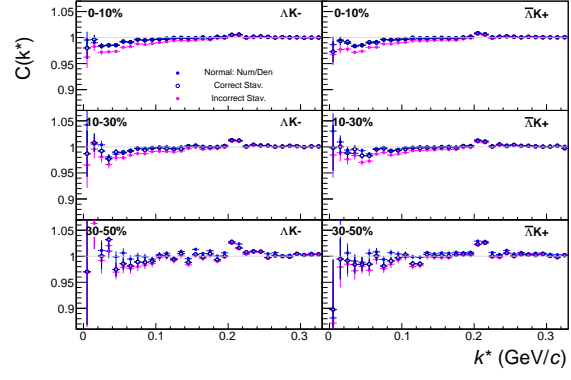
(a) ΔK^+ (left) and $\bar{\Delta}K^-$ (right). Incorrect Stavinsky shown as open symbols.



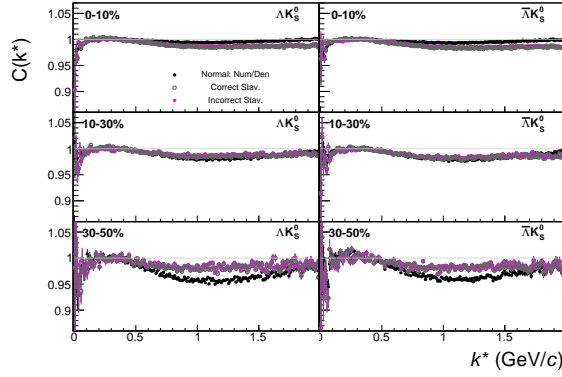
(b) ΔK^+ (left) and $\bar{\Delta}K^-$ (right). Incorrect Stavinsky shown as open symbols.



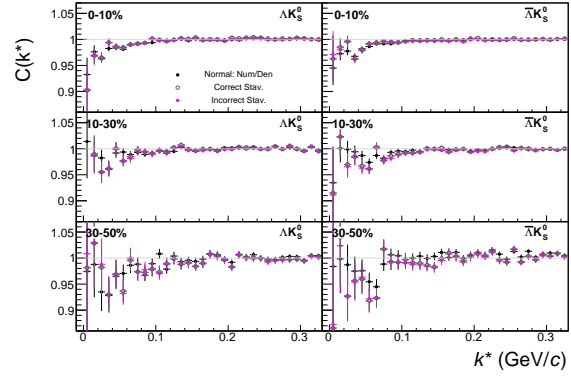
(c) ΔK^- (left) and $\bar{\Delta}K^+$ (right). Incorrect Stavinsky shown as open symbols.



(d) ΔK^- (left) and $\bar{\Delta}K^+$ (right). Incorrect Stavinsky shown as open symbols.



(e) ΔK_S^0 (left) and $\bar{\Delta}K_S^0$ (right). Incorrect Stavinsky shown as open symbols.



(f) ΔK_S^0 (left) and $\bar{\Delta}K_S^0$ (right). Incorrect Stavinsky shown as open symbols.

Fig. 15: ΔK and $\bar{\Delta}K$ correlation functions built, both correctly and incorrectly, using the Stavinsky method for 0-10%, 10-30%, and 30-50% centralities. This figure is the same as Fig. 14, but with results from the incorrect Stavinsky implementation shown in magenta. The closed, (red, blue, black) symbols represent correlation functions formed using the normal method with mixed-event background pairs. The open, cyan symbols represent correlation functions formed using the correct Stavinsky method. The closed, magenta symbols represent correlation functions formed using the incorrect Stavinsky method. In the correct method, the pseudo-pairs (same-event pairs with one particle rotated by 180° in the transverse plane) are also run through the pair cuts used in the analysis; in the incorrect method, they are not. Figures in the right column are zoomed-in versions of figures in the left column.

375 **5 Fitting**

376 **5.1 Model: $\Lambda K_S^0, \Lambda K^\pm, \Xi^- K_S^0$**

377 The two-particle relative momentum correlation function may be written theoretically by the Koonin-
378 Pratt equation [3, 4]:

$$C(\mathbf{k}^*) = \int S(\mathbf{r}^*) |\Psi_{\mathbf{k}^*}(\mathbf{r}^*)|^2 d^3 \mathbf{r}^* \quad (4)$$

379 where $S(\mathbf{r}^*)$ is the pair source distribution, $\Psi_{\mathbf{k}^*}(\mathbf{r}^*)$ is the two-particle wave-function, and k^* is the
380 momentum of one particle in the pair rest frame. In the absence of Coulomb effects, and assuming a
381 spherically Gaussian source of width R , and s-wave scattering, the 1D femtoscopic correlation function
382 can be calculated analytically using:

$$C(k^*) = 1 + C_{QI}(k^*) + C_{FSI}(k^*) \quad (5)$$

383 C_{QI} describes plane-wave quantum interference:

$$C_{QI}(k^*) = \alpha \exp(-4k^{*2}R^2) \quad (6)$$

384 where $\alpha = (-1)^{2j}/(2j+1)$ for identical particles with spin j , and $\alpha = 0$ for non-identical particles. For
385 all analyses presented in this note, $\alpha = 0$. C_{FSI} describes the s-wave strong final state interaction between
386 the particles:

$$\begin{aligned} C_{FSI}(k^*) &= (1 + \alpha) \left[\frac{1}{2} \left| \frac{f(k^*)}{R} \right|^2 \left(1 - \frac{d_0}{2\sqrt{\pi}R} \right) + \frac{2\Re f(k^*)}{\sqrt{\pi}R} F_1(2k^*R) - \frac{\Im f(k^*)}{R} F_2(2k^*R) \right] \\ f(k^*) &= \left(\frac{1}{f_0} + \frac{1}{2} d_0 k^{*2} - ik^* \right)^{-1}; \quad F_1(z) = \int_0^z \frac{e^{x^2-z^2}}{z} dx; \quad F_2(z) = \frac{1-e^{-z^2}}{z} \end{aligned} \quad (7)$$

387 where R is the source size, $f(k^*)$ is the s-wave scattering amplitude, f_0 is the complex scattering length,
388 and d_0 is the effective range of the interaction.

389 An additional parameter λ is typically included in the femtoscopic fit function to account for the purity
390 of the pair sample. In the case of no residual correlations (to be discussed in Section 5.4), the fit function
391 becomes:

$$C(k^*) = 1 + \lambda [C_{QI}(k^*) + C_{FSI}(k^*)] \quad (8)$$

392 **5.2 Model: $\Xi^- K^\pm$**

393 The two-particle correlation function may be written as:

$$C(\mathbf{k}^*) = \sum_S \rho_S \int S(\mathbf{r}^*) |\Psi_{\mathbf{k}^*}^S(\mathbf{r}^*)|^2 d^3 \mathbf{r}^* \quad (9)$$

394 where ρ_S is the normalized emission probability of particles in a state with spin S , $S(\mathbf{r}^*)$ is the pair
395 emission source distribution (assumed to be Gaussian), and $\Psi_{\mathbf{k}^*}^S(\mathbf{r}^*)$ is the two-particle wave-function
396 including both strong and Coulomb interactions [5]:

$$\Psi_{\mathbf{k}^*}(\mathbf{r}^*) = e^{i\delta_c} \sqrt{A_c(\eta)} [e^{i\mathbf{k}^*\cdot\mathbf{r}^*} F(-i\eta, 1, i\xi) + f_c(k^*) \frac{\tilde{G}(\rho, \eta)}{r^*}] \quad (10)$$

where $\rho = k^*r^*$, $\eta = (k^*a_c)^{-1}$, $\xi = \mathbf{k}^* \cdot \mathbf{r}^* + k^*r^* \equiv \rho(1 + \cos\theta^*)$, and $a_c = (\mu z_1 z_2 e^2)^{-1}$ is the two-particle Bohr radius (including the sign of the interaction). δ_c is the Coulomb s-wave phase shift, $A_c(\eta)$ is the Coulomb penetration factor, $\tilde{G} = \sqrt{A_c}(G_0 + iF_0)$ is a combination of the regular (F_0) and singular (G_0) s-wave Coulomb functions. $f_c(k^*)$ is the s-wave scattering amplitude:

$$f_c(k^*) = \left[\frac{1}{f_0} + \frac{1}{2} d_0 k^{*2} - \frac{2}{a_c} h(\eta) - ik^* A_c(\eta) \right]^{-1} \quad (11)$$

where, the “h-function”, $h(\eta)$, is expressed through the digamma function, $\psi(z) = \Gamma'(z)/\Gamma(z)$ as:

$$h(\eta) = 0.5[\psi(i\eta) + \psi(-i\eta) - \ln(\eta^2)] \quad (12)$$

In this case, the λ parameter may be included as:

$$C(\mathbf{k}^*) = (1 - \lambda) + \lambda \sum_S \rho_S \int S(\mathbf{r}^*) |\Psi_{\mathbf{k}^*}^S(\mathbf{r}^*)|^2 d^3\mathbf{r}^* \quad (13)$$

5.3 Momentum Resolution Corrections

Finite track momentum resolution causes the reconstructed momentum of a particle to smear around the true value. This, of course, also holds true for V0 particles. The effect is propagated up to the pairs of interest, which causes the reconstructed relative momentum (k_{Rec}^*) to differ from the true momentum (k_{True}^*). Smearing of the momentum typically will result in a suppression of the signal. More specifically, the smearing will broaden the signal, which would cause a decrease in the extracted radius of the system.

The effect of finite momentum resolution can be investigated using the HIJING MC data, for which both the true and reconstructed momenta are available. Figure 16 shows sample k_{True}^* vs. k_{Rec}^* plots for ΛK^\pm 0-10% analyses; Figure 16a was generated using same-event pairs, while Figure 16b was generated using mixed-event pairs (with $N_{\text{mix}} = 5$).

If there are no contaminations in our particle collection, the plots in Figure 16 should be smeared around $k_{\text{True}}^* = k_{\text{Rec}}^*$; this is mostly true in our analyses. However, there are some interesting features of our results which demonstrate a small (notice the log-scale on the z-axis) contamination in our particle collection. The structure around $k_{\text{Rec}}^* = k_{\text{True}}^* - 0.15 \text{ GeV}/c$ is mainly caused by K_S^0 contamination in our $\Lambda(\bar{\Lambda})$ sample. The remaining structure not distributed about $k_{\text{Rec}}^* = k_{\text{True}}^*$ is due to π and e contamination in our K^\pm sample. These contaminations are more visible in Figure 17, which show k_{Rec}^* vs. k_{True}^* plots (for a small sample of the ΛK^\pm 0-10% central analysis), for which the MC truth (i.e. true, known identity of the particle) was used to eliminate misidentified particles in the $K^+(a)$ and $\Lambda(b)$ collections. (NOTE: This is an old figure and is for a small sample of the data. A new version will be generated shortly. It, nonetheless, demonstrates the point well).

Information gained from looking at k_{Rec}^* vs k_{true} can be used to apply corrections to account for the effects of finite momentum resolution on the correlation functions. A typical method (“Ratio” method) involves using the MC HIJING data to build two correlation functions, $C_{\text{Rec}}(k^*)$ and $C_{\text{True}}(k^*)$, using the generator-level momentum (k_{True}^*) and the measured detector-level momentum (k_{Rec}^*). The data is then corrected by multiplying by the ratio, $C_{\text{True}}/C_{\text{Rec}}$, before fitting. This essentially unsmears the data, which then can be compared directly to theoretical predictions and fits. Although this is conceptually simple, there are a couple of big disadvantages to this method. First, HIJING does not incorporate final-state interactions, so weights must be used when building same-event (numerator) distributions. These weights account for the interactions, and, in the absence of Coulomb interactions, can be calculated using Eq. 5. Of course, these weights are valid only for a particular set of fit parameters. Therefore, in the fitting process, during which the fitter explores a large parameter set, the corrections will not remain valid. As

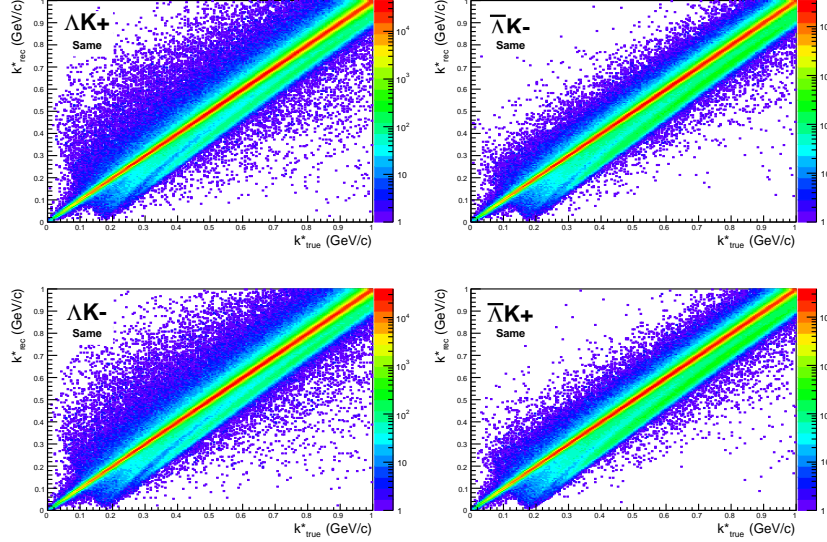
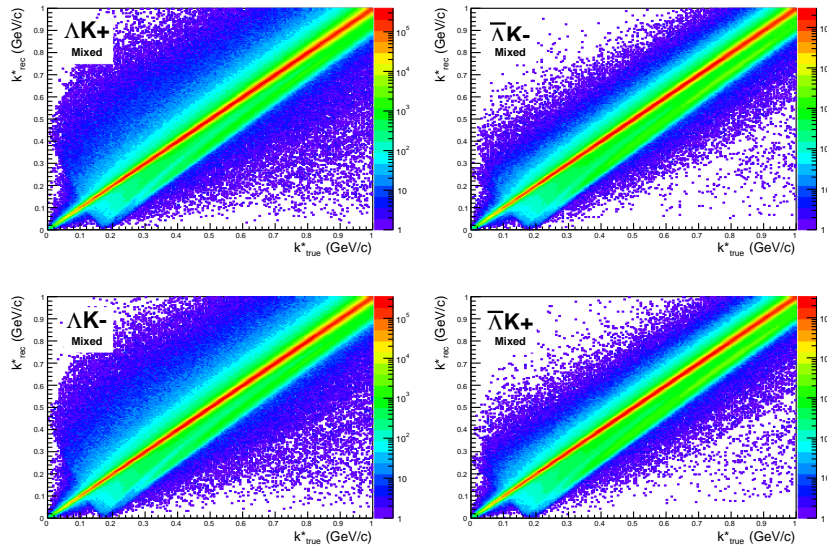
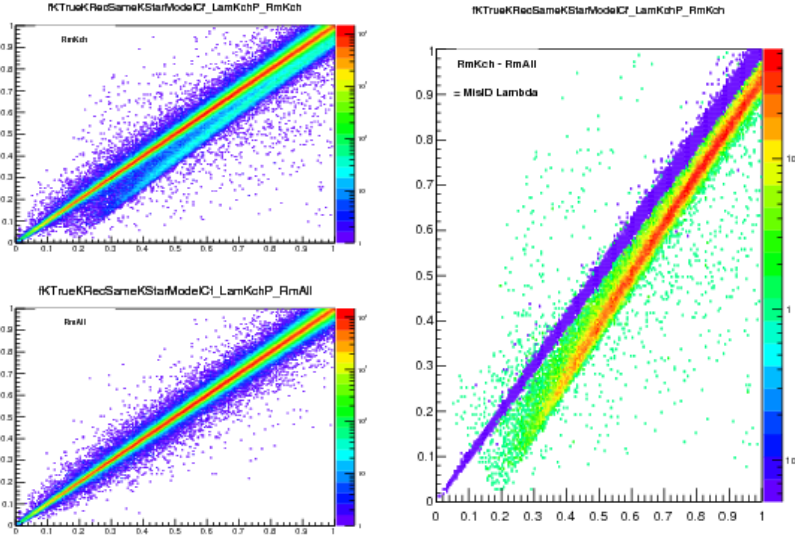
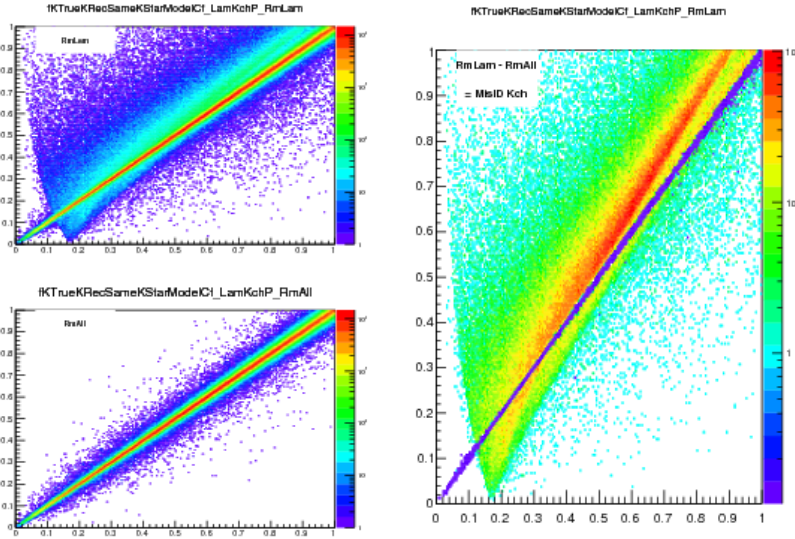
(a) Same Event Pairs (ΛK^\pm , 0-10% Centrality)(b) Mixed Event Pairs (ΛK^\pm , 0-10% Centrality)

Fig. 16: Sample k_{True}^* vs. k_{Rec}^* plots from MC HIJING events for ΛK^\pm 0-10% analyses. The structure which appears around $k_{\text{Rec}}^* = k_{\text{True}}^* - 0.15 \text{ GeV}/c$ is mainly caused by K_S^0 contamination in our $\Lambda(\bar{\Lambda})$ sample. The remaining structure not distributed about $k_{\text{Rec}}^* = k_{\text{True}}^*$ is due to π and e contamination in our K^\pm sample. These contaminations are more clearly visible in Figure 17

such, applying the momentum resolution correction and fitting becomes a long and drawn out iterative process. An initial parameter set is obtained (through fitting without momentum resolution corrections, theoretical models, or a good guess), then the MC data is analyzed to obtain correlation functions needed to calculate the correction factor, the data is fit using the correction factor, a refined parameter set is extracted, the MC data is analyzed again to obtain the new correction factor, etc. This process continues until the parameter set stabilizes. The second issue concerns statistics. With the MC data available on the grid, we were not able to generate the statistics necessary to use the raw $C_{\text{True}}/C_{\text{Rec}}$ ratio. The ratio was not stable, and when applied to the data, obscured the signal. Attempting to fit the ratio to use to generate the corrections also proved problematic. However, as HIJING does not include final-state interactions, the same-event and mixed-event pairs are very similar (with the exception of things like



(a) (Top Left) All misidentified K^+ excluded. (Bottom Left) All misidentified Λ and K^+ excluded. (Right) The difference of (Top Left) - (Bottom Left), which reveals the contamination in our Λ collection. The structure which appears around $k_{\text{Rec}}^* = k_{\text{True}}^* - 0.15 \text{ GeV}/c$ is mainly caused by K_S^0 contamination in our $\Lambda(\bar{\Lambda})$ sample.



(b) (Top Left) All misidentified Λ excluded. (Bottom Left) All misidentified Λ and K^+ excluded. (Right) The difference of (Top Left) - (Bottom Left), which reveals the contamination in our K^+ collection. The structure not distributed about $k_{\text{Rec}}^* = k_{\text{True}}^*$ is due to π and e^- contamination in our K^\pm sample.

Fig. 17: In the figure, the y-axis = k_{Rec}^* , and the x-axis = k_{True}^* . (Left) k_{Rec}^* vs. k_{True}^* plots for a small sample of the ΛK^+ 0-10% central analysis, MC truth was used to eliminate misidentified particles in the K^+ (a) and Λ (b) collections. (Right) The difference of the top left and bottom left plots. Contaminations in our particle collections are clearly visible. Figure (a) demonstrates a K_S^0 contamination in our Λ collection; Figure (b) demonstrates a π and e^- contamination in our K^\pm collection.

444 energy and momentum conservation, etc). Therefore, one may build the numerator distribution using
 445 mixed-event pairs. This corresponds, more or less, to simply running the weight generator through the
 446 detector framework.

447 A second approach (“Matrix” method) is to use information gained from plots like those in Figure 16,

448 which can be considered response matrices. The response matrix describes quantitatively how each
 449 k_{Rec}^* bin receives contributions from multiple k_{True}^* bins, and can be used to account for the effects of
 450 finite momentum resolution. With this approach, the resolution correction is applied on-the-fly during
 451 the fitting process by propagating the theoretical correlation function (fit) through the response matrix,
 452 according to:

$$C_{\text{Fit}}(k_{\text{Rec}}^*) = \frac{\sum_{k_{\text{True}}^*} M_{k_{\text{Rec}}^*, k_{\text{True}}^*} C_{\text{Fit}}(k_{\text{True}}^*)}{\sum_{k_{\text{True}}^*} M_{k_{\text{Rec}}^*, k_{\text{True}}^*}} \quad (14)$$

453 where $M_{k_{\text{Rec}}^*, k_{\text{True}}^*}$ is the response matrix (Figure 16), $C_{\text{Fit}}(k_{\text{True}}^*)$ is the fit binned in k_{True}^* , and the denominator normalizes the result.

455 Equation 14 describes that, for a given k_{Rec}^* bin, the observed value of $C(k_{\text{Rec}}^*)$ is a weighted average of
 456 all $C(k_{\text{True}}^*)$ values, where the weights are the normalized number of counts in the $[k_{\text{Rec}}^*, k_{\text{True}}^*]$ bin. As
 457 seen in Figure 16, overwhelmingly the main contributions comes from the $k_{\text{Rec}}^* = k_{\text{True}}^*$ bins. Although
 458 the correction is small, it is non-negligible for the low- k^* region of the correlation function.

459 Here, the momentum resolution correction is applied to the fit, not the data. In other words, during
 460 fitting, the theoretical correlation function is smeared just as real data would be, instead of unsmearing
 461 the data. This may not be ideal for the theorist attempting to compare a model to experimental data, but
 462 it leaves the experimental data unadulterated. The current analyses use this second approach to applying
 463 momentum resolution corrections because of two major advantages. First, the MC data must be analyzed
 464 only once, and no assumptions about the fit are needed. Secondly, the momentum resolution correction
 465 is applied on-the-fly by the fitter, delegating the iterative process to a computer instead of the user.

466 The two methods described above, Ratio and Matrix, should reproduce the same results at the parameter
 467 set used to generate the $C_{\text{True}}/C_{\text{Rec}}$ needed for the Ratio method. Figure 18 shows that the two methods
 468 converge as the binning size is decreased.

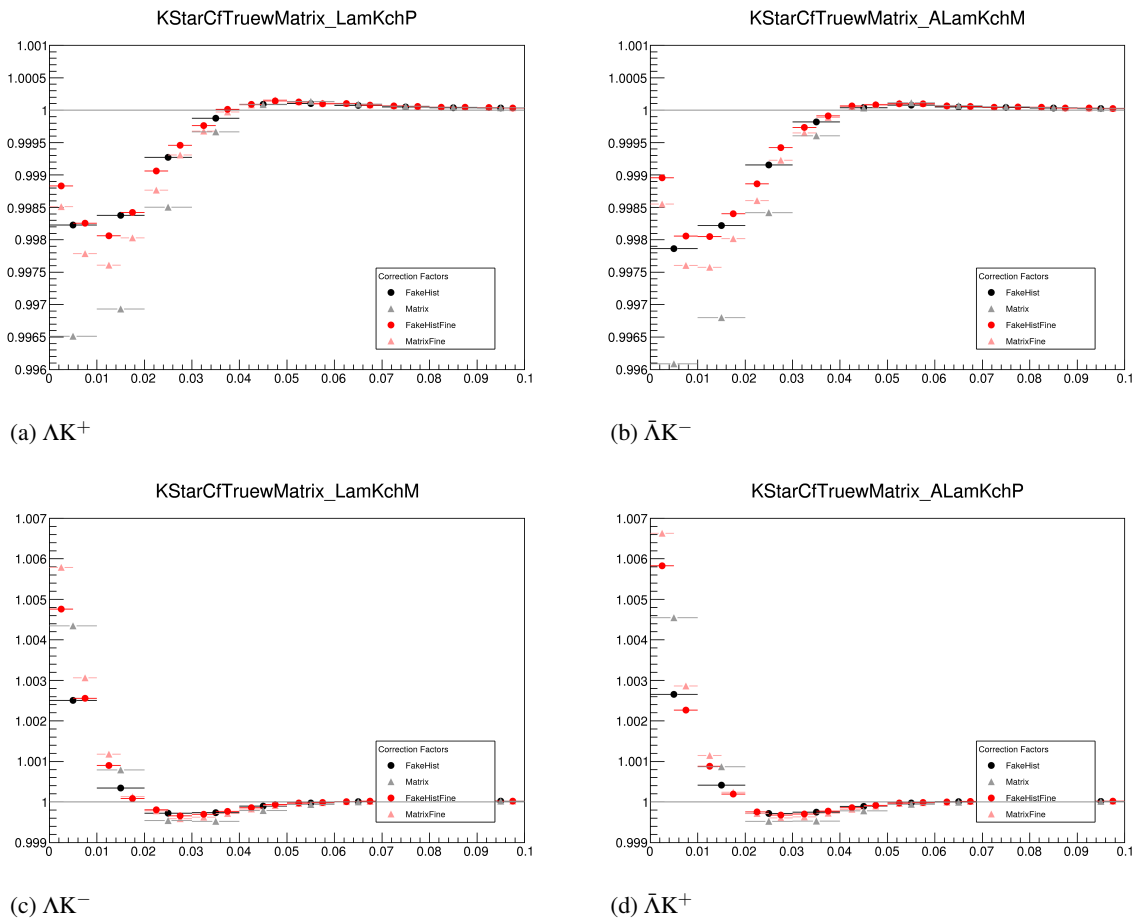


Fig. 18: Comparison of the two methods, Ratio and Matrix, for accounting for momentum resolution effects with HIJING. The Ratio method corresponds to the “FakeHist” histograms (circles), while the Matrix method corresponds to the “Matrix” histograms (triangles). Black shows a course binning, while red shows a finer binning.

469 **5.4 Residual Correlations**

470 The purpose of this analysis is to study both the interaction, and the scale of the emitting source, of
 471 the pairs. In order to obtain correct results, it is important for our particle collections to consist of
 472 primary particles. In practice, this is difficult to achieve for our Λ and $\bar{\Lambda}$ collections. Many of our Λ
 473 particles are not primary, but originate as decay products from other hyperons, including Σ^0 , Ξ^0 , Ξ^- and
 474 $\Sigma^{*(+,-,0)}(1385)$. Additionally, many of our K particles are not primary, but decay from $K^{*(+,-,0)}(892)$
 475 parents. In these decays, the daughter Λ or K_S^0 carries away a momentum very similar to that of its parent.
 476 As a result, the correlation function between a secondary Λ and, for instance, a K^+ will be sensitive to,
 477 and dependent upon, the interaction between the parent of the Λ and the K^+ . In effect, the correlation
 478 between the parent of the Λ and the K^+ (ex. $\Sigma^0 K^+$) will be visible, although smeared out, in the ΛK^+
 479 data; we call this a residual correlation resulting from feed-down. The contributions from the primary
 480 correlation, residual correlations, and fake pairs on the finally measure data is shown schematically in
 481 Figure 19. Residual correlations are important in an analysis when three criteria are met [6]: i) the parent
 482 correlation signal is large, ii) a large fraction of pairs in the sample originate from the particular parent
 483 system, and iii) the decay momenta are comparable to the expected correlation width in k^* .

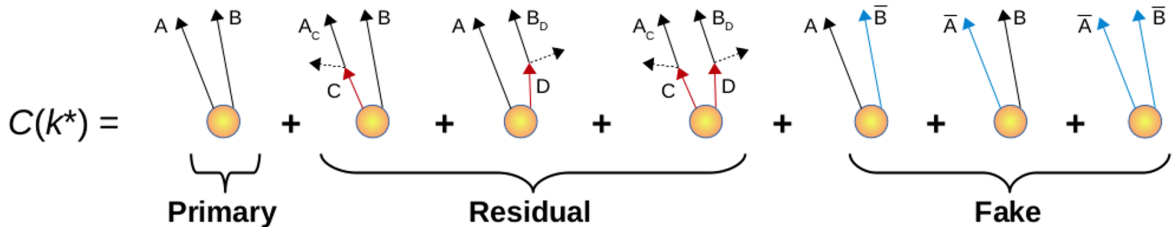


Fig. 19: A schematic representation of the contributions to the finally measured data from the primary correlation, residual correlations, and fake pairs.

484 As it is difficult for us to eliminate these residual correlations in our analyses, we must attempt to account
 485 for them in our fit. To achieve this, we will simultaneously fit the data for both the primary correlation
 486 function and the residual correlations. For example, in the simple case of a ΛK^+ analysis with residuals
 487 arising solely from $\Sigma^0 K^+$ feed-down:

$$C_{measured}(k_{\Lambda K^+}^*) = 1 + \lambda_{\Lambda K^+}[C_{\Lambda K^+}(k_{\Lambda K^+}^*) - 1] + \lambda_{\Sigma^0 K^+}[C_{\Sigma^0 K^+}(k_{\Lambda K^+}^*) - 1]$$

$$C_{\Sigma^0 K^+}(k_{\Lambda K^+}^*) \equiv \frac{\sum_{k_{\Sigma^0 K^+}^*} C_{\Sigma^0 K^+}(k_{\Sigma^0 K^+}^*) T(k_{\Sigma^0 K^+}^*, k_{\Lambda K^+}^*)}{\sum_{k_{\Sigma^0 K^+}^*} T(k_{\Sigma^0 K^+}^*, k_{\Lambda K^+}^*)} \quad (15)$$

488 $C_{\Sigma^0 K^+}(k_{\Sigma^0 K^+}^*)$ is the $\Sigma^0 K^+$ correlation function from, for instance, Equation 5, and T is the transform
 489 matrix generated with THERMINATOR. The transform matrix is formed for a given parent pair, AB,
 490 by taking all ΛK pairs originating from AB, calculating the relative momentum of the parents (k_{AB}^*)
 491 and daughters ($k_{\Lambda K}^*$), and filling a two-dimensional histogram with the values. The transform matrix
 492 is essentially an unnormalized probability distribution mapping the k^* of the parent pair to that of the
 493 daughter pair when one or both parents decay. An example of such transform matrices can be found in
 494 Figures 20 and 21.

495 The above equation can be easily extended to include feed-down from more sources:

$$\begin{aligned}
C_{measured}(k_{\Lambda K}^*) &= 1 + \lambda_{\Lambda K}[C_{\Lambda K}(k_{\Lambda K}^*) - 1] + \lambda_{\Sigma^0 K}[C_{\Sigma^0 K}(k_{\Lambda K}^*) - 1] + \dots \\
&\quad + \lambda_{P_1 P_2}[C_{P_1 P_2}(k_{\Lambda K}^*) - 1] + \lambda_{other}[C_{other}(k_{\Lambda K}^*) - 1]
\end{aligned}
\tag{16}$$

$$C_{P_1 P_2}(k_{\Lambda K}^*) \equiv \frac{\sum_{k_{P_1 P_2}^*} C_{P_1 P_2}(k_{P_1 P_2}^*) T(k_{P_1 P_2}^*, k_{\Lambda K}^*)}{\sum_{k_{P_1 P_2}^*} T(k_{P_1 P_2}^*, k_{\Lambda K}^*)}$$

496 Or, more compactly:

$$C_{measured}(k_{\Lambda K}^*) = 1 + \sum_i \lambda_i [C_i(k_{\Lambda K}^*) - 1] \tag{17}$$

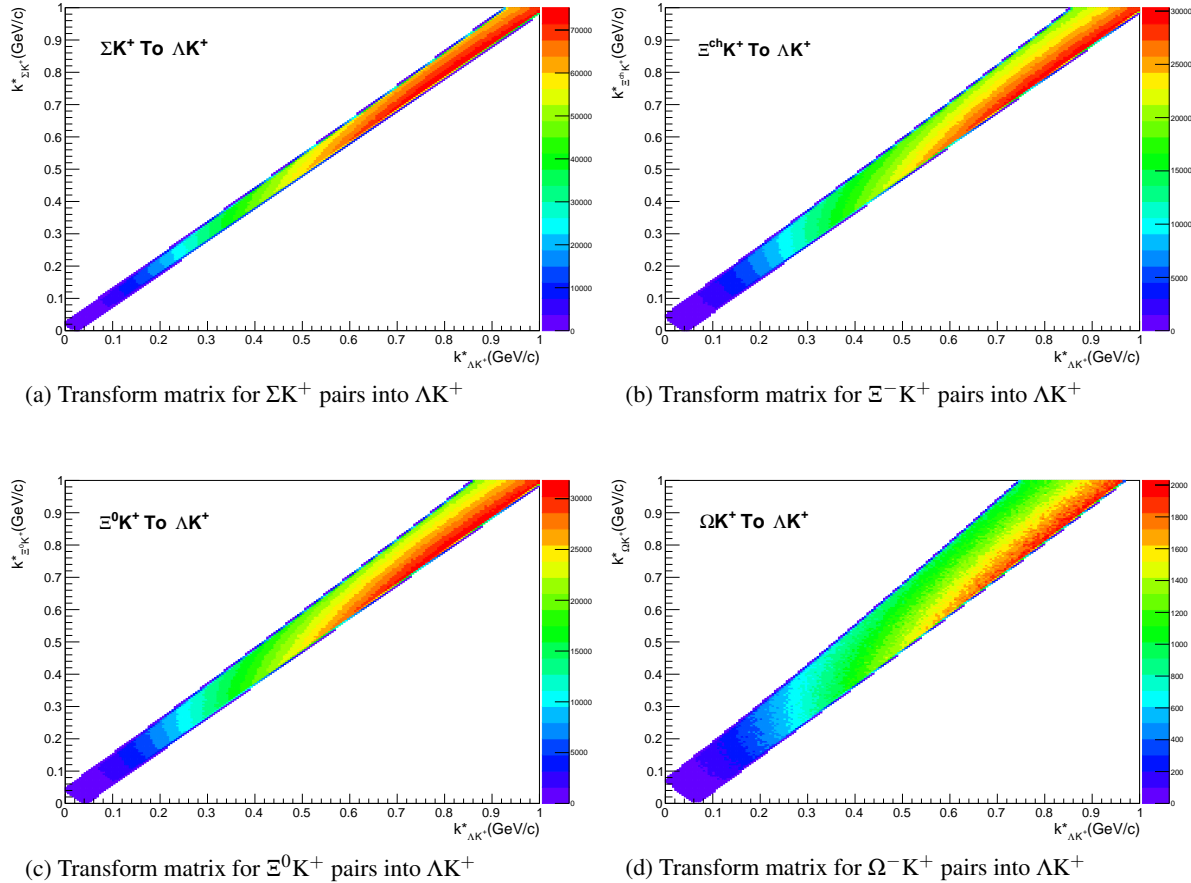


Fig. 20: Sample Transform Matrices generated with THERMINATOR for ΛK^+ Analysis

497 So, in practice, we model the correlation function of the parents (ex. $\Sigma^0 K^+$), and run the correlation
498 function through the appropriate transform matrix to determine the contribution to the daughter correla-
499 tion function (ex. ΛK^+). A few questions still remain. First, what λ values should be used in the above
500 equation? One option would be to leave all of these λ -parameters free during the fit process. However,
501 this would introduce a huge number of new parameters into the fitter, and would make the fit results less
502 trustworthy. The λ parameters roughly dictate the strength of the parent contribution to the daughter
503 pair. Additionally, as found in [7], the reconstruction efficiency for primary Λ particles is nearly equal
504 to that of Λ particles originating from Σ , Σ^* , Ξ^0 , Ξ^- , and Ω hyperons. Therefore, the λ parameter for

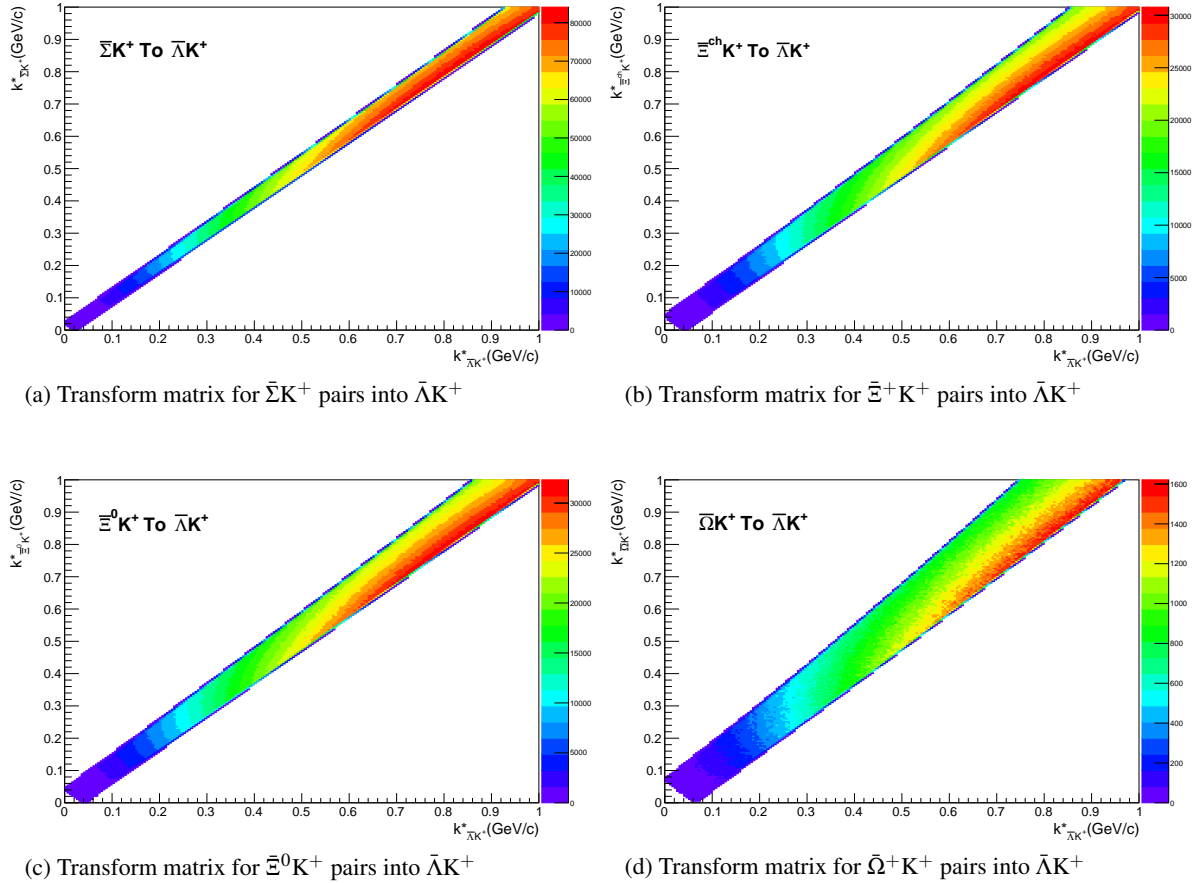


Fig. 21: Sample Transform Matrices generated with THERMINATOR for $\bar{\Lambda}K^+$ Analysis

parent system AB can be estimated using THERMINATOR as the total number of ΛK pairs originating from AB (N_{AB}) divided by the total number of ΛK pairs (N_{Total}):

$$\lambda_{AB} = \frac{N_{AB}}{N_{Total}} \quad (18)$$

Note, for our study, we consider a particle to be primary if its parent has a proper decay length of < 4 fm. The λ values used can be found in Table 1, for the case of both three and ten residual contributors. In the table, we also list the λ values used for “Other” and “Fakes”. The “Other” category contains pairs which are not primary, and which do not originate from the (3 or 10) residual pairs included in the fit. The “Fakes” category represents pairs that are mistakenly identified as ΛK . To estimate this λ_{Fakes} value, we assumed that the number of fake pairs was equal to the total number of pairs multiplied by the Λ purity (i.e. assuming perfect purity for the kaons); or, more simply, $\lambda_{Fakes} = 1.0 - \text{Purity}(\Lambda)$. For both of these contributors (“Other” and “Fakes”), we assume that these correlations average to unity, and therefore do not contribute to the final correlation function.

ΛK^+ residuals		$\bar{\Lambda}K^-$ residuals		ΛK^- residuals		$\bar{\Lambda}K^+$ residuals		ΛK_S^0 residuals		$\bar{\Lambda}K_S^0$ residuals	
Pair System	λ value	Pair System	λ value	Pair System	λ value	Pair System	λ value	Pair System	λ value	Pair System	λ value
3 Residuals											
ΛK^+	0.154	$\bar{\Lambda}K^-$	0.158	ΛK^-	0.154	$\bar{\Lambda}K^+$	0.158	ΛK_S^0	0.165	$\bar{\Lambda}K_S^0$	0.169
$\Sigma^0 K^+$	0.099	$\bar{\Sigma}^0 K^-$	0.102	$\Sigma^0 K^-$	0.099	$\bar{\Sigma}^0 K^+$	0.103	$\Sigma^0 K_S^0$	0.107	$\bar{\Sigma}^0 K_S^0$	0.111
$\Xi^0 K^+$	0.072	$\bar{\Xi}^0 K^-$	0.067	$\Xi^0 K^-$	0.071	$\bar{\Xi}^0 K^+$	0.068	$\Xi^0 K_S^0$	0.077	$\bar{\Xi}^0 K_S^0$	0.073
$\Xi^- K^+$	0.069	$\bar{\Xi}^+ K^-$	0.065	$\Xi^- K^-$	0.068	$\bar{\Xi}^+ K^+$	0.066	$\Xi^- K_S^0$	0.075	$\bar{\Xi}^+ K_S^0$	0.071
Other	0.558	Other	0.560	Other	0.561	Other	0.557	Other	0.528	Other	0.528
Fakes	0.048	Fakes	0.048	Fakes	0.048	Fakes	0.048	Fakes	0.048	Fakes	0.048
10 Residuals											
ΛK^+	0.154	$\bar{\Lambda}K^-$	0.158	ΛK^-	0.154	$\bar{\Lambda}K^+$	0.158	ΛK_S^0	0.165	$\bar{\Lambda}K_S^0$	0.169
$\Sigma^0 K^+$	0.099	$\bar{\Sigma}^0 K^-$	0.102	$\Sigma^0 K^-$	0.099	$\bar{\Sigma}^0 K^+$	0.103	$\Sigma^0 K_S^0$	0.107	$\bar{\Sigma}^0 K_S^0$	0.111
$\Xi^0 K^+$	0.072	$\bar{\Xi}^0 K^-$	0.067	$\Xi^0 K^-$	0.071	$\bar{\Xi}^0 K^+$	0.068	$\Xi^0 K_S^0$	0.077	$\bar{\Xi}^0 K_S^0$	0.073
$\Xi^- K^+$	0.069	$\bar{\Xi}^+ K^-$	0.065	$\Xi^- K^-$	0.068	$\bar{\Xi}^+ K^+$	0.066	$\Xi^- K_S^0$	0.075	$\bar{\Xi}^+ K_S^0$	0.071
$\Sigma^{*+} K^+$	0.046	$\bar{\Sigma}^{*-} K^-$	0.046	$\Sigma^{*+} K^-$	0.046	$\bar{\Sigma}^{*-} K^+$	0.046	$\Sigma^{*+} K_S^0$	0.050	$\bar{\Sigma}^{*-} K_S^0$	0.050
$\Sigma^{*-} K^+$	0.042	$\bar{\Sigma}^{*+} K^-$	0.045	$\Sigma^{*-} K^-$	0.041	$\bar{\Sigma}^{*+} K^+$	0.045	$\Sigma^{*-} K_S^0$	0.045	$\bar{\Sigma}^{*+} K_S^0$	0.049
$\Sigma^{*0} K^+$	0.042	$\bar{\Sigma}^{*0} K^-$	0.040	$\Sigma^{*0} K^-$	0.041	$\bar{\Sigma}^{*0} K^+$	0.041	$\Sigma^{*0} K_S^0$	0.045	$\bar{\Sigma}^{*0} K_S^0$	0.044
ΛK^{*0}	0.039	$\bar{\Lambda}K^{*0}$	0.041	$\Lambda \bar{K}^{*0}$	0.039	$\bar{\Lambda}K^{*0}$	0.041	ΛK^{*0}	0.019	$\bar{\Lambda}K^{*0}$	0.020
$\Sigma^0 K^{*0}$	0.035	$\bar{\Sigma}^0 \bar{K}^{*0}$	0.036	$\Sigma^0 \bar{K}^{*0}$	0.035	$\bar{\Sigma}^0 K^{*0}$	0.036	$\Sigma^0 K^{*0}$	0.017	$\bar{\Sigma}^0 K^{*0}$	0.017
$\Xi^0 K^{*0}$	0.025	$\bar{\Xi}^0 \bar{K}^{*0}$	0.024	$\Xi^0 \bar{K}^{*0}$	0.025	$\bar{\Xi}^0 K^{*0}$	0.024	$\Xi^0 K^{*0}$	0.012	$\bar{\Xi}^0 K^{*0}$	0.011
$\Xi^- K^{*0}$	0.024	$\bar{\Xi}^+ \bar{K}^{*0}$	0.023	$\Xi^- \bar{K}^{*0}$	0.024	$\bar{\Xi}^+ K^{*0}$	0.023	$\Xi^- K^{*0}$	0.012	$\bar{\Xi}^+ K^{*0}$	0.011
Other	0.305	Other	0.305	Other	0.308	Other	0.301	Other	0.329	Other	0.326
Fakes	0.048	Fakes	0.048	Fakes	0.048	Fakes	0.048	Fakes	0.048	Fakes	0.048

Table 1: λ values for the individual components of the ΛK correlation functions for the case of 3 and 10 residual contributions.

Now, the remaining question is how do we model the parent correlation functions? In an ideal world, we would simply look up the parent interaction in some table, and input this into our Lednicky equation (for the case of one or more charge neutral particle in the pair), or run it through the CoulombFitter machinery described in Sec.5.2. Unfortunately, the world in which we live is not perfect, such a table does not exists, and little is know about the interaction between the residual pairs in this study. One solution would be to introduce a set of scattering parameters and radii for each residual system. However, as was the case of the λ -parameters above, this would introduce a large number of additional fit parameters, and would make our fitter too unconstrained and would yield untrustworthy results. The second option, which is adopted in this analysis, is to assume all residual pairs have the same source size as the daughter pair, and all Coulomb-neutral residual pairs also share the same scattering parameters as the daughter pair (the case of charged pairs, such as $\Xi^- K^\pm$ or $\Sigma^{*\pm} K^\pm$, will be described below).

Concerning the radii of the residual parent pairs, it was suggested that these should be set to smaller values than those of the daughter pair. In the interest of minimizing the number of parameters in the fitter, we tested this by introducing an m_T -scaling of the parents' radii. The motivation for this scaling comes from the approximate m_T -scaling of the radii observed in ???. To achieve this scaling, we assume the radii follow an inverse-square-root distribution: $R_{AB} = \alpha m_T^{-1/2}$. Then, it follows that we should scale the parent radii as:

$$R_{AB} = R_{\Lambda K} \left(\frac{m_{T,AB}}{m_{T,\Lambda K}} \right)^{-1/2} \quad (19)$$

The values of m_T for each pair system were taken from THERMINATOR. As the fitter dances around parameter space and selects a new radius for the ΛK system, the radii of the residuals is simply the ΛK radius scaled by the appropriate factor, given above (Eq.19). In the end, this scaling factor made no significant difference in our fit results, so this complication is excluded from our final results. Note that this is not surprising, as the most extreme scaling factor was, in the case of using 10 residual systems, between $\Lambda K+$ with $m_{T,\Lambda K+} \approx 1.4 \text{ GeV}/c^2$ and $\Xi^- K^{*0}$ with $m_{T,\Xi^- K^{*0}} \approx 1.8 \text{ GeV}/c^2$, resulting in a scale factor of ≈ 0.9 .

Now, as hinted above, accounting for charged residuals adds a complication in that they necessitate the inclusion of the CoulombFitter (described in Sec. 5.7) into the process. The complication of combining the two fitters is not troubling; however, the substantial increase in the fitting time is (the parallelization of the CoulombFitter across a large number of GPU cores, to drastically decrease run-time, is currently underway). We have two solutions to bypass such a large increase in run time. First, we can use our experimental $\Xi^{ch} K^{ch}$ data to represent all charged parent pair system. In this case, there is no need to make any assumption about scattering parameters or source sizes, as we already have the experimental data. The downside is that, especially in the 30-50% centrality bin, the statistics are low and error bars large. Alternatively, we can assume the strong interaction is negligible in the charged residual, and generate the parent correlation function given radius and λ parameters. We find in our $\Xi^{ch} K^{ch}$ study that a Coulomb-only description of the system describes, reasonably well, the broad features of the correlation. The strong interaction is necessary for the fine details. However, as these correlations are run through a transform matrix, which largely flattens out and fine details, a Coulomb-only description should be sufficient. In practice, this Coulomb-only scenario is achieved by first building a large number of Coulomb-only correlations for various radii and λ parameter values, and interpolating from this grid during the fitting process. We find consistent results between using the ΞK data and the Coulomb-only interpolation method. When quantifying the $\Xi^- K^\pm$ residual contribution, the experimental $\Xi^- K^\pm$ data is always used. When the number of residual pairs used is increased to 10, so that contributors such as $\Sigma^{*+} K^-$ enter the picture, the Coulomb-only interpolation method is used. In other words, the ΞK experimental data is only used to model the ΞK residual contribution, all other charged pairs are treated with the Coulomb-only interpolation method.

561 Two examples of how very different transform matrices can alter a correlation function are shown in
 562 Figures 22 and 23 below. These figures were taken using parameter values obtained from fits to the data.
 563 In the top left corner of the figures, the input correlation function (closed symbols) is shown together
 564 with the output, transformed, correlation function (open symbols). In the bottom left, the transformed
 565 correlation is shown by itself (with zoomed y-axis). This is especially helpful when the λ parameter is
 566 very small, in which case the contribution in the top left can look flat, but the zoomed in view in the
 567 bottom left shows the structure. The right two plots in each figure show the transform matrix without
 568 (top right) and with (bottom right) a log-scale on the z-axis. Note, more examples of these transforms
 569 can be found in Sec. 9.

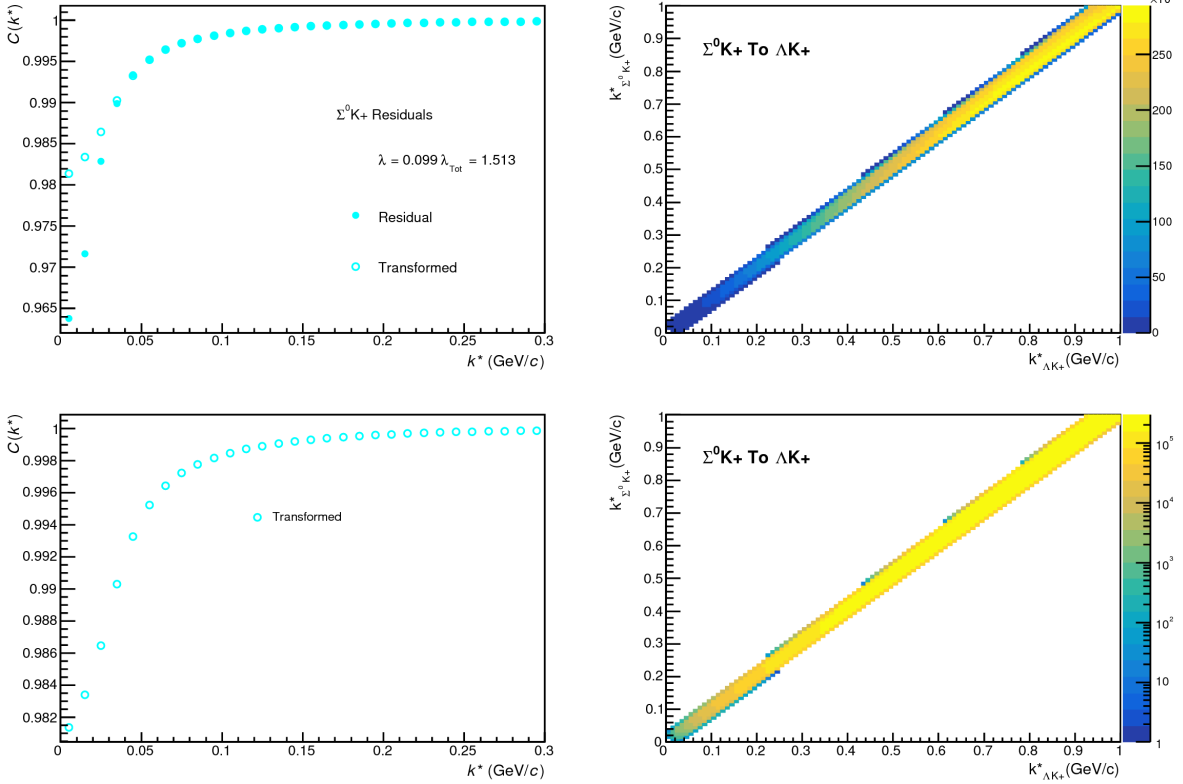


Fig. 22: $\Sigma^0 K^+$ Transform. These figures were taken using parameter values obtained from fits to the data. In the top left corner of the figures, the input correlation function (closed symbols) is shown together with the output, transformed, correlation function (open symbols). In the bottom left, the transformed correlation is shown by itself. The right two plots in each figure show the transform matrix without (top right) and with (bottom right) a log-scale on the z-axis.

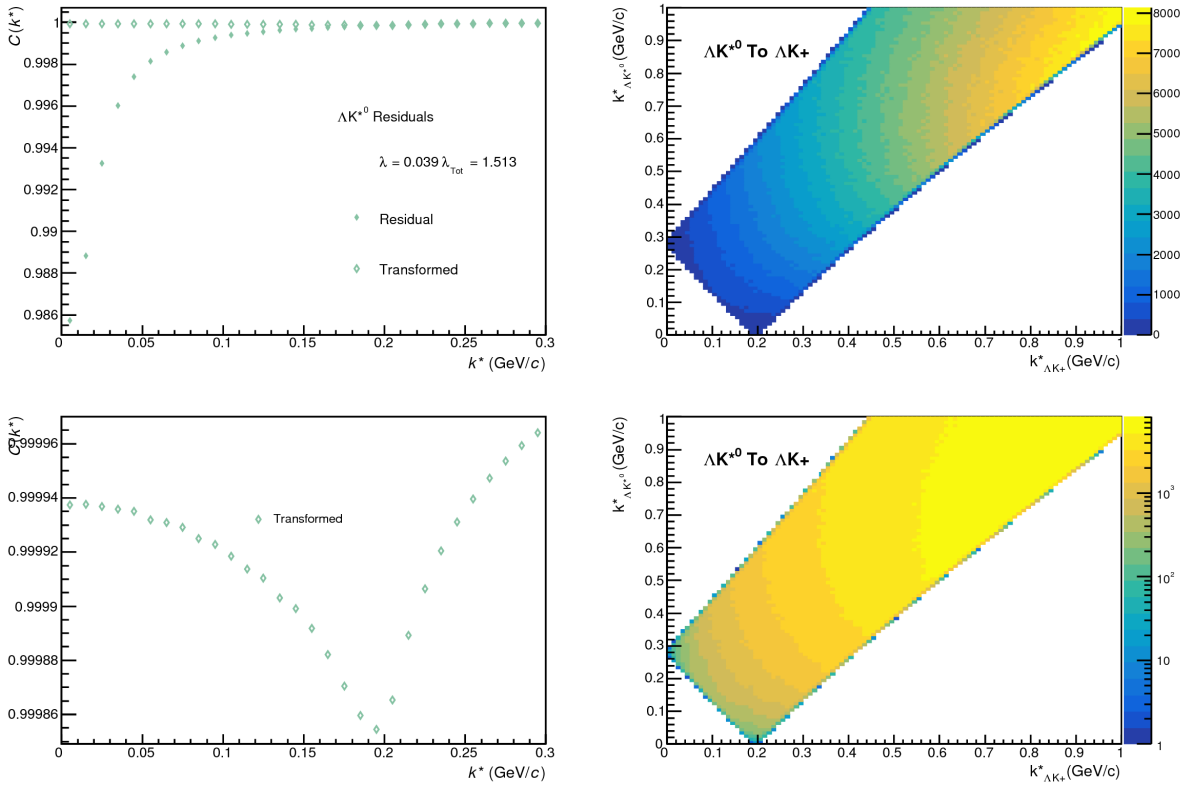


Fig. 23: ΔK^{*0} Transform. These figures were taken using parameter values obtained from fits to the data. In the top left corner of the figures, the input correlation function (closed symbols) is shown together with the output, transformed, correlation function (open symbols). In the bottom left, the transformed correlation is shown by itself. The right two plots in each figure show the transform matrix without (top right) and with (bottom right) a log-scale on the z-axis.

570 5.5 Non-Flat Background

571 We observe a significant non-femtoscopic, non-flat, background in all of our correlations at large k^* .
 572 This background increases with decreasing centrality, is the same amongst all ΛK^\pm pairs, and is more
 573 pronounced in the ΛK_S^0 system, as can be seen in Fig. 24. Figure 25a shows that THERMINATOR 2
 574 simulation does a good job of describing the difference in backgrounds between ΛK^\pm and ΛK_S^0 .

575 Before beginning, it is important to note that the difference in ΛK^\pm and ΛK_S^0 backgrounds is due mainly
 576 to the difference in kinematic cuts, not due to any interesting physics. Figure 25b shows that, for THER-
 577 MINATOR simulation, when restrictions are imposed on the p_T of the K_S^0 to more closely match the
 578 K^\pm cuts, the backgrounds align much better. Therefore, we conclude that the difference in background
 579 between ΛK^\pm and ΛK_S^0 observed in our experimental data is simply due to a difference in kinematic cuts
 580 between K^\pm and K_S^0 particles.

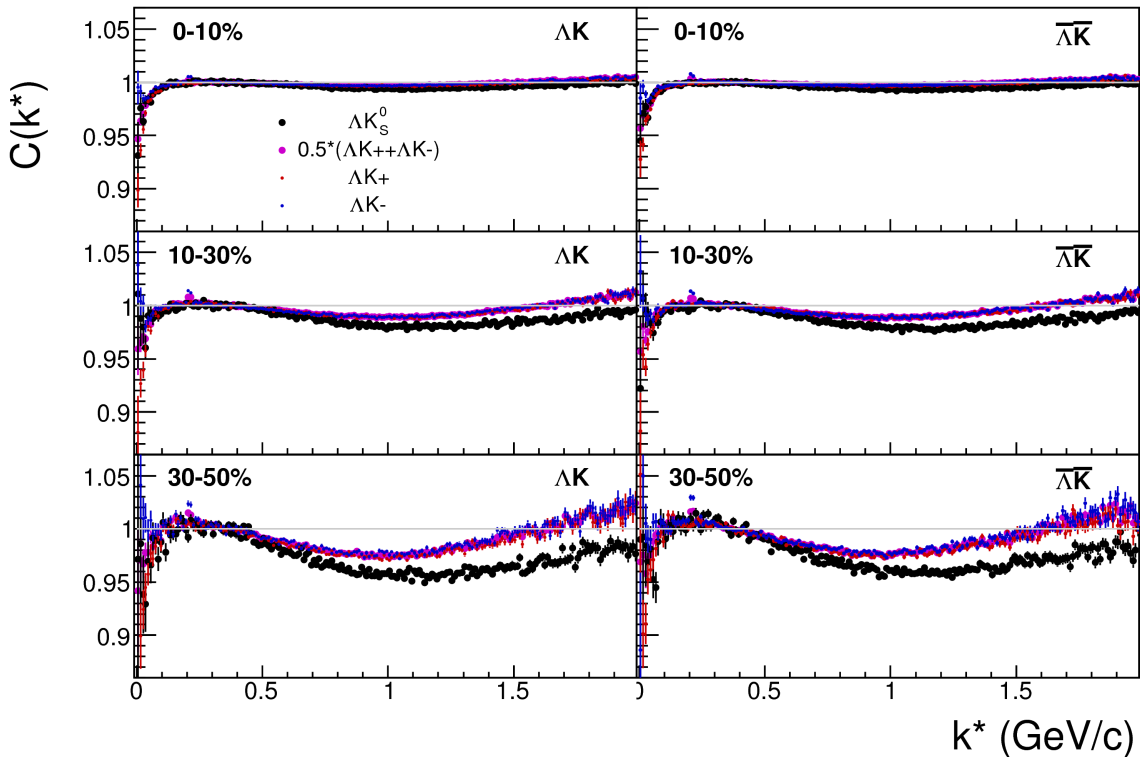


Fig. 24: A comparison on the non-femtoscopic backgrounds observed in our ΛK experimental data.

581 It is suggested that this background effect is due primarily to particle collimation associated with elliptic
 582 flow [8]. More specifically, these backgrounds result from mixing events with unlike event-plane angles
 583 (Ψ_{EP}). As explained in [8], when elliptic flow is present, all particles are more likely to be emitted
 584 in a specific direction (in-plane), as opposed to a perpendicular direction. Therefore, the difference in
 585 momenta for pairs of particles tends to be smaller, compared to the case of no flow. In the case of mixed-
 586 event pairs, the two events used do not share an event-plane, and therefore there is no collimation effect
 587 in the pairs from flow. As a result, pairs with larger momentum are more likely when mixed-events are
 588 used, causing the correlation function to be observed below unity. In general, a dip below unity, at a given
 589 k^* , means it is more probable to find a pair at that k^* when the daughters are taken from mixed-events, as
 590 compared to when they are taken from the same event.

591 This same reasoning suggests that the background should lead to an enhancement at low- k^* . The en-
 592 hancement at high- k^* ($k^* \gtrsim 1.5$ GeV/c) does not result from the collective flow of the system. We are not

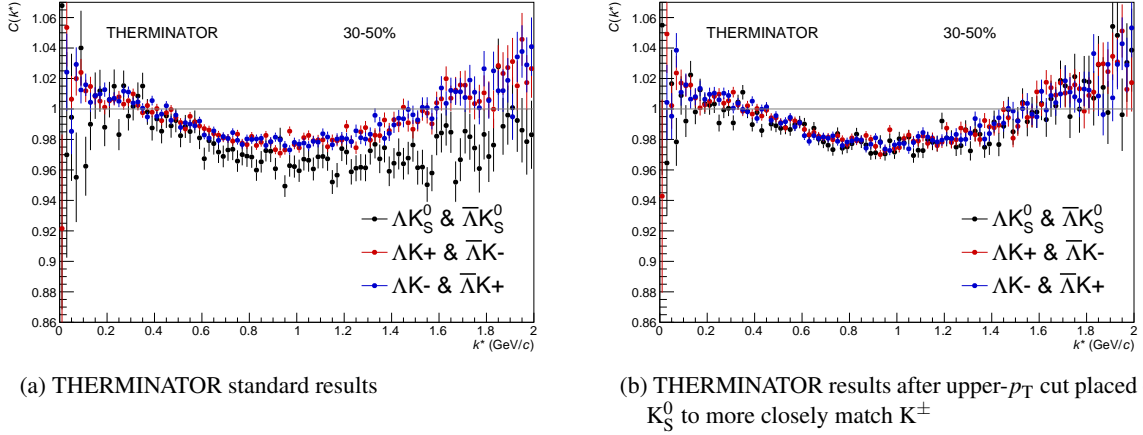


Fig. 25: THERMINATOR 2 simulation for ΛK^+ (red), ΛK^- (blue), and ΛK_S^0 (black). In 25a, we show the standard THERMINATOR 2 results. THERMINATOR 2 does a good job describing qualitatively the difference between the ΛK^\pm and ΛK_S^0 backgrounds. In 25b, an upper- p_T cut was placed on the K_S^0 particles to more closely match the K^\pm kinematic cuts. After this tweak, the ΛK^\pm and ΛK_S^0 backgrounds agree much better.

593 certain causes this enhancement, but typical suspects are jet-like correlations and resonance decays.

594 We can split our correlation functions into three main regions. First, the low- k^* region ($k^* \lesssim 0.3$ GeV/c)
 595 contains the femtoscopic correlations, as well as a likely enhancement from the background. The
 596 intermediate- k^* region ($0.3 \lesssim k^* \gtrsim 1.5$ GeV/c) contains a suppression from the background. Finally,
 597 the high- k^* region ($k^* \gtrsim 1.5$ GeV/c) contains an enhancement with unknown origin.

598 THERMINATOR 2 simulation has been shown to reproduce the background features in a πK analysis
 599 [8]. As the background effect can be attributed mainly to elliptic flow, which is a global feature of the
 600 system, we suspected THERMINATOR 2 could also, at least qualitatively, describe our backgrounds.
 601 After ensuring each simulated event received a random event-plane angle (Ψ_{EP})¹, we found THERMI-
 602 NATOR 2 did a good job of describing our data qualitatively, and, in many cases, quantitatively. Figure
 603 26 shows the THERMINATOR 2 simulation (gold) together with experimental data (red, blue, or black)
 604 The figure also shows a 6th-order polynomial fit to the simulation (gold), as well as the fit polynomial
 605 scaled to match the data (red, blue, black).

606 Figure 27 shows three different correlation function generated using THERMINATOR 2 simulation (“Cf
 607 w/o Bgd (A)”, “Cf w. Bgd (B)”, “Bgd(C)”), as well as two histograms describing the relation between
 608 the three (“Ratio (B/C)”, “1+Diff(B-C)”). “Cf w/o Bgd (A)” shows a correlation function with a femto-
 609 scopic correlation, but without background. When THERMINATOR 2 is run without randomizing event
 610 planes, and therefore having all events share a common event plane, no background is observed, as ex-
 611 pected. The femtoscopic correlation effect was introduced by assuming a set of scattering parameters for
 612 the system, and weighting the numerators appropriately. The second correlation, ”Cf w. Bgd (B)”, shows
 613 a correlation function with both a femtoscopic correlation and a background (most closely matches our
 614 situation in experiment). To generate the background, each event was given a random event-plane angle,
 615 as is given to us in experiment. To generate the femtoscopic correlation, the same numerator weighting
 616 procedure was used. Finally, ”Bgd (C)”, shows a correlation function with a non-femtoscopic back-
 617 ground, but no femtoscopic correlation, i.e. background only. This is generated just as ”Cf w. Bgd (B)”,
 618 with randomized event planes, but unit weights are used when filling the numerators, so no femtoscopic
 619 effects are included.

¹default was for all events to share a common event plane

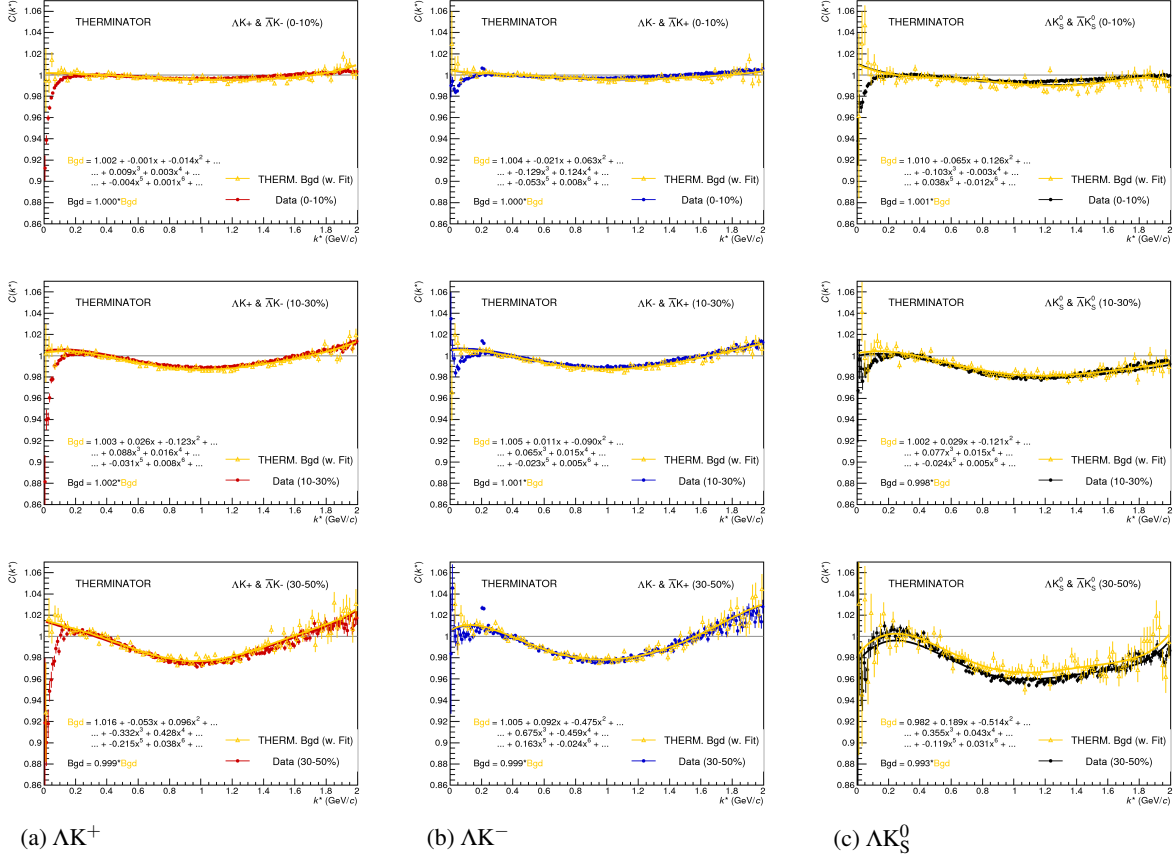


Fig. 26: THERMINATOR 2 simulation (gold) together with experimental data (red, blue, or black). The left column shows results for ΛK^+ (26a), middle for ΛK^- (26b), and right for ΛK_S^0 (26c). A 6th-order polynomial fit to the simulation is shown as a solid gold line, and whose fit parameters are printed on the lower left of each plot. This polynomial is scaled to match the experimental data; the value of this scale is printed in the lower left corner of each plot. The polynomial fit with scale factor applied is drawn in a color matching the experimental data (red, blue, black).

620 The main point of Fig. 27 is that the black points match the blue (and purple) points; or, equivalently:

$$C_{fw/oBgd} = \frac{C_{fw.Bgd}}{Bgd} \rightarrow C_{theory} = \frac{C_{exp}}{F_{Bgd}} \rightarrow C_{exp} = C_{theory} \cdot F_{Bgd} \quad (20)$$

621 As shown and described in Fig 27 and Eq. 20, THERMINATOR 2 simulation shows the non-femtoscopic
 622 background affects the correlation function as a separable scale factor. We expect this behavior to be
 623 roughly the same in the experimental data.

624 Figure 28 demonstrates the use of the Stavinsky method with THERMINATOR 2. In the figure, unit
 625 weights were used for all numerators, so no femtoscopic signal is included, only background effects.
 626 The black points show an ideal, experimentally unreachable, situation of aligning all of the event-plane
 627 angles. With THERMINATOR 2, when the event-planes are aligned, the background signal is killed.
 628 The green points show the case of random event-plane angles, a situation more closely matching that
 629 of experiment. The purple points show the affect of applying the Stavinsky method to the case of
 630 random event-planes. The figure shows that this method effectively kills the non-flat background (i.e.
 631 the procedure takes the green points to the purple). Finally, the blue points show the effect of applying
 632 the Stavinsky method when all of the event-planes are aligned. This shows that the Stavinsky method

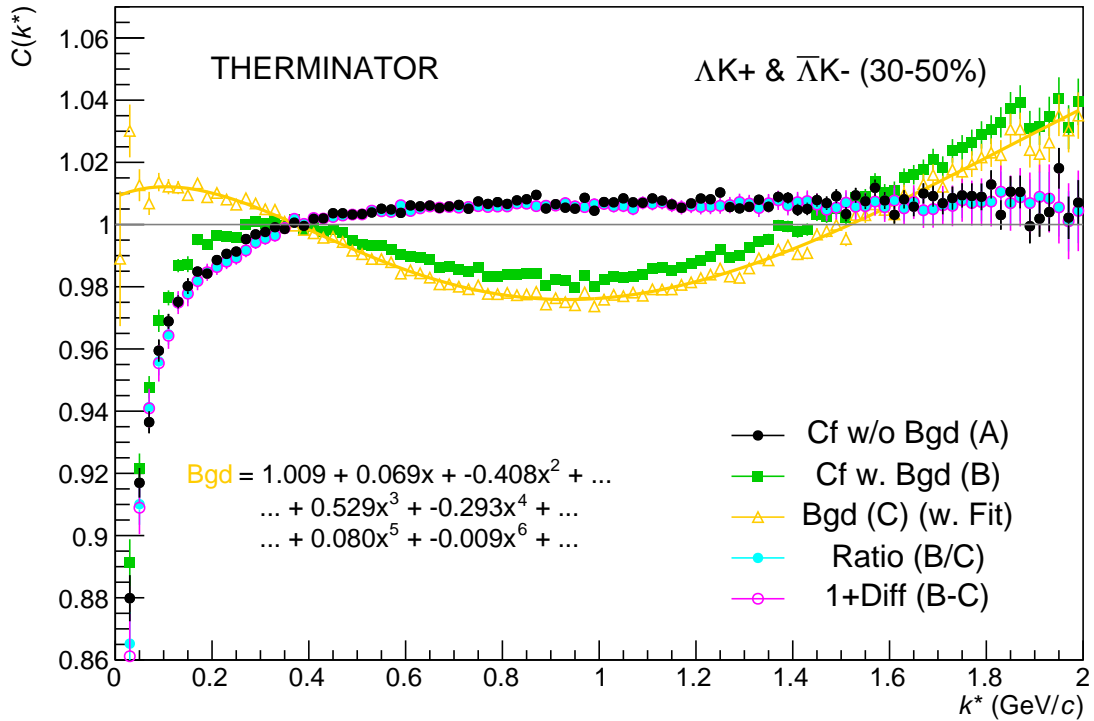


Fig. 27: Correlation with background decomposition with THERMINATOR. "Cf w/o Bgd (A)" shows a correlation function with a femtoscopic correlation, but without background. "Cf w. Bgd (B)", shows a correlation function with both a femtoscopic correlation and a background (most closely matches our situation in experiment). "Bgd (C)", shows a correlation function with a non-femtoscopic background, but no femtoscopic correlation, i.e. background only.

633 does not introduce any signal to an already flat background.

634 5.6 LednickyFitter

635 The code developed to fit the data is called "LednickyFitter", and utilizes the ROOT TMinuit implemen-
 636 tation of the MINUIT fitting package. In short, given a function with a number of parameters, the fitter
 637 explores the parameter space searching for the minimum of the function. In this implementation, the
 638 function to be minimized should represent the difference between the measured and theoretical corre-
 639 lation functions. However, a simple χ^2 test is inappropriate for fitting correlation functions, as the ratio of
 640 two Poisson distributions does not result in a Poisson distribution. Instead, a log-likelihood fit function
 641 of the following form is used [2]:

$$\chi_{PML}^2 = -2 \left[A \ln \left(\frac{C(A+B)}{A(C+1)} \right) + B \ln \left(\frac{A+B}{B(C+1)} \right) \right] \quad (21)$$

642 where A is the experimental signal distribution (numerator), B is the experimental background distribu-
 643 tion (denominator), and C is the theoretical fit correlation function.

644 The LednickyFitter uses Equations 5 – 7 to build the theoretical fit, and Equation 21 as the statistic
 645 quantifying the quality of the fit. The parameters to be varied by MINUIT are: λ , R , f_0 ($\mathbb{R}f_0$ and $\mathbb{I}f_0$
 646 separately), d_0 , and normalization N . The fitter currently includes methods to correct for momentum
 647 resolution and a non-flat background. These corrections are applied to the fit function, the data is never

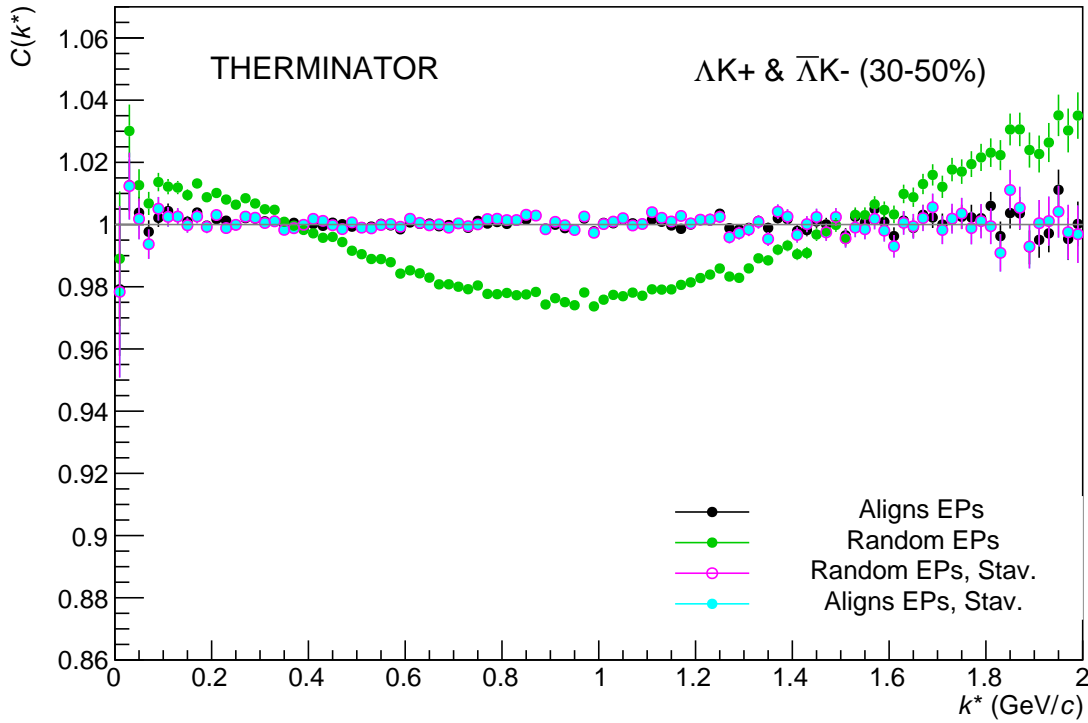


Fig. 28: The use of the Stavinsky method with THERMINATOR 2. Unit weights were used for all numerators, so no femtoscopic signal is included, only background effects. The black points show an ideal, experimentally unreachable, situation of aligning all of the event-plane angles. The green points show the experimental situation of random event-plane angles. The purple points show the affect of applying the Stavinsky method to the case of random event-planes. Finally, the blue points show the effect of applying the Stavinsky method when all of the event-planes are aligned.

- 648 touched. The fitter is able to share parameters between different analyses and fit all simultaneously.
- 649 In a typical fit, a given pair is fit with its conjugate (ex. ΛK^+ with $\bar{\Lambda} K^-$) across all centralities (0-10%,
650 10-30%, 30-50%), for a total of 6 simultaneous analyses. Each analysis has a unique λ and normalization
651 parameter. The radii are shared between analyses of like centrality, as these should have similar source
652 sizes. The scattering parameters ($\mathbb{R}f_0$, $\mathbb{I}f_0$, d_0) are shared amongst all.
- 653 Initially, we left open the possibility for the $\Lambda K^+(\bar{\Lambda} K^-)$ and $\Lambda K^-(\bar{\Lambda} K^+)$ systems to have different source
654 radii. After always finding these two to be consistent, we decided to join the radii parameters between these
655 systems. So, now, in a typical fit of our ΛK^\pm data, all ΛK^\pm analyses (ΛK^+ , $\bar{\Lambda} K^-$, ΛK^- , $\bar{\Lambda} K^+$) are fit
656 simultaneously across all centralities. Scattering parameters are shared between pair-conjugate systems
657 (i.e. a parameter set describing the $\Lambda K^+ & \bar{\Lambda} K^-$ system, and a separate set describing the $\Lambda K^- & \bar{\Lambda} K^+$
658 system). For each centrality, a radius and λ parameters are shared amongst all pairs. Each analysis has a
659 unique normalization parameter.
- 660 In the case of fitting with residuals, the λ_{Fit} parameter serves as an overall normalization shared by all
661 contributors, such that Eqn 17 becomes:

$$\begin{aligned}
C_{measured}(k_{\Lambda K}^*) &= 1 + \sum_i \lambda'_i [C_i(k_{\Lambda K}^*) - 1] \\
\lambda'_i &= \lambda_{Fit} \lambda_i \\
\sum_i \lambda'_i &= \lambda_{Fit} \sum_i \lambda_i = \lambda_{Fit}
\end{aligned} \tag{22}$$

where λ_i is obtained from THERMINATOR, as explained in Section 5.4, and whose values are presented in Tables ?? through ???. For Coulomb-neutral pairs, such as ΛK , $\Sigma^0 K$, and $\Xi^0 K$, $C_i(k_{\Lambda K}^*)$ is calculated from Eqn. 5, with the help of Eqn. 7. For those residual pairs which include a Coulomb interaction, $C_i(k_{\Lambda K}^*)$ is either calculated using the CoulombFitter method (Sections 5.2 and 5.7) with no strong interaction, or by using the $\Xi^{ch} K^{ch}$ data directly. Unless otherwise stated, the $\Xi^{ch} K^{ch}$ residual contribution is modeled using the experimental $\Xi^{ch} K^{ch}$ data, and all other charged contributors (ex. $\Sigma^{*ch} K^{ch}$) are modeled using the CoulombFitter technique with no strong interaction contribution.

To summarize, the complete fit function is constructed as follows:

1. The uncorrected, primary, correlation function, $C_{\Lambda K}(k_{True}^*)$, is constructed using Eq. 22 (with the help of Eqns. 5 and 7)
2. If residuals are included:
 - the parent correlation functions are obtained using:
 - Eq. 22 (with the help of Eqns. 5 and 7) for the case of Coulomb-neutral pairs
 - $\Xi^- K^\pm$ experimental data for $\Xi^- K^\pm$ contributions
 - a Coulomb-only curve, with the help of Secs. 5.2 and 5.7, for pairs including the Coulomb interaction
 - the contribution to the ΛK correlation function is found by running the parent correlation function through the appropriate transform, via Eq.16
3. The primary and residual correlations are combined, via Eq.17, to form $C'_{Fit}(k_{True}^*)$
 - in the case of no residual contributions included in the fit, $\lambda_i = \lambda_{\Lambda K}$ in Eq. 22 is set equal to 1. Then, the extracted λ_{Fit} parameter should be roughly equal to the pair purity
 - when residuals are included, the λ_i values are presented in Table 1
4. The correlation function is corrected to account for momentum resolution effects using Eq. 14

$$C'_{fit}(k_{Rec}^*) = \frac{\sum_{k_{True}^*} M_{k_{Rec}, k_{True}^*} C'_{fit}(k_{True}^*)}{\sum_{k_{True}^*} M_{k_{Rec}, k_{True}^*}}$$

5. Finally, the non-flat background correction is applied, and the final fit function is obtained
 - $C_{Fit}(k_{Rec}^*) = C'_{Fit}(k_{Rec}^*) * F_{Bgd}(k_{Rec}^*)$

Figures 32, 33, and 34 (37, 38, and 39, or 44, 45, and 46), in Section 7, show experimental data with fits for all studied centralities for $\Lambda K_S^0 (\bar{\Lambda} K_S^0)$, $\Lambda K^+ (\bar{\Lambda} K^-)$, and $\Lambda K^- (\bar{\Lambda} K^+)$, respectively. In the figures, the black solid line represents the “raw” fit, i.e. not corrected for momentum resolution effects nor non-flat background. The green line shows the fit to the non-flat background. The purple points show the fit after momentum resolution, non-flat background, and residual correlations (if applicable) corrections have been applied. The extracted fit values with uncertainties are also printed on the figures.

694 5.7 Coulomb Fitter

695 When fitting the $\Xi^-(\bar{\Xi}^+)K^\pm$ results, it is necessary to include both strong and Coulomb effects. In this
 696 case, Equation 5 is no longer valid, and, in fact, there is no analytical form with which to fit. We therefore
 697 must take a more basic approach, and integrate out Eq.4 by hand. To achieve this, one has two options.
 698 The first option is to numerically integrate Eq.4. The second option is to simulate a large sample of
 699 particle pairs, calculate the wave function describing the interaction, and average to obtain the integral.
 700 Having no experience with either of these options, we elected the latter of simulating pairs. The code
 701 developed to achieve this functionality is called “CoulombFitter”. Currently, in order to generate the
 702 statistics needed for a stable fit, we find that $\sim 10^4$ simulated pairs per 10 MeV bin are necessary. The
 703 nature of this process means that the “CoulombFitter” takes much longer to run than the “LednickyFitter”
 704 of Section 5.1.

705 Unfortunately, with this analysis, we are not sensitive to, and therefore not able to distinguish between,
 706 the iso-spin singlet and triplet states. We proceed with our analysis, but the results must be interpreted
 707 as iso-spin averaged scattering parameters.

708 As stated before, to generate a fit correlation function, we must simulate a large number of pairs, calculate
 709 the wave-function, and average Ψ^2 over all pairs in a given k^* bin. Essentially, we calculate Equation 9
 710 by hand:

$$\begin{aligned} C(\mathbf{k}^*) &= \sum_S \rho_S \int S(\mathbf{r}^*) |\Psi_{\mathbf{k}^*}^S(\mathbf{r}^*)|^2 d^3 \mathbf{r}^* \\ &\longrightarrow C(|\mathbf{k}^*|) \equiv C(k^*) = \sum_S \rho_S \langle |\Psi^S(\mathbf{k}_i^*, \mathbf{r}_i^*)|^2 \rangle_i \\ &\longrightarrow C(k^*) = \lambda \sum_S \rho_S \langle |\Psi^S(\mathbf{k}_i^*, \mathbf{r}_i^*)|^2 \rangle_i + (1 - \lambda) \end{aligned} \quad (23)$$

711 where $\langle \rangle_i$ represents an average over all pairs in a given k^* bin.

712 In summary, for a given k^* bin, we must draw $N_{pairs} \sim 10^4$ pairs, and for each pair:

- 713 1. Draw a random \mathbf{r}^* vector according to our Gaussian source distribution $S(\mathbf{r}^*)$
- 714 2. Draw a random \mathbf{k}^* vector satisfying the $|\mathbf{k}^*|$ restriction of the bin
 - 715 – We draw from real k^* vectors obtained from the data
 - 716 – However, we find that drawing from a distribution flat in k^* gives similar results
- 717 3. Construct the wave-function Ψ

718 After all pairs for a given k^* bin are simulated and wave-functions obtained, the results are averaged to
 719 give the fit result.

720 Construction of the wave-functions, Equation 10, involves a number of complex functions not included
 721 in standard C++ or ROOT libraries (namely, $h(\eta)$, $\tilde{G}(\rho, \eta)$), and $F(-i\eta, 1, i\xi)$. These functions were
 722 even difficult to find and implement from elsewhere. Our solution was to embed a Mathematica kernel
 723 into our C++ code to evaluate these functions. However, having Mathematica work on-the-fly with the
 724 fitter was far too time consuming (fitter would have taken days, maybe weeks to finish). Our solution
 725 was to use Mathematica to create matrices representing these functions for different parameter values.
 726 During fitting, these matrices were then interpolated and the results used to build the wave-functions.
 727 This method decreased the running time dramatically, and we are not able to generate results in under \sim
 728 1 hour. This process will be explained in more detail in future versions of the note.

729 **6 Systematic Errors**

730 In order to understand my systematic uncertainties, the analysis code was run many times using slightly
 731 different values for a number of important cuts, and the results were compared. To quantify the systematic
 732 errors on the data, all correlation functions built using all varied cut values were bin-by-bin averaged,
 733 and the resulting variance of each bin was taken as the systematic error. The cuts which were utilized in
 734 this study are presented in Sections 6.1.1 (ΛK_S^0) and 6.2.1 (ΛK^\pm).

735 Similarly, the fit parameters extracted from all of these correlation functions were averaged, and the
 736 resulting variances were taken as the systematic errors for the fit parameters. As with the systematic
 737 errors on the data, this was performed for all varied cut values. Additionally, a systematic analysis was
 738 done on our fit method (which, for now, just includes our choice of fit range and functional form used to
 739 model the non-femtoscopic background). These two sources of uncertainty were combined in quadrature
 740 to obtain the final systematic uncertainties on the extracted fit parameters.

741 **6.1 Systematic Errors: ΛK_S^0**

742 **6.1.1 Particle and Pair Cuts**

743 The cuts included in the systematic study, as well as the values used in the variations, are listed below.
 744 Note, the central value corresponds to that used in the analysis.

ΛK_S^0 systematics	
DCA $\Lambda(\bar{\Lambda})$	4, 5, 6 mm
DCA K_S^0	2, 3, 4 mm
DCA $\Lambda(\bar{\Lambda})$ Daughters	3, 4, 5 mm
DCA K_S^0 Daughters	2, 3, 4 mm
$\Lambda(\bar{\Lambda})$ Cosine of Pointing Angle	0.9992, 0.9993, 0.9994
K_S^0 Cosine of Pointing Angle	0.9992, 0.9993, 0.9994
DCA to Primary Vertex of $p(\bar{p})$ Daughter of $\Lambda(\bar{\Lambda})$	0.5, 1, 2 mm
DCA to Primary Vertex of $\pi^-(\pi^+)$ Daughter of $\Lambda(\bar{\Lambda})$	2, 3, 4 mm
DCA to Primary Vertex of π^+ Daughter of K_S^0	2, 3, 4 mm
DCA to Primary Vertex of π^- Daughter of K_S^0	2, 3, 4 mm
Average Separation of Like-Charge Daughters	5, 6, 7 cm

Table 2: ΛK_S^0 systematics

745 **6.1.2 Non-Flat Background**

746 We fit our non-flat background with a linear function. To study the contribution of this choice to our sys-
 747 tematic errors, we also fit with a quadratic and Gaussian form. The resulting uncertainties are combined
 748 with the uncertainties arising from our particle cuts.

749 **6.1.3 Fit Range**

750 Our choice of k^* fit range was varied by $\pm 25\%$. The resulting uncertainties in the extracted parameter
 751 sets were combined with our uncertainties arising from our particle and pair cuts.

752 **6.2 Systematic Errors: ΛK^\pm**

753 **6.2.1 Particle and Pair Cuts**

754 The cuts included in the systematic study, as well as the values used in the variations, are listed below.
 755 Note, the central value corresponds to that used in the analysis.

ΛK^\pm systematics	
DCA $\Lambda(\bar{\Lambda})$	4, 5, 6 mm
DCA $\Lambda(\bar{\Lambda})$ Daughters	3, 4, 5 mm
$\Lambda(\bar{\Lambda})$ Cosine of Pointing Angle	0.9992, 0.9993, 0.9994
DCA to Primary Vertex of $p(\bar{p})$ Daughter of $\Lambda(\bar{\Lambda})$	0.5, 1, 2 mm
DCA to Primary Vertex of $\pi^-(\pi^+)$ Daughter of $\Lambda(\bar{\Lambda})$	2, 3, 4 mm
Average Separation of $\Lambda(\bar{\Lambda})$ Daughter with Same Charge as K^\pm	7, 8, 9 cm
Max. DCA to Primary Vertex in Transverse Plane of K^\pm	1.92, 2.4, 2.88
Max. DCA to Primary Vertex in Longitudinal Direction of K^\pm	2.4, 3.0, 3.6

Table 3: ΛK^\pm systematics

756 **6.2.2 Non-Flat Background**

757 We fit our non-flat background with a linear function. To study the contribution of this choice to our sys-
 758 tematic errors, we also fit with a quadratic and Gaussian form. The resulting uncertainties are combined
 759 with the uncertainties arising from our particle cuts.

760 **6.2.3 Fit Range**

761 Our choice of k^* fit range was varied by $\pm 25\%$. The resulting uncertainties in the extracted parameter
 762 sets were combined with our uncertainties arising from our particle and pair cuts.

763 **6.3 Systematic Errors: ΞK^\pm**

764 **6.3.1 Particle and Pair Cuts**

765 The cuts included in the systematic study, as well as the values used in the variations, are listed below.
 766 Note, the central value corresponds to that used in the analysis.

$\Xi^- K^\pm$ systematics

$\Xi^- K^\pm$ systematics	
Max. DCA $\Xi(\bar{\Xi})$	2, 3, 4 mm
Max. DCA $\Xi(\bar{\Xi})$ Daughters	2, 3, 4 mm
Min. $\Xi(\bar{\Xi})$ Cosine of Pointing Angle to Primary Vertex	0.9991, 0.9992, 0.9993
Min. $\Lambda(\bar{\Lambda})$ Cosine of Pointing Angle to $\Xi(\bar{\Xi})$ Decay Vertex	0.9992, 0.9993, 0.9994
Min. DCA Bachelor π	0.5, 1, 2 mm
Min. DCA $\Lambda(\bar{\Lambda})$	1, 2, 3 mm
Max. DCA $\Lambda(\bar{\Lambda})$ Daughters	3, 4, 5 mm
Min. DCA to Primary Vertex of $p(\bar{p})$ Daughter of $\Lambda(\bar{\Lambda})$	0.5, 1, 2 mm
Min. DCA to Primary Vertex of $\pi^-(\pi^+)$ Daughter of $\Lambda(\bar{\Lambda})$	2, 3, 4 mm
Min. Average Separation of $\Lambda(\bar{\Lambda})$ Daughter and K^\pm with like charge	7, 8, 9 cm
Min. Average Separation of Bachelor π and K^\pm with like charge	7, 8, 9 cm
Max. DCA to Primary Vertex in Transverse Plane of K^\pm	1.92, 2.4, 2.88
Max. DCA to Primary Vertex in Longitudinal Direction of K^\pm	2.4, 3.0, 3.6

Table 4: $\Xi^- K^\pm$ systematics

767 **7 Results and Discussion**

768 **7.1 Results: ΛK_S^0 and ΛK^\pm**

769 In the following sections, we present results assuming (i) no residual correlations (Sec. 7.1.1), (ii) three
 770 residual contributors (Sec. 7.1.2), and (iii) ten residual contributors (Sec. 7.1.3). We find the case of
 771 three and ten contributors to be consistent; therefore, for simplicity, we will quote the result utilizing
 772 three residuals as our final result.

773 For the results shown, unless otherwise noted, the following hold true: All correlation functions were
 774 normalized in the range $0.32 < k^* < 0.40$ GeV/c, and fit in the range $0.0 < k^* < 0.30$ GeV/c. For the
 775 ΛK^- and $\bar{\Lambda} K^+$ analyses, the region $0.19 < k^* < 0.23$ GeV/c was excluded from the fit to exclude the
 776 bump caused by the Ω^- resonance. The non-femtoscopic background was modeled by a (6th-)order
 777 polynomial fit to THERMINATOR simulation. The $\Lambda K^+(\bar{\Lambda} K^-)$ radii are shared with $\Lambda K^-(\bar{\Lambda} K^+)$, while
 778 the $\Lambda K_S^0(\bar{\Lambda} K_S^0)$ radii are unique. In the figures showing experimental correlation functions with fits, the
 779 black solid line represents the primary (ΛK) correlation's contribution to the fit. The green line shows
 780 the fit to the non-flat background. The purple points show the fit after all residuals' contributions have
 781 been included, and momentum resolution and non-flat background corrections have been applied.

782 Before beginning, I first collect a summary of my final results in Figure 29. In the summary plot, we
 783 show the extracted scattering parameters in the form of a $\text{Im}[f_0]$ vs $\text{Re}[f_0]$ plot, which includes the d_0
 784 values to the right side. We also show the λ vs. radius parameters for all three of our studied centrality
 785 bins. In Fig. 29, three residual contributors were used, and the background was modeled by a (6th-
 786)order polynomial fit to THERMINATOR simulation. For the ΛK_S^0 results shown in the figure, the ΛK_S^0
 787 and $\bar{\Lambda} K_S^0$ analyses were fit simultaneously across all centralities (0-10%, 10-30%, 30-50%); scattering
 788 parameters and a single λ parameter were shared amongst all, the radii were shared amongst results
 789 of like-centrality, and each has a unique normalization parameter. For the ΛK^\pm results shown, all four
 790 pair combinations were fit simultaneously ($\Lambda K^+, \bar{\Lambda} K^-, \Lambda K^-, \bar{\Lambda} K^+$) across all centralities. Scattering
 791 parameters were shared between pair-conjugate systems (i.e. a parameter set describing ΛK^+ & $\bar{\Lambda} K^-$,
 792 and a separate set describing ΛK^- & $\bar{\Lambda} K^+$). For each centrality, a radius and λ parameters were shared
 793 between all pairs. Each analysis has a unique normalization parameter.

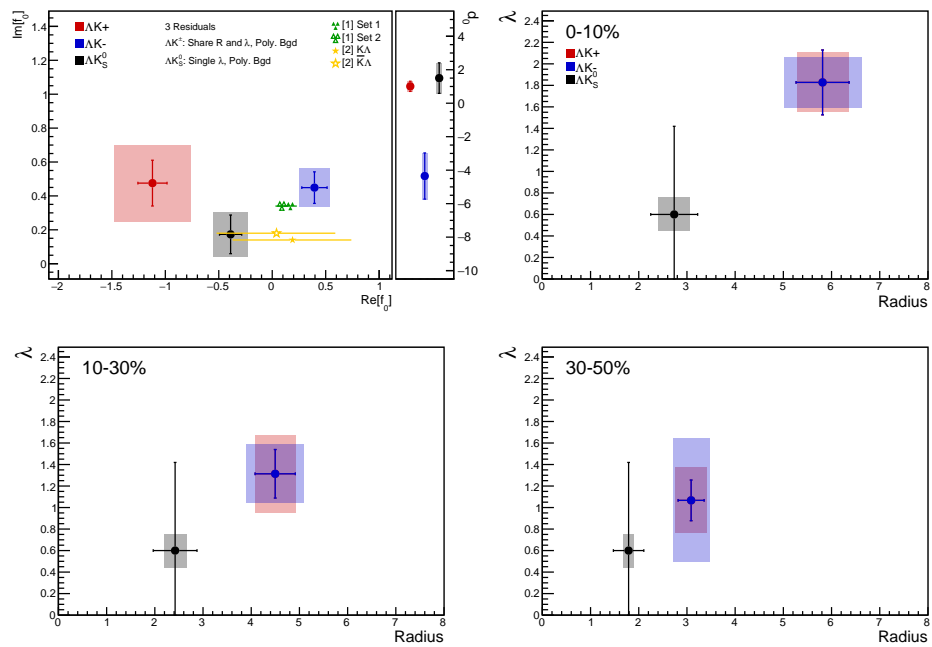


Fig. 29: Extracted scattering parameters for the case of 3 residual contributors for all of our ΛK systems. [Top Left]: $\text{Im}[f_0]$ vs. $\text{Re}[f_0]$, together with d_0 to the right. [Top Right (Bottom Left, Bottom Right)]: λ vs. Radius for the 0-10% (10-30%, 30-50%) bin. The green [9] and yellow [10] points show theoretical predictions made using chiral perturbation theory.

794 **7.1.1 Results: ΛK_S^0 and ΛK^\pm : No Residual Correlations Included in Fit**

795 Figure 30 nicely collects and summarizes all of our extracted fit parameters for the case of no included
 796 residual contributors. Figure 31 presents our extracted fit radii, along with those of other systems pre-
 797 viously analyzed by ALICE [11], as a function of pair transverse mass (m_T). Figures 32, 33, and 34
 798 show the experimental correlation functions with fits, assuming no residual contributors, for all studied
 799 centralities for ΛK_S^0 with $\bar{\Lambda} K_S^0$, ΛK^+ with $\bar{\Lambda} K^-$, and ΛK^- with $\bar{\Lambda} K^+$, respectively. The parameter sets
 800 extracted from the fits can be found in Tables 7 and 8.

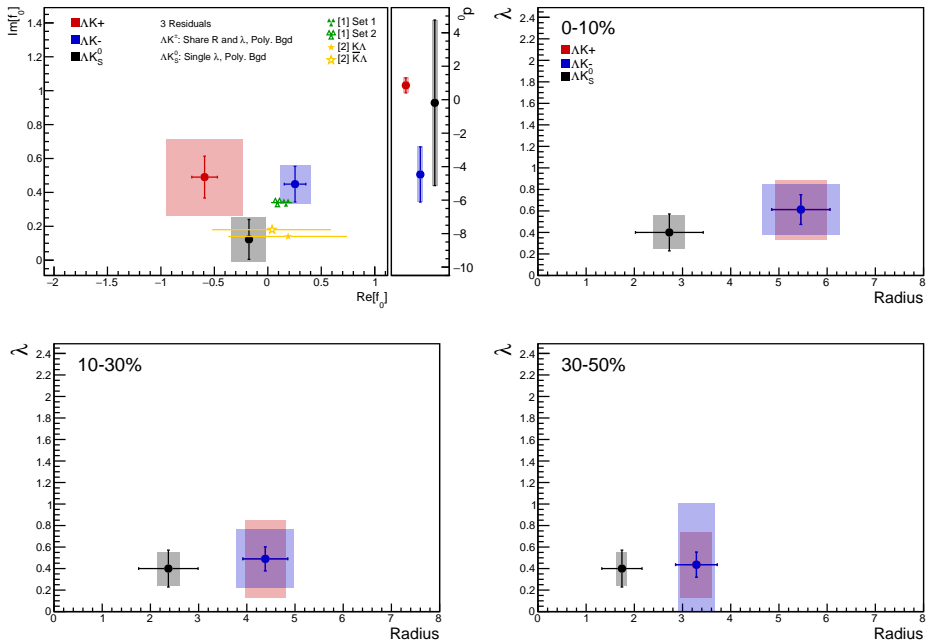


Fig. 30: Extracted scattering parameters for the case of NO residual contributors for all of our ΛK systems. [Top Left]: $\Im f_0$ vs. $\Re f_0$, together with d_0 to the right. [Top Right (Bottom Left, Bottom Right)]: λ vs. Radius for the 0-10% (10-30%, 30-50%) bin. The green [9] and yellow [10] points show theoretical predictions made using chiral perturbation theory.

801 Figure 31 shows extracted R_{inv} parameters as a function of transverse mass (m_T) for various pair systems
 802 over several centralities. The published ALICE data [11] is shown with transparent, open symbols. The
 803 new ΛK results are shown with opaque, filled symbols. The radii shown an increasing size with increas-
 804 ing centrality, as is expected from the simple geometric picture of the collisions. The radii decrease
 805 in size with increasing m_T , and we see an approximate scaling of the radii with transverse mass, as is
 806 expected in the presence of collective flow in the system.

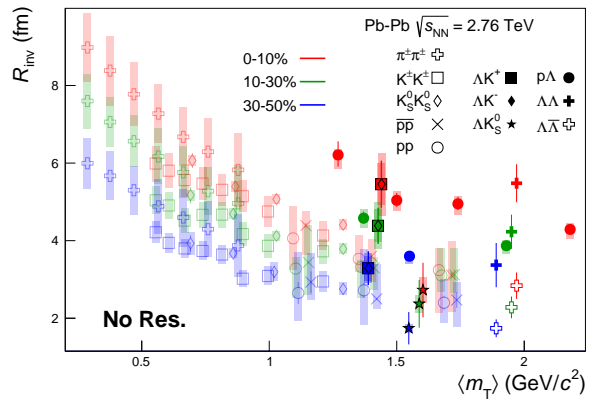
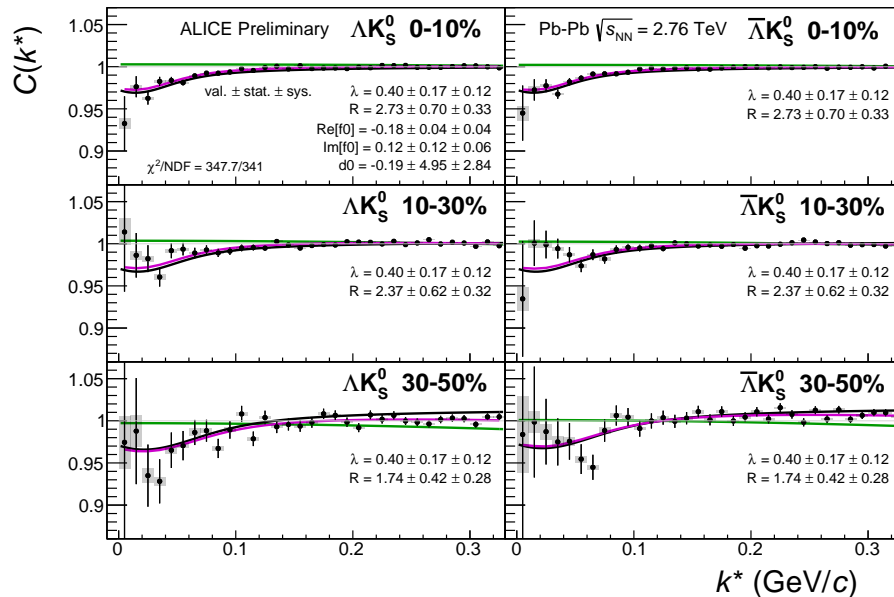
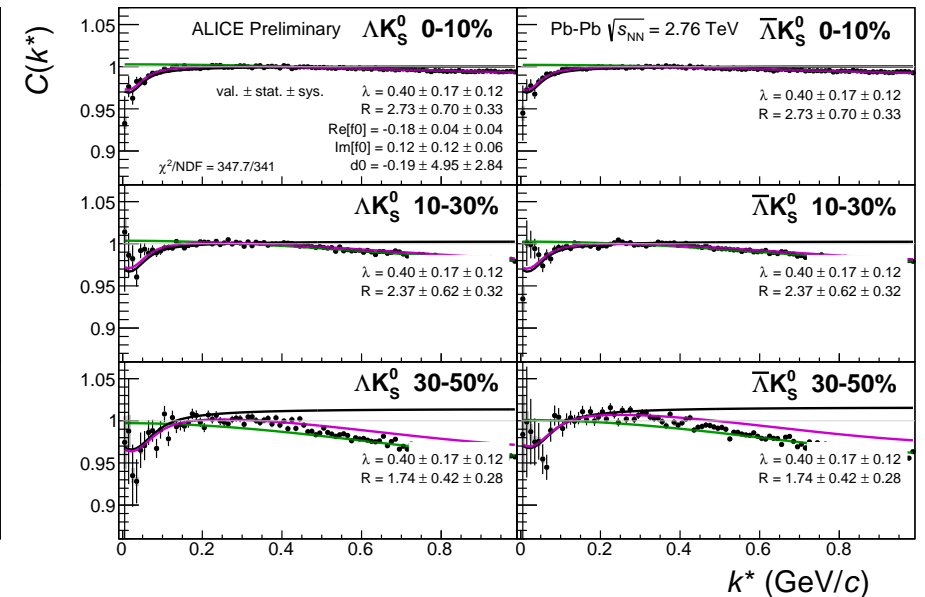


Fig. 31: No residual correlations in ΛK fits. Extracted fit R_{inv} parameters as a function of pair transverse mass (m_T) for various pair systems over several centralities. The ALICE published data [11] is shown with transparent, open symbols. The new ΛK results are shown with opaque, filled symbols. In the left, the ΛK^+ (with its conjugate pair) results are shown separately from the ΛK^- (with its conjugate pair) results. In the right, all ΛK^\pm results are averaged.

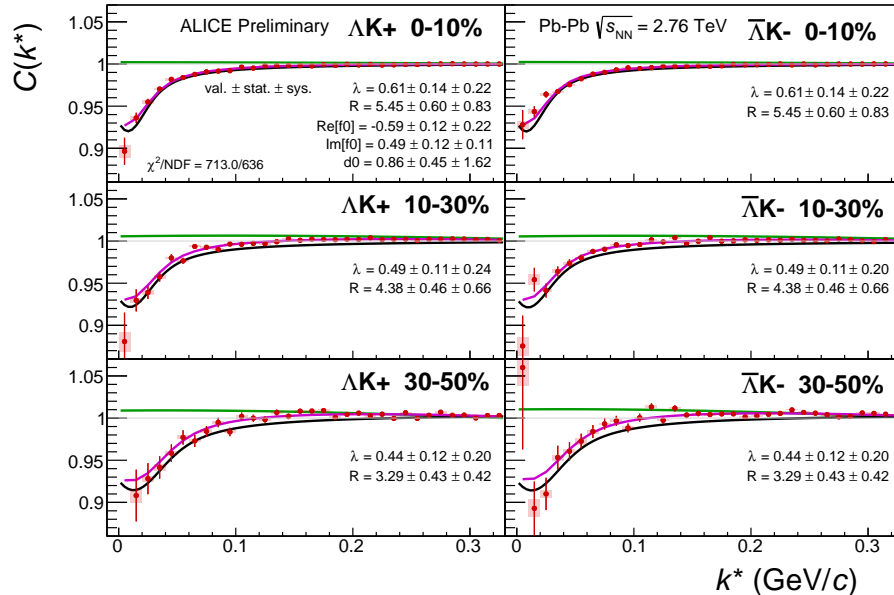


(a) Signal region view ($k^* \lesssim 0.3$ GeV/c)

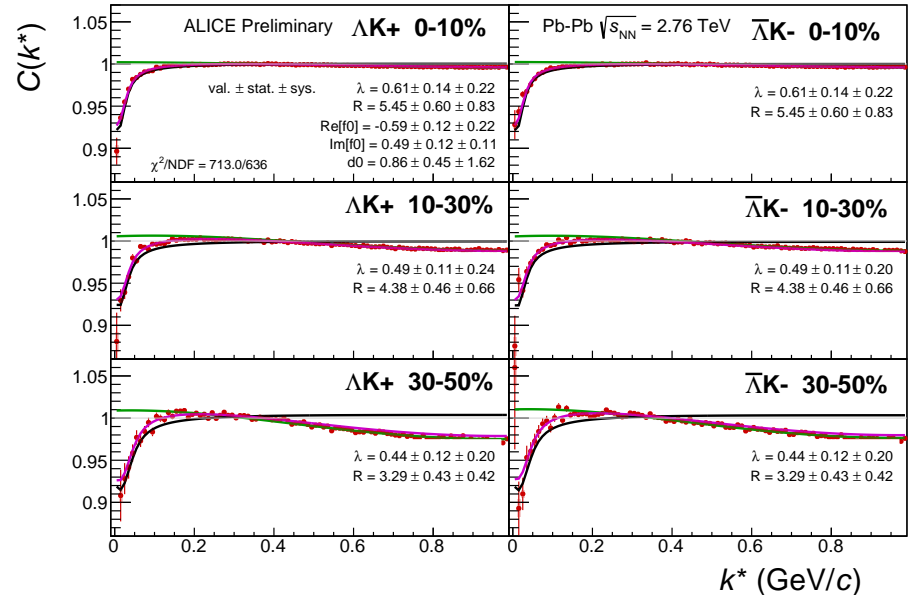


(b) Wide view ($k^* \lesssim 1.0$ GeV/c)

Fig. 32: Fits, with NO residual correlations included, to the ΛK_S^0 (left) and $\bar{\Lambda} K_S^0$ (right) data for the centralities 0-10% (top), 10-30% (middle), and 30-50% (bottom). The lines represent the statistical errors, while the boxes represent the systematic errors. A single λ parameter is shared amongst all. Each analysis has a unique normalization parameter. The radii are shared between analyses of like centrality, as these should have similar source sizes. The scattering parameters ($\mathbb{R}f_0$, $\mathbb{I}f_0$, d_0) are shared amongst all. The background is modeled by a (6th-)degree polynomial fit to THERMINATOR simulation. The black solid line represents the “raw” primary fit, i.e. not corrected for momentum resolution effects nor non-flat background. The green line shows the fit to the non-flat background. The purple points show the fit after momentum resolution and non-flat background corrections have been applied. The extracted fit values with uncertainties are printed.

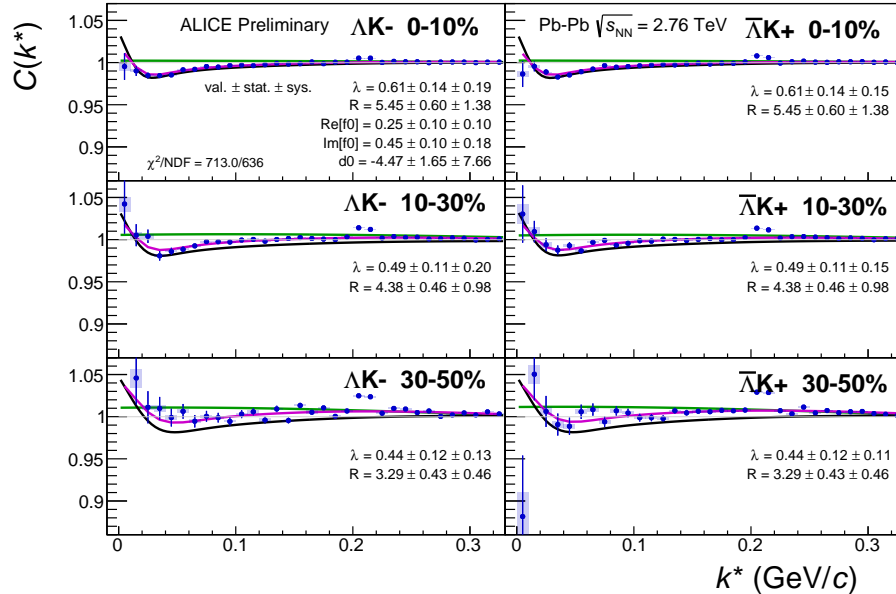


(a) Signal region view ($k^* \lesssim 0.3 \text{ GeV}/c$)

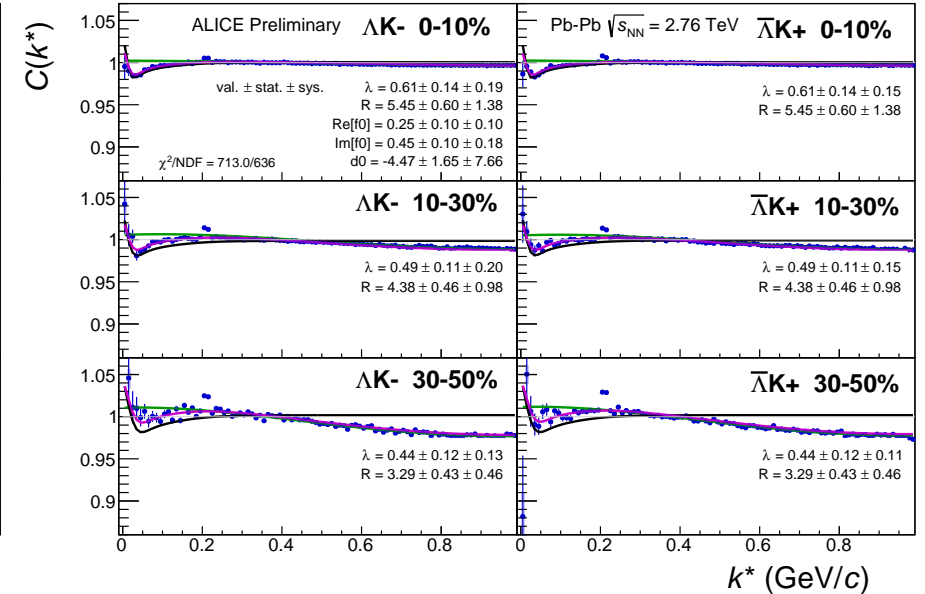


(b) Wide view ($k^* \lesssim 1.0 \text{ GeV}/c$)

Fig. 33: Fits to the ΔK^+ (left) and $\bar{\Delta}K^-$ (right) data for the centralities 0-10% (top), 10-30% (middle), and 30-50% (bottom). The lines represent the statistical errors, while the boxes represent the systematic errors. All ΔK^\pm analyses are fit simultaneously across all centralities (0-10%, 10-30%, 30-50%). Scattering parameters ($\mathbb{R}f_0$, $\mathbb{I}f_0$, d_0) are shared between pair-conjugate systems (i.e. a parameter set describing the ΔK^+ & $\bar{\Delta}K^-$ system, and a separate set describing the ΔK^- & $\bar{\Delta}K^+$ system). For each centrality, a radius and λ parameters are shared between all pairs (ΔK^+ , $\bar{\Delta}K^-$, ΔK^- , $\bar{\Delta}K^+$). Each analysis has a unique normalization parameter. The background is modeled by a (6th-)degree polynomial fit to THERMINATOR simulation. The black solid line represents the “raw” primary fit, i.e. not corrected for momentum resolution effects nor non-flat background. The green line shows the fit to the non-flat background. The purple points show the fit after momentum resolution and non-flat background corrections have been applied. The extracted fit values with uncertainties are printed.



(a) Signal region view ($k^* \lesssim 0.3$ GeV/c)



(b) Wide view ($k^* \lesssim 1.0$ GeV/c)

Fig. 34: Fits, with NO residual correlations included, to the ΛK^- (left) with $\bar{\Lambda} K^+$ (right) data for the centralities 0-10% (top), 10-30% (middle), and 30-50% (bottom). The lines represent the statistical errors, while the boxes represent the systematic errors. All ΛK^\pm analyses are fit simultaneously across all centralities (0-10%, 10-30%, 30-50%). Scattering parameters ($\mathbb{R}f_0$, $\mathbb{I}f_0$, d_0) are shared between pair-conjugate systems (i.e. a parameter set describing the ΛK^+ & $\bar{\Lambda} K^-$ system, and a separate set describing the ΛK^- & $\bar{\Lambda} K^+$ system). For each centrality, a radius and λ parameters are shared between all pairs (ΛK^+ , $\bar{\Lambda} K^-$, ΛK^- , $\bar{\Lambda} K^+$). Each analysis has a unique normalization parameter. The background is modeled by a (6th-degree polynomial fit to THERMINATOR simulation. The black solid line represents the “raw” primary fit, i.e. not corrected for momentum resolution effects nor non-flat background. The green line shows the fit to the non-flat background. The purple points show the fit after momentum resolution and non-flat background corrections have been applied. The extracted fit values with uncertainties are printed.

Fit Results $\Lambda(\bar{\Lambda})K_S^0$						
System	Centrality	Fit Parameters				
		λ	R	$\mathbb{R}f_0$	$\mathbb{I}f_0$	d_0
$\Lambda K_S^0 \& \bar{\Lambda} K_S^0$	0-10%			2.73 ± 0.70 (stat.) ± 0.33 (sys.)		
	10-30%	0.40 ± 0.17 (stat.) ± 0.16 (sys.)	2.37 ± 0.62 (stat.) ± 0.23 (sys.)	-0.18 ± 0.04 (stat.) ± 0.16 (sys.)	0.12 ± 0.12 (stat.) ± 0.13 (sys.)	-0.19 ± 4.95 (stat.) ± 0.62 (sys.)
	30-50%			1.74 ± 0.42 (stat.) ± 0.11 (sys.)		

Table 5: Fit Results $\Lambda(\bar{\Lambda})K_S^0$, with no residual correlations included. Each pair is fit simultaneously with its conjugate (ie. ΛK_S^0 with $\bar{\Lambda} K_S^0$) across all centralities (0-10%, 10-30%, 30-50%), for a total of 6 simultaneous analyses in the fit. A single λ parameter is shared amongst all. Each analysis has a unique normalization parameter. The radii are shared between analyses of like centrality, as these should have similar source sizes. The scattering parameters ($\mathbb{R}f_0$, $\mathbb{I}f_0$, d_0) are shared amongst all. The background is modeled by a (6th-)degree polynomial fit to THERMINATOR simulation. The fit is done on the data with only statistical error bars. The errors marked as “stat.” are those returned by MINUIT. The errors marked as “sys.” are those which result from my systematic analysis (as outlined in Section 6).

Fit Results $\Lambda(\bar{\Lambda})K^\pm$						
System	Centrality	Fit Parameters				
		λ	R	$\mathbb{R}f_0$	$\mathbb{I}f_0$	d_0
$\Lambda K^+ \& \bar{\Lambda} K^-$	0-10%	0.61 ± 0.14 (stat.) ± 0.28 (sys.)	5.45 ± 0.60 (stat.) ± 0.54 (sys.)	-0.59 ± 0.12 (stat.) ± 0.36 (sys.)	0.49 ± 0.12 (stat.) ± 0.23 (sys.)	0.86 ± 0.45 (stat.) ± 0.53 (sys.)
	10-30%	0.49 ± 0.11 (stat.) ± 0.36 (sys.)	4.38 ± 0.46 (stat.) ± 0.42 (sys.)			
$\Lambda K^+ \& \bar{\Lambda} K^-$	30-50%	0.44 ± 0.12 (stat.) ± 0.31 (sys.)	3.29 ± 0.43 (stat.) ± 0.32 (sys.)	0.25 ± 0.10 (stat.) ± 0.14 (sys.)	0.45 ± 0.10 (stat.) ± 0.11 (sys.)	-4.47 ± 1.65 (stat.) ± 1.33 (sys.)

Table 6: Fit Results $\Lambda(\bar{\Lambda})K^\pm$, with no residual correlations included. All ΛK^\pm analyses are fit simultaneously across all centralities (0-10%, 10-30%, 30-50%). Scattering parameters ($\mathbb{R}f_0$, $\mathbb{I}f_0$, d_0) are shared between pair-conjugate systems (i.e. a parameter set describing the $\Lambda K^+ \& \bar{\Lambda} K^-$ system, and a separate set describing the $\Lambda K^- \& \bar{\Lambda} K^+$ system). For each centrality, a radius and λ parameters are shared between all pairs ($\Lambda K^+, \bar{\Lambda} K^-, \Lambda K^-, \bar{\Lambda} K^+$). Each analysis has a unique normalization parameter. The background is modeled by a (6th-)degree polynomial fit to THERMINATOR simulation. The fit is done on the data with only statistical error bars. The errors marked as “stat.” are those returned by MINUIT. The errors marked as “sys.” are those which result from my systematic analysis (as outlined in Section 6).

807 7.1.2 Results: ΛK_S^0 and ΛK^\pm : 3 Residual Correlations Included in Fit

808 Figure 35 nicely collects and summarizes all of our extracted fit parameters for the case of 3 included
 809 residual contributors. Figure 36 presents our extracted fit radii, along with those of other systems pre-
 810 viously analyzed by ALICE [11], as a function of pair transverse mass (m_T). Figures 37, 38, and 39
 811 show the experimental correlation functions with fits, assuming 3 residual contributors, for all studied
 812 centralities for ΛK_S^0 with $\bar{\Lambda} K_S^0$, ΛK^+ with $\bar{\Lambda} K^-$, and ΛK^- with $\bar{\Lambda} K^+$, respectively. The parameter sets
 813 extracted from the fits can be found in Tables 7 and 8.

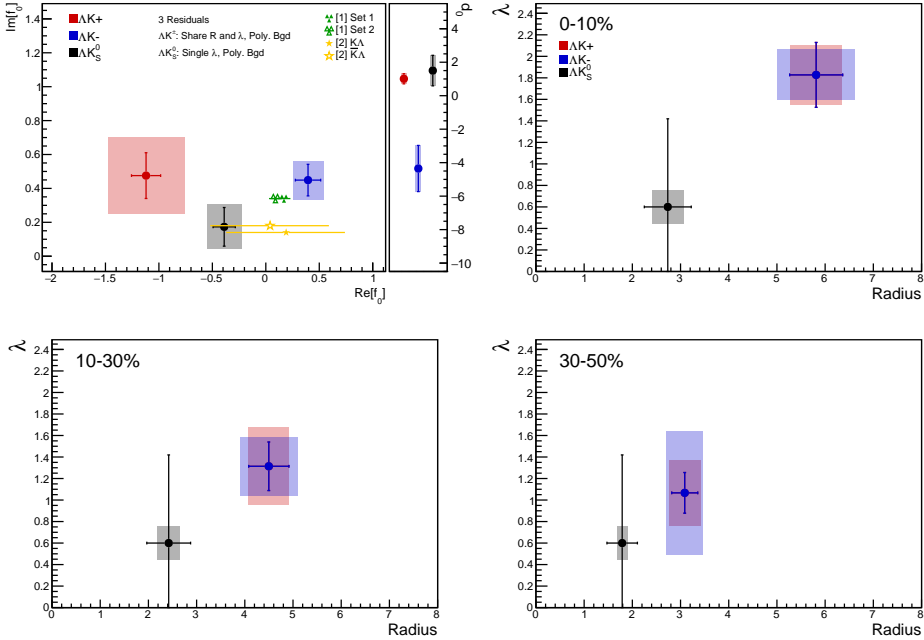


Fig. 35: Extracted scattering parameters for the case of 3 residual contributors for all of our AK systems. [Top Left]: $\text{Im}[f_0]$ vs. $\text{Re}[f_0]$, together with d_0 to the right. [Top Right (Bottom Left, Bottom Right)]: λ vs. Radius for the 0-10% (10-30%, 30-50%) bin. The green [9] and yellow [10] points show theoretical predictions made using chiral perturbation theory.

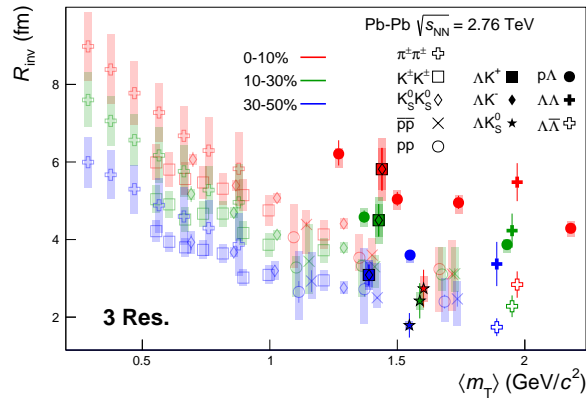
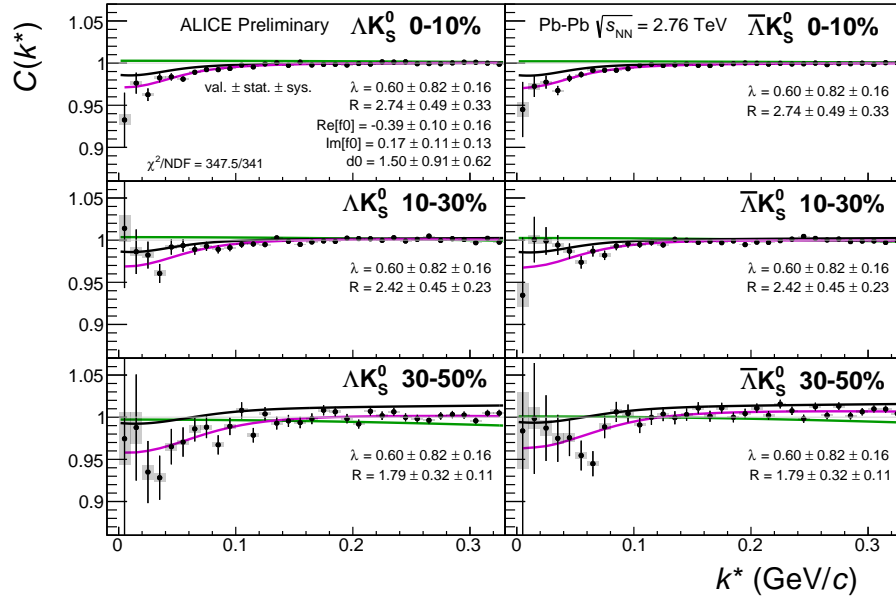
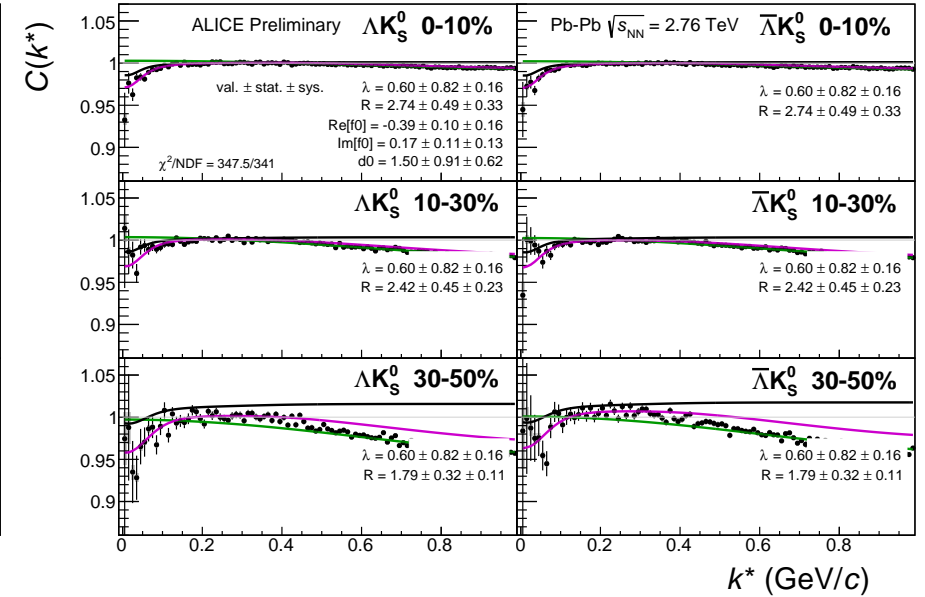


Fig. 36: 3 residual correlations in AK fits. Extracted fit R_{inv} parameters as a function of pair transverse mass (m_T) for various pair systems over several centralities. The ALICE published data [11] is shown with transparent, open symbols. The new AK results are shown with opaque, filled symbols. In the left, the ΛK^+ (with it's conjugate pair) results are shown separately from the ΛK^- (with it's conjugate pair) results. In the right, all ΛK^\pm results are averaged.

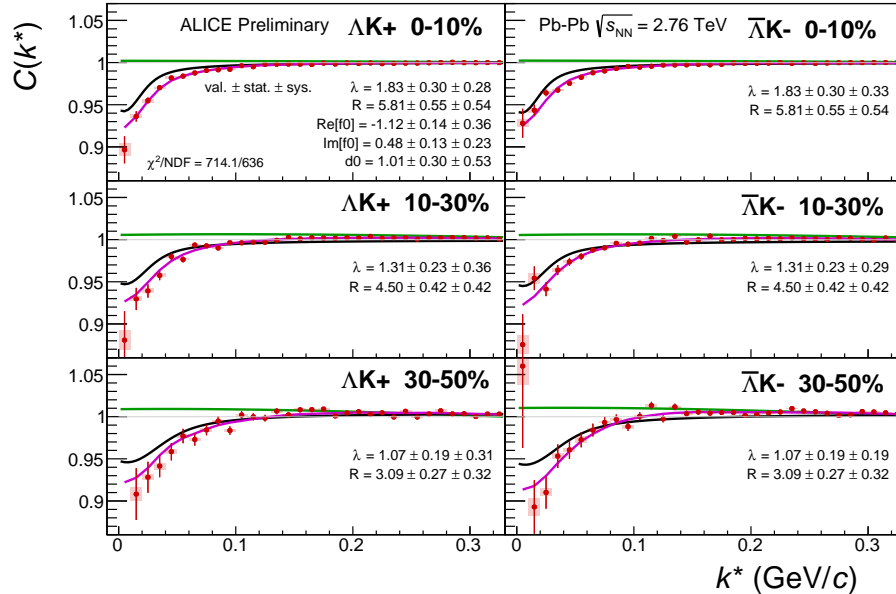


(a) Signal region view ($k^* \lesssim 0.3$ GeV/c)

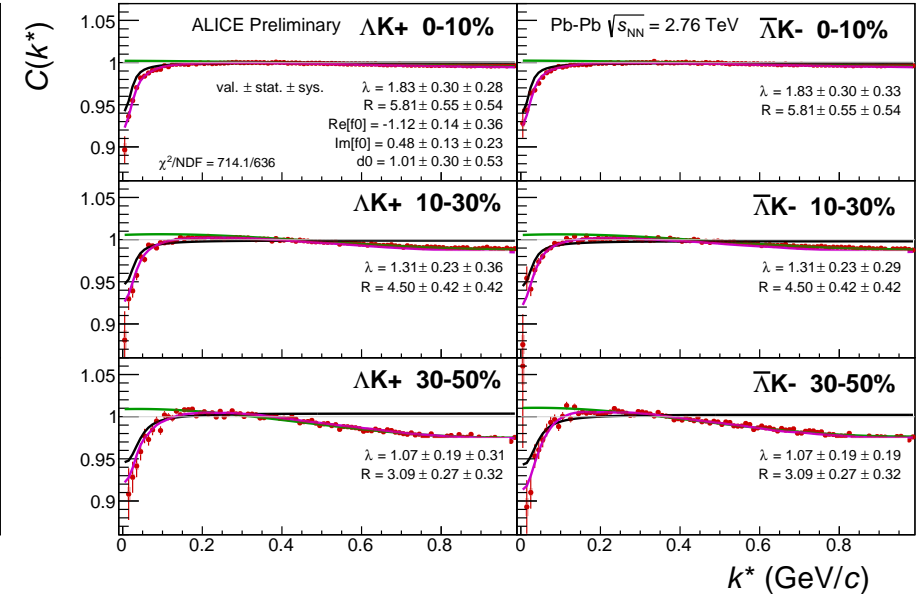


(b) Wide view ($k^* \lesssim 1.0$ GeV/c)

Fig. 37: Fits, with 3 residual correlations included, to the ΛK_s^0 (left) and $\bar{\Lambda} K_s^0$ (right) data for the centralities 0-10% (top), 10-30% (middle), and 30-50% (bottom). The lines represent the statistical errors, while the boxes represent the systematic errors. A single λ parameter is shared amongst all. Each analysis has a unique normalization parameter. The radii are shared between analyses of like centrality, as these should have similar source sizes. The scattering parameters ($\mathbb{R} f_0, \mathbb{I} f_0, d_0$) are shared amongst all. The background is modeled by a (6th-degree polynomial fit to THERMINATOR simulation. The black solid line represents the primary (ΛK) correlation's contribution to the fit. The green line shows the fit to the non-flat background. The purple points show the fit after all residuals' contributions have been included, and momentum resolution and non-flat background corrections have been applied. The extracted fit values with uncertainties are printed.

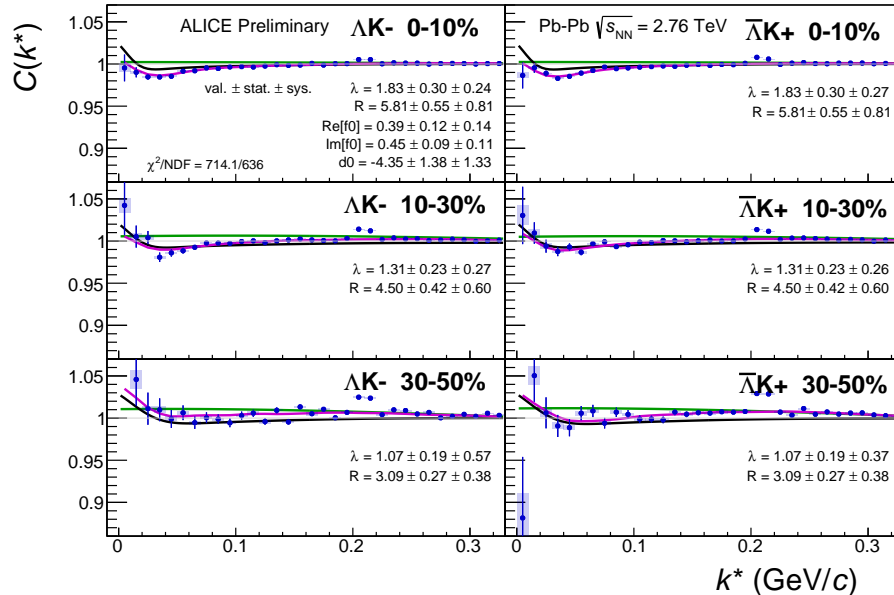


(a) Signal region view ($k^* \lesssim 0.3 \text{ GeV}/c$)

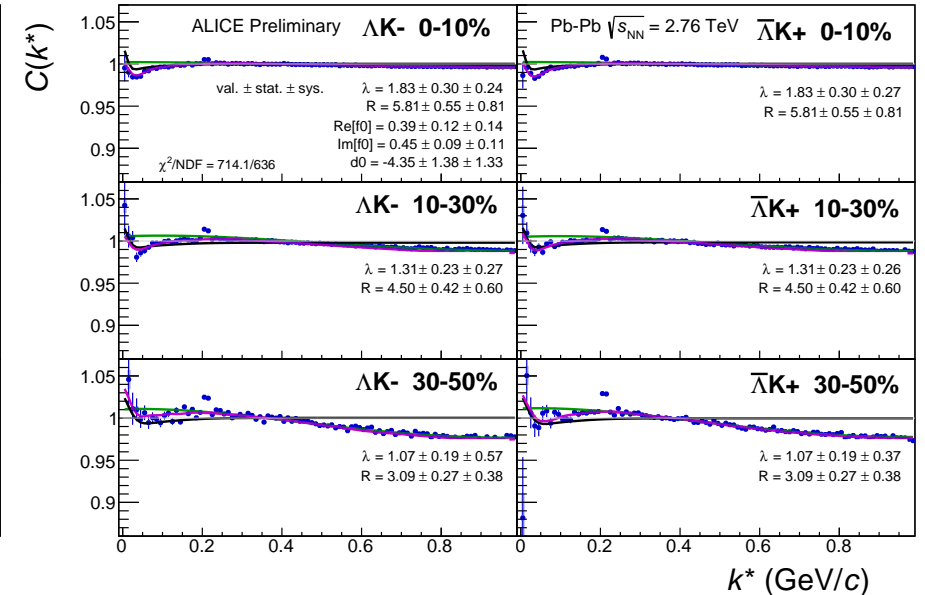


(b) Wide view ($k^* \lesssim 1.0 \text{ GeV}/c$)

Fig. 38: Fits, with 3 residual correlations included, to the ΔK^+ (left) and $\bar{\Delta} K^-$ (right) data for the centralities 0-10% (top), 10-30% (middle), and 30-50% (bottom). The lines represent the statistical errors, while the boxes represent the systematic errors. All ΔK^\pm analyses are fit simultaneously across all centralities (0-10%, 10-30%, 30-50%). Scattering parameters ($\text{Re}[f_0]$, $\text{Im}[f_0]$, d_0) are shared between pair-conjugate systems (i.e. a parameter set describing the ΔK^+ & $\bar{\Delta} K^-$ system, and a separate set describing the ΔK^- & $\bar{\Delta} K^+$ system). For each centrality, a radius and λ parameters are shared between all pairs (ΔK^+ , $\bar{\Delta} K^-$, ΔK^- , $\bar{\Delta} K^+$). Each analysis has a unique normalization parameter. The background is modeled by a (6th-degree polynomial fit to THERMINATOR simulation. The black solid line represents the primary (ΔK) correlation's contribution to the fit. The green line shows the fit to the non-flat background. The purple points show the fit after all residuals' contributions have been included, and momentum resolution and non-flat background corrections have been applied. The extracted fit values with uncertainties are printed.



(a) Signal region view ($k^* \lesssim 0.3 \text{ GeV}/c$)



(b) Wide view ($k^* \lesssim 1.0 \text{ GeV}/c$)

Fig. 39: Fits, with 3 residual correlations included, to the ΛK^- (left) with $\bar{\Lambda} K^+$ (right) data for the centralities 0-10% (top), 10-30% (middle), and 30-50% (bottom). The lines represent the statistical errors, while the boxes represent the systematic errors. All ΛK^\pm analyses are fit simultaneously across all centralities (0-10%, 10-30%, 30-50%). Scattering parameters ($\mathbb{R}f_0$, $\mathbb{I}f_0$, d_0) are shared between pair-conjugate systems (i.e. a parameter set describing the ΛK^+ & $\bar{\Lambda} K^-$ system, and a separate set describing the ΛK^- & $\bar{\Lambda} K^+$ system). For each centrality, a radius and λ parameters are shared between all pairs (ΛK^+ , $\bar{\Lambda} K^-$, ΛK^- , $\bar{\Lambda} K^+$). Each analysis has a unique normalization parameter. The background is modeled by a (6th-)degree polynomial fit to THERMINATOR simulation. The black solid line represents the “raw” fit, i.e. not corrected for momentum resolution effects nor non-flat background. The green line shows the fit to the non-flat background. The purple points show the fit after momentum resolution and non-flat background corrections have been applied. The extracted fit values with uncertainties are printed.

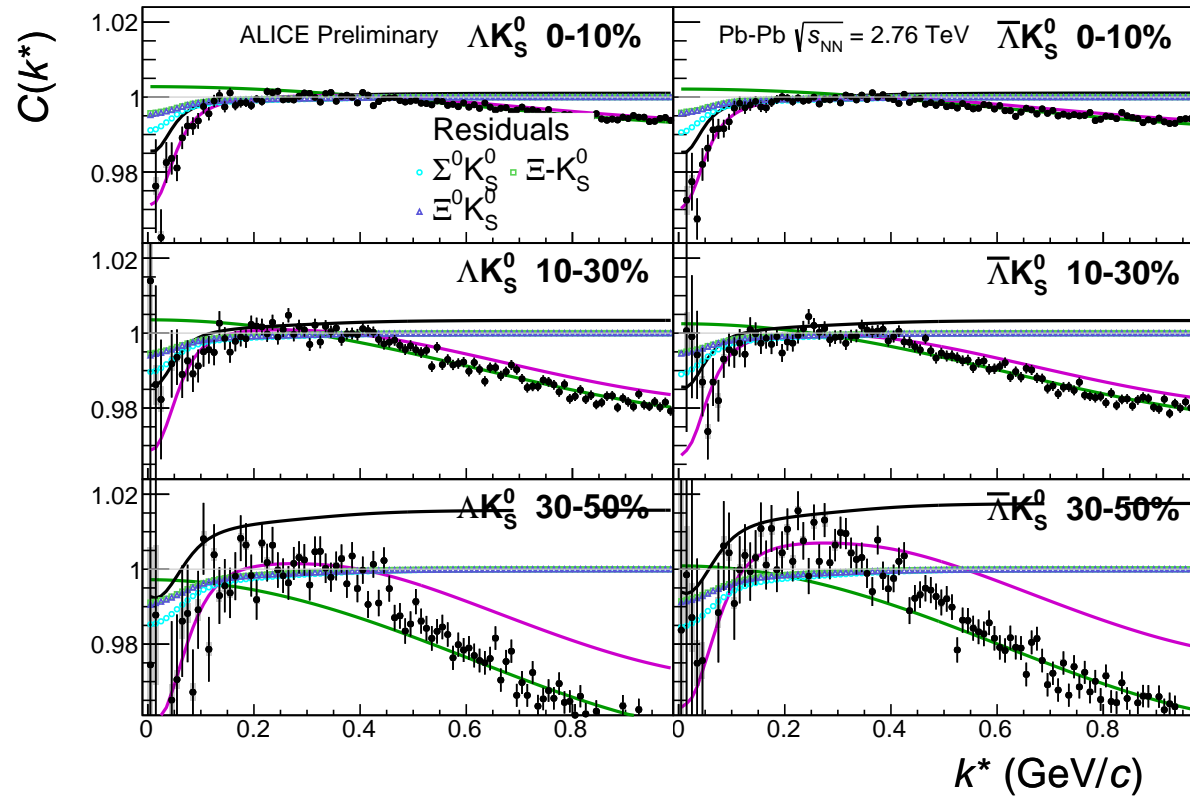
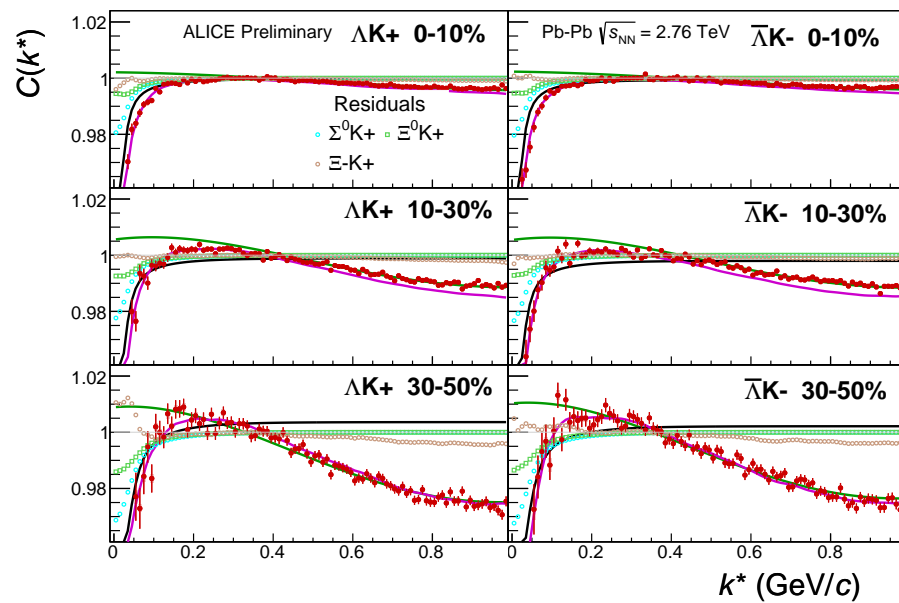
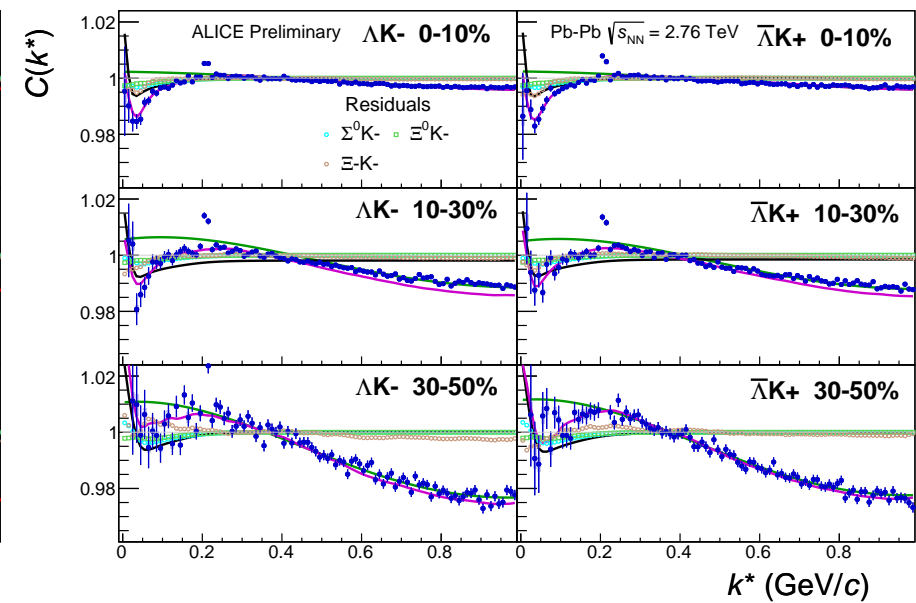


Fig. 40: Fits, with 3 residual correlations included and shown, to the ΛK_S^0 (left) and $\bar{\Lambda} K_S^0$ (right) data for the centralities 0-10% (top), 10-30% (middle), and 30-50% (bottom). The three parent pairs used for the residual correction to the ΛK_S^0 ($\bar{\Lambda} K_S^0$) fit are $\Sigma^0 K_S^0$, $\Xi^0 K_S^0$, and $\Xi^- K_S^0$ ($\bar{\Sigma}^0 K_S^0$, $\bar{\Xi}^0 K_S^0$, and $\bar{\Xi}^+ K_S^0$).



(a) $\Lambda K^+(\bar{\Lambda} K^-)$ fits with residual contributions shown for the centralities 0-10% (top), 10-30% (middle), and 30-50% (bottom)



(b) $\Lambda K^-(\bar{\Lambda} K^+)$ fits with residual contributions shown for the centralities 0-10% (top), 10-30% (middle), and 30-50% (bottom)

Fig. 41: Fits, with 3 residual correlations included and shown, to the ΛK^+ & $\bar{\Lambda} K^-$ (left) and ΛK^- & $\bar{\Lambda} K^+$ (right) data for the centralities 0-10% (top), 10-30% (middle), and 30-50% (bottom). The three parent pairs used for the residual correction to the $\Lambda K^+(\bar{\Lambda} K^-)$ fit are $\Sigma^0 K^+$, $\Xi^0 K^+$, and $\Xi^- K^+$ ($\bar{\Sigma}^0 K^-$, $\bar{\Xi}^0 K^-$, and $\bar{\Xi}^+ K^-$).

Fit Results $\Lambda(\bar{\Lambda})K_S^0$						
System	Centrality	Fit Parameters				
		λ	R	$\mathbb{R}f_0$	$\mathbb{I}f_0$	d_0
$\Lambda K_S^0 \& \bar{\Lambda} K_S^0$	0-10%			2.74 ± 0.49 (stat.) ± 0.33 (sys.)		
	10-30%	0.60 ± 0.82 (stat.) ± 0.16 (sys.)	2.42 ± 0.45 (stat.) ± 0.23 (sys.)	-0.39 ± 0.10 (stat.) ± 0.16 (sys.)	0.17 ± 0.11 (stat.) ± 0.13 (sys.)	1.50 ± 0.91 (stat.) ± 0.62 (sys.)
	30-50%			1.79 ± 0.32 (stat.) ± 0.11 (sys.)		

Table 7: Fit Results $\Lambda(\bar{\Lambda})K_S^0$, with 3 residual correlations included. Each pair is fit simultaneously with its conjugate (ie. ΛK_S^0 with $\bar{\Lambda} K_S^0$) across all centralities (0-10%, 10-30%, 30-50%), for a total of 6 simultaneous analyses in the fit. A single λ parameter is shared amongst all. Each analysis has a unique normalization parameter. The radii are shared between analyses of like centrality, as these should have similar source sizes. The scattering parameters ($\mathbb{R}f_0$, $\mathbb{I}f_0$, d_0) are shared amongst all. The background is modeled by a (6th-)degree polynomial fit to THERMINATOR simulation. The fit is done on the data with only statistical error bars. The errors marked as “stat.” are those returned by MINUIT. The errors marked as “sys.” are those which result from my systematic analysis (as outlined in Section 6).

Fit Results $\Lambda(\bar{\Lambda})K^\pm$						
System	Centrality	Fit Parameters				
		λ	R	$\mathbb{R}f_0$	$\mathbb{I}f_0$	d_0
$\Lambda K^+ \& \bar{\Lambda} K^-$	0-10%	1.83 ± 0.30 (stat.) ± 0.28 (sys.)	5.81 ± 0.55 (stat.) ± 0.54 (sys.)			
	10-30%	1.31 ± 0.23 (stat.) ± 0.36 (sys.)	4.50 ± 0.42 (stat.) ± 0.42 (sys.)	-1.12 ± 0.14 (stat.) ± 0.36 (sys.)	0.48 ± 0.13 (stat.) ± 0.23 (sys.)	1.01 ± 0.30 (stat.) ± 0.53 (sys.)
$\Lambda K^+ \& \bar{\Lambda} K^+$	30-50%	1.07 ± 0.19 (stat.) ± 0.31 (sys.)	3.09 ± 0.27 (stat.) ± 0.32 (sys.)	0.39 ± 0.12 (stat.) ± 0.14 (sys.)	0.45 ± 0.09 (stat.) ± 0.11 (sys.)	-4.35 ± 1.38 (stat.) ± 1.33 (sys.)

Table 8: Fit Results $\Lambda(\bar{\Lambda})K^\pm$, with 3 residual correlations included. All ΛK^\pm analyses are fit simultaneously across all centralities (0-10%, 10-30%, 30-50%). Scattering parameters ($\mathbb{R}f_0$, $\mathbb{I}f_0$, d_0) are shared between pair-conjugate systems (i.e. a parameter set describing the $\Lambda K^+ \& \bar{\Lambda} K^-$ system, and a separate set describing the $\Lambda K^- \& \bar{\Lambda} K^+$ system). For each centrality, a radius and λ parameters are shared between all pairs ($\Lambda K^+, \bar{\Lambda} K^-, \Lambda K^-, \bar{\Lambda} K^+$). Each analysis has a unique normalization parameter. The background is modeled by a (6th-)degree polynomial fit to THERMINATOR simulation. The fit is done on the data with only statistical error bars. The errors marked as “stat.” are those returned by MINUIT. The errors marked as “sys.” are those which result from my systematic analysis (as outlined in Section 6).

814 **7.1.3 Results: ΛK_S^0 and ΛK^\pm : 10 Residual Correlations Included in Fit**

815 Figure 42 nicely collects and summarizes all of our extracted fit parameters for the case of 10 included
 816 residual contributors. Figure 43 presents our extracted fit radii, along with those of other systems pre-
 817 viously analyzed by ALICE [11], as a function of pair transverse mass (m_T). Figures 44, 45, and 46
 818 show the experimental correlation functions with fits, assuming 10 residual contributors, for all studied
 819 centralities for ΛK_S^0 with $\bar{\Lambda} K_S^0$, ΛK^+ with $\bar{\Lambda} K^-$, and ΛK^- with $\bar{\Lambda} K^+$, respectively. The parameter sets
 820 extracted from the fits can be found in Tables 9 and 10.

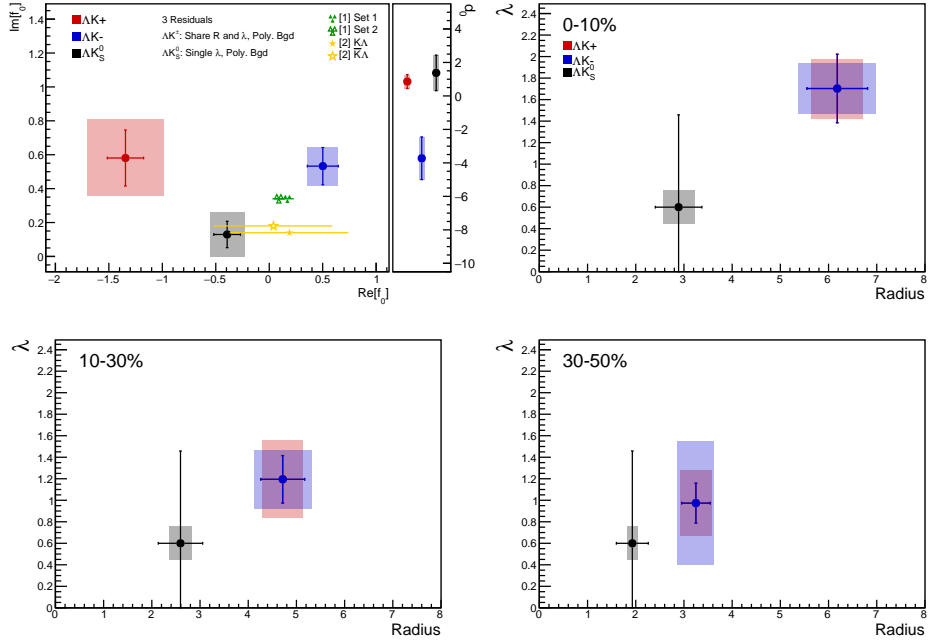


Fig. 42: Extracted scattering parameters for the case of 10 residual contributors for all of our ΛK systems. [Top Left]: $\text{Im } f_0$ vs. $\text{Re } f_0$, together with d_0 to the right. [Top Right (Bottom Left, Bottom Right)]: λ vs. Radius for the 0-10% (10-30%, 30-50%) bin. The green [9] and yellow [10] points show theoretical predictions made using chiral perturbation theory.

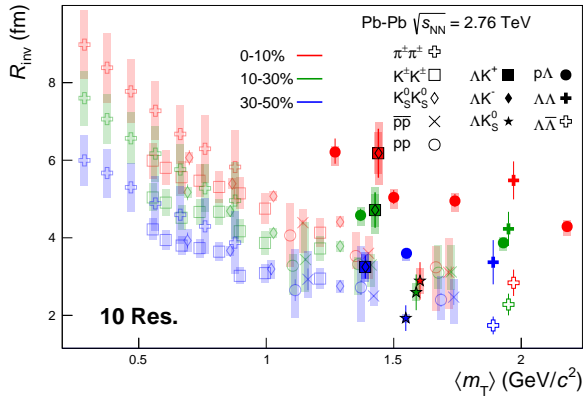
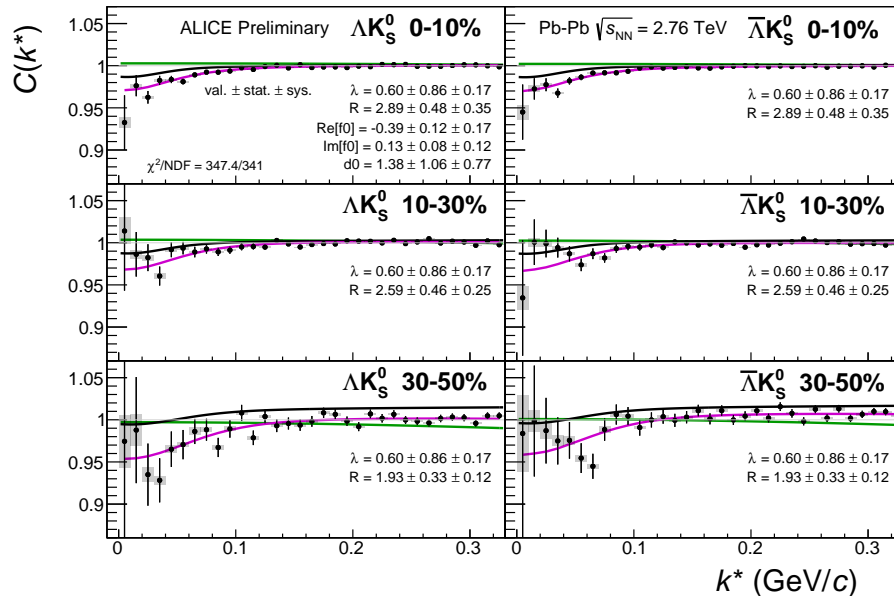
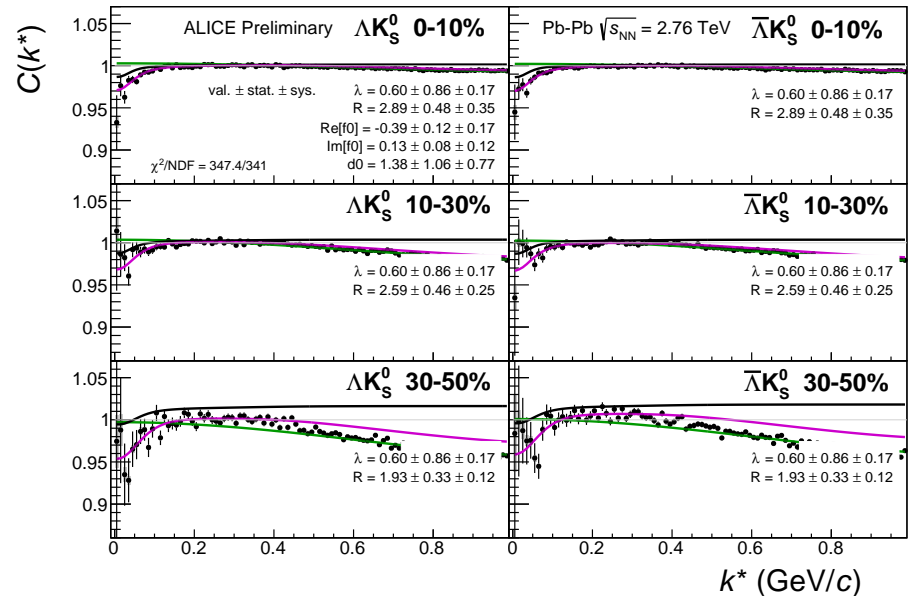


Fig. 43: 10 residual correlations in ΛK fits. Extracted fit R_{inv} parameters as a function of pair transverse mass (m_T) for various pair systems over several centralities. The ALICE published data [11] is shown with transparent, open symbols. The new ΛK results are shown with opaque, filled symbols. In the left, the ΛK^+ (with its conjugate pair) results are shown separately from the ΛK^- (with its conjugate pair) results. In the right, all ΛK^\pm results are averaged.

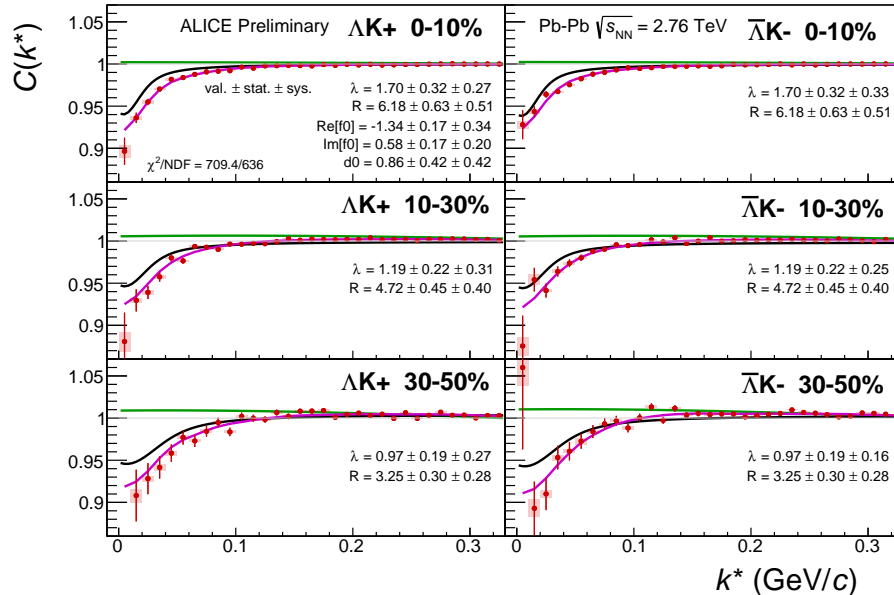


(a) Signal region view ($k^* \lesssim 0.3$ GeV/c)

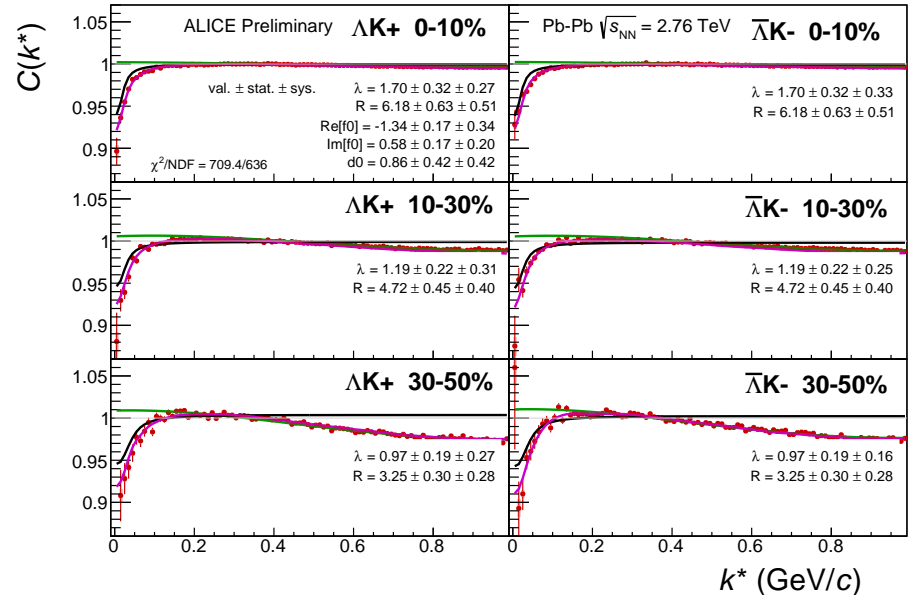


(b) Wide view ($k^* \lesssim 1.0$ GeV/c)

Fig. 44: Fits, with 10 residual correlations included, to the ΛK_s^0 (left) and $\bar{\Lambda} K_s^0$ (right) data for the centralities 0-10% (top), 10-30% (middle), and 30-50% (bottom). The lines represent the statistical errors, while the boxes represent the systematic errors. A single λ parameter is shared amongst all. Each analysis has a unique normalization parameter. The radii are shared between analyses of like centrality, as these should have similar source sizes. The scattering parameters ($\mathbb{R} f_0$, $\mathbb{I} f_0$, d_0) are shared amongst all. The background is modeled by a (6th-degree polynomial fit to THERMINATOR simulation. The black solid line represents the primary (ΛK) correlation's contribution to the fit. The green line shows the fit to the non-flat background. The purple points show the fit after all residuals' contributions have been included, and momentum resolution and non-flat background corrections have been applied. The extracted fit values with uncertainties are printed.

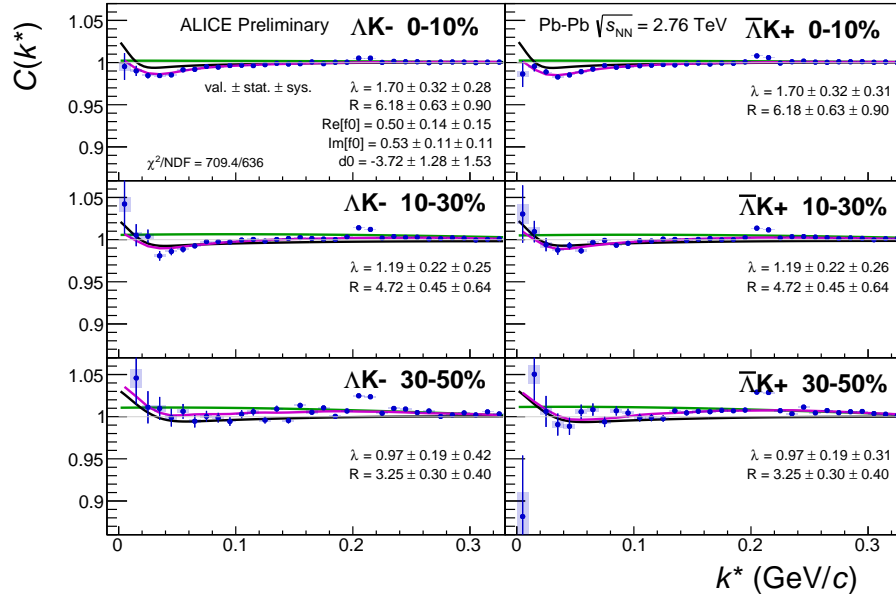


(a) Signal region view ($k^* \lesssim 0.3 \text{ GeV}/c$)

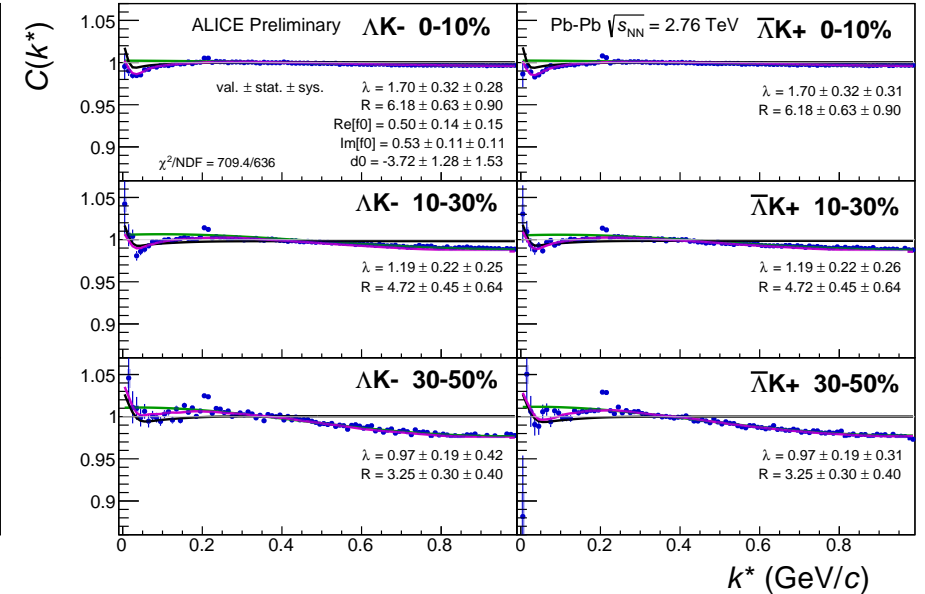


(b) Wide view ($k^* \lesssim 1.0 \text{ GeV}/c$)

Fig. 45: Fits, with 10 residual correlations included, to the ΔK^+ (left) and $\bar{\Delta} K^-$ (right) data for the centralities 0-10% (top), 10-30% (middle), and 30-50% (bottom). The lines represent the statistical errors, while the boxes represent the systematic errors. All ΔK^\pm analyses are fit simultaneously across all centralities (0-10%, 10-30%, 30-50%). Scattering parameters ($\Re f_0$, $\Im f_0$, d_0) are shared between pair-conjugate systems (i.e. a parameter set describing the ΔK^+ & $\bar{\Delta} K^-$ system, and a separate set describing the ΔK^- & $\bar{\Delta} K^+$ system). For each centrality, a radius and λ parameters are shared between all pairs (ΔK^+ , $\bar{\Delta} K^-$, ΔK^- , $\bar{\Delta} K^+$). Each analysis has a unique normalization parameter. The background is modeled by a (6th-degree polynomial fit to THERMINATOR simulation. The black solid line represents the primary (ΔK) correlation's contribution to the fit. The green line shows the fit to the non-flat background. The purple points show the fit after all residuals' contributions have been included, and momentum resolution and non-flat background corrections have been applied. The extracted fit values with uncertainties are printed.



(a) Signal region view ($k^* \lesssim 0.3 \text{ GeV}/c$)



(b) Wide view ($k^* \lesssim 1.0 \text{ GeV}/c$)

Fig. 46: Fits, with 10 residual correlations included, to the ΔK^- (left) with $\bar{\Delta}K^+$ (right) data for the centralities 0-10% (top), 10-30% (middle), and 30-50% (bottom). The lines represent the statistical errors, while the boxes represent the systematic errors. All ΔK^\pm analyses are fit simultaneously across all centralities (0-10%, 10-30%, 30-50%). Scattering parameters ($\text{Re}[f_0]$, $\text{Im}[f_0]$, d_0) are shared between pair-conjugate systems (i.e. a parameter set describing the ΔK^+ & $\bar{\Delta}K^-$ system, and a separate set describing the ΔK^- & $\bar{\Delta}K^+$ system). For each centrality, a radius and λ parameters are shared between all pairs (ΔK^+ , $\bar{\Delta}K^-$, ΔK^- , $\bar{\Delta}K^+$). Each analysis has a unique normalization parameter. The background is modeled by a (6th-degree polynomial fit to THERMINATOR simulation. The black solid line represents the primary (ΔK) correlation's contribution to the fit. The green line shows the fit to the non-flat background. The purple points show the fit after all residuals' contributions have been included, and momentum resolution and non-flat background corrections have been applied. The extracted fit values with uncertainties are printed.

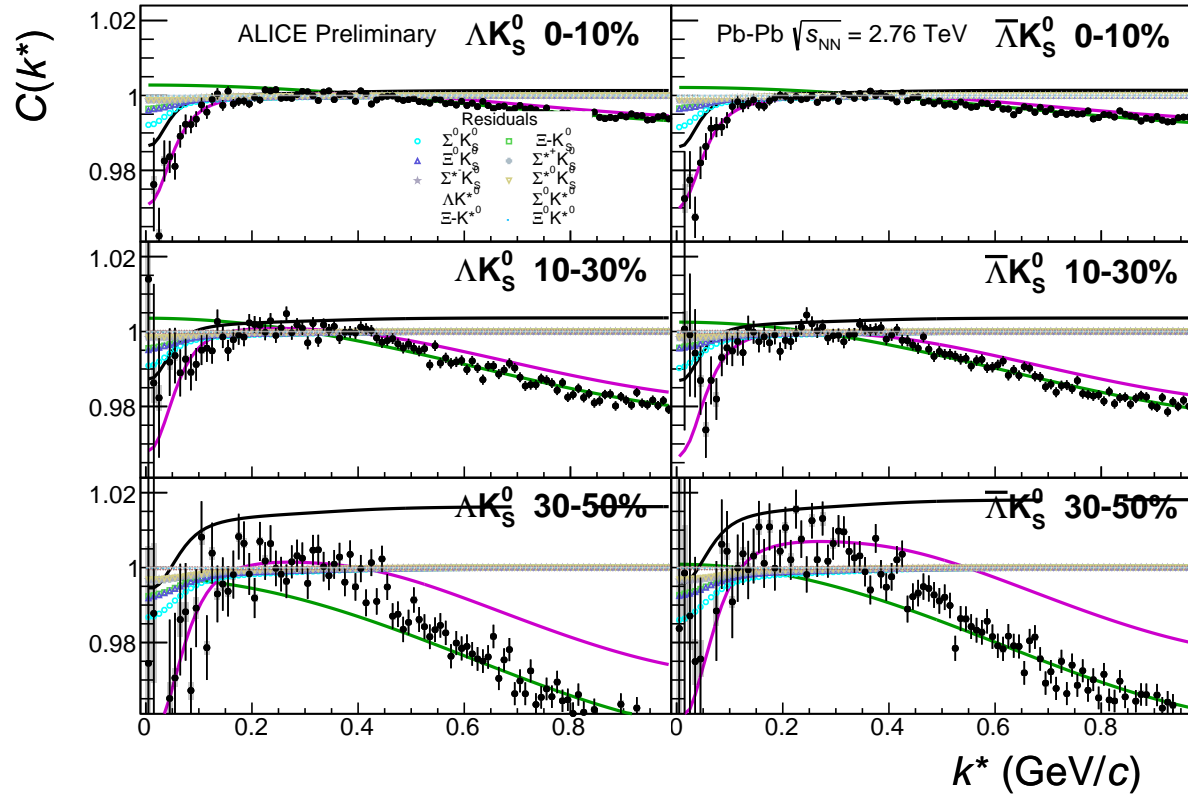
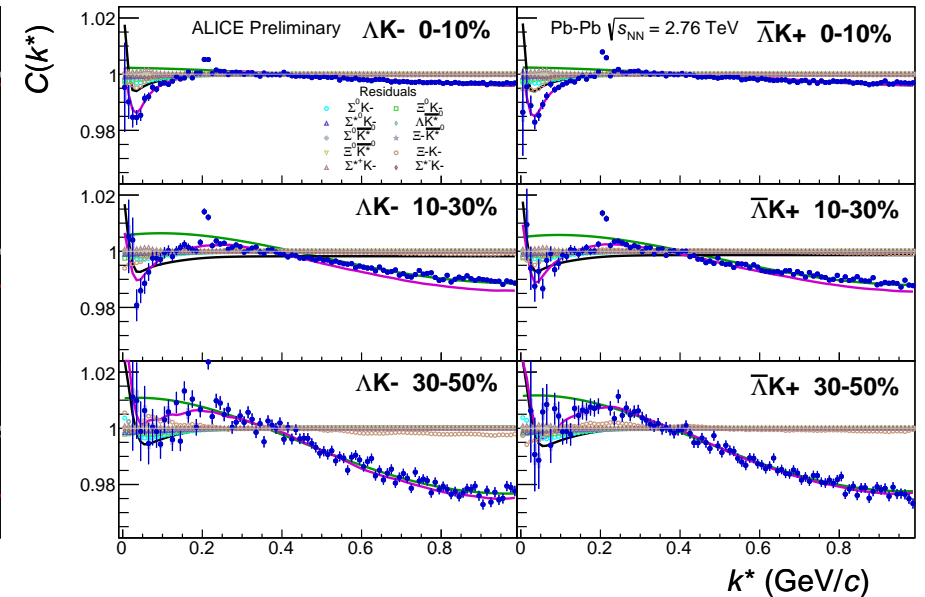
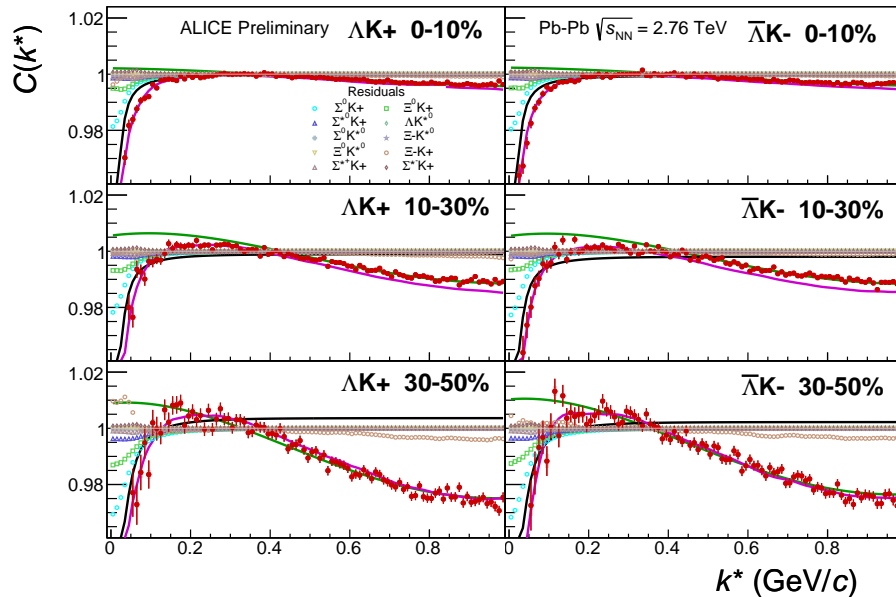


Fig. 47: Fits, with 10 residual correlations included and shown, to the ΛK_S^0 (left) and $\bar{\Lambda} K_S^0$ (right) data for the centralities 0-10% (top), 10-30% (middle), and 30-50% (bottom). The ten parent pairs used for the residual correction to the ΛK_S^0 ($\bar{\Lambda} K_S^0$) fit are $\Sigma^0 K_S^0$, $\Xi^0 K_S^0$, $\Xi^- K_S^0$, $\Sigma^{*(+,-,0)} K_S^0$, ΛK^{*0} , $\Sigma^0 K^{*0}$, $\Xi^0 K^{*0}$, and $\Xi^- K^{*0}$ ($\bar{\Sigma}^0 K_S^0$, $\bar{\Xi}^0 K_S^0$, $\bar{\Xi}^+ K_S^0$, $\bar{\Sigma}^{*(+,-,0)} K_S^0$, $\bar{\Lambda} K^{*0}$, $\bar{\Sigma}^0 K^{*0}$, $\bar{\Xi}^0 K^{*0}$, and $\bar{\Xi}^- K^{*0}$).



(a) $\Lambda K^+(\bar{\Lambda}K^-)$ fits with residual contributions shown for the centralities 0-10% (top), 10-30% (middle), and 30-50% (bottom)

(b) $\Lambda K^-(\bar{\Lambda}K^+)$ fits with residual contributions shown for the centralities 0-10% (top), 10-30% (middle), and 30-50% (bottom)

Fig. 48: Fits, with 10 residual correlations included and shown, to the ΛK^+ & $\bar{\Lambda}K^-$ (left) and ΛK^- & $\bar{\Lambda}K^+$ (right) data for the centralities 0-10% (top), 10-30% (middle), and 30-50% (bottom). The ten parent pairs used for the residual correction to the $\Lambda K^+(\bar{\Lambda}K^-)$ fit are $\Sigma^0 K^+$, $\Xi^0 K^+$, $\Xi^- K^+$, $\Sigma^{*(+,-,0)} K^+$, ΛK^{*0} , $\Sigma^0 K^{*0}$, $\Xi^0 K^{*0}$, and $\Xi^- K^{*0}$ ($\Sigma^0 K^-$, $\Xi^0 K^-$, $\Xi^+ K^-$, $\Sigma^{*(+,-,0)} K^-$, $\bar{\Lambda}K^{*0}$, $\Sigma^0 \bar{K}^{*0}$, $\Xi^0 \bar{K}^{*0}$, and $\Xi^+ \bar{K}^{*0}$).

Fit Results $\Lambda(\bar{\Lambda})K_S^0$						
System	Centrality	Fit Parameters				
		λ	R	$\mathbb{R}f_0$	$\mathbb{I}f_0$	d_0
$\Lambda K_S^0 \text{ & } \bar{\Lambda} K_S^0$	0-10%			$2.89 \pm 0.48 \text{ (stat.)} \pm 0.33 \text{ (sys.)}$		
	10-30%	$0.60 \pm 0.86 \text{ (stat.)} \pm 0.16 \text{ (sys.)}$	$2.59 \pm 0.46 \text{ (stat.)} \pm 0.23 \text{ (sys.)}$	$-0.39 \pm 0.12 \text{ (stat.)} \pm 0.16 \text{ (sys.)}$	$0.13 \pm 0.08 \text{ (stat.)} \pm 0.13 \text{ (sys.)}$	$1.38 \pm 1.06 \text{ (stat.)} \pm 0.62 \text{ (sys.)}$
	30-50%			$1.93 \pm 0.33 \text{ (stat.)} \pm 0.11 \text{ (sys.)}$		

Table 9: Fit Results $\Lambda(\bar{\Lambda})K_S^0$, with 10 residual correlations included. Each pair is fit simultaneously with its conjugate (ie. ΛK_S^0 with $\bar{\Lambda} K_S^0$) across all centralities (0-10%, 10-30%, 30-50%), for a total of 6 simultaneous analyses in the fit. A single λ parameter is shared amongst all. Each analysis has a unique normalization parameter. The radii are shared between analyses of like centrality, as these should have similar source sizes. The scattering parameters ($\mathbb{R}f_0$, $\mathbb{I}f_0$, d_0) are shared amongst all. The background is modeled by a (6th-)degree polynomial fit to THERMINATOR simulation. The fit is done on the data with only statistical error bars. The errors marked as “stat.” are those returned by MINUIT. The errors marked as “sys.” are those which result from my systematic analysis (as outlined in Section 6).

Fit Results $\Lambda(\bar{\Lambda})K^\pm$						
System	Centrality	Fit Parameters				
		λ	R	$\mathbb{R}f_0$	$\mathbb{I}f_0$	d_0
$\Lambda K^+ \text{ & } \bar{\Lambda} K^-$	0-10%	$1.70 \pm 0.32 \text{ (stat.)} \pm 0.28 \text{ (sys.)}$	$6.18 \pm 0.63 \text{ (stat.)} \pm 0.54 \text{ (sys.)}$	$-1.34 \pm 0.17 \text{ (stat.)} \pm 0.36 \text{ (sys.)}$	$0.58 \pm 0.17 \text{ (stat.)} \pm 0.23 \text{ (sys.)}$	$0.86 \pm 0.42 \text{ (stat.)} \pm 0.53 \text{ (sys.)}$
	10-30%	$1.19 \pm 0.22 \text{ (stat.)} \pm 0.36 \text{ (sys.)}$	$4.72 \pm 0.45 \text{ (stat.)} \pm 0.42 \text{ (sys.)}$			
$\Lambda K^+ \text{ & } \bar{\Lambda} K^-$	30-50%	$0.97 \pm 0.19 \text{ (stat.)} \pm 0.31 \text{ (sys.)}$	$3.25 \pm 0.30 \text{ (stat.)} \pm 0.32 \text{ (sys.)}$	$0.50 \pm 0.14 \text{ (stat.)} \pm 0.14 \text{ (sys.)}$	$0.53 \pm 0.11 \text{ (stat.)} \pm 0.11 \text{ (sys.)}$	$-3.72 \pm 1.28 \text{ (stat.)} \pm 1.33 \text{ (sys.)}$

Table 10: Fit Results $\Lambda(\bar{\Lambda})K^\pm$, with 10 residual correlations included. All ΛK^\pm analyses are fit simultaneously across all centralities (0-10%, 10-30%, 30-50%). Scattering parameters ($\mathbb{R}f_0$, $\mathbb{I}f_0$, d_0) are shared between pair-conjugate systems (i.e. a parameter set describing the $\Lambda K^+ \text{ & } \bar{\Lambda} K^-$ system, and a separate set describing the $\Lambda K^- \text{ & } \bar{\Lambda} K^+$ system). For each centrality, a radius and λ parameters are shared between all pairs ($\Lambda K^+, \bar{\Lambda} K^-, \Lambda K^-, \bar{\Lambda} K^+$). Each analysis has a unique normalization parameter. The background is modeled by a (6th-)degree polynomial fit to THERMINATOR simulation. The fit is done on the data with only statistical error bars. The errors marked as “stat.” are those returned by MINUIT. The errors marked as “sys.” are those which result from my systematic analysis (as outlined in Section 6).

821 **7.1.4 Results: ΛK_S^0 and ΛK^\pm : Fit Method Comparisons**

822 In Figure 49, we show extracted fit parameters for the case of $\Lambda K^+(\bar{\Lambda}K^-)$ sharing radii with $\Lambda K^-(\bar{\Lambda}K^+)$.
 823 The figure shows results for three different treatments of the non-femtoscopic background: a polynomial
 824 fit to THERMINATOR 2 simulation to model the background (circles), a linear fit to the data to model
 825 the background (squares), and the Stavinsky method (crosses).

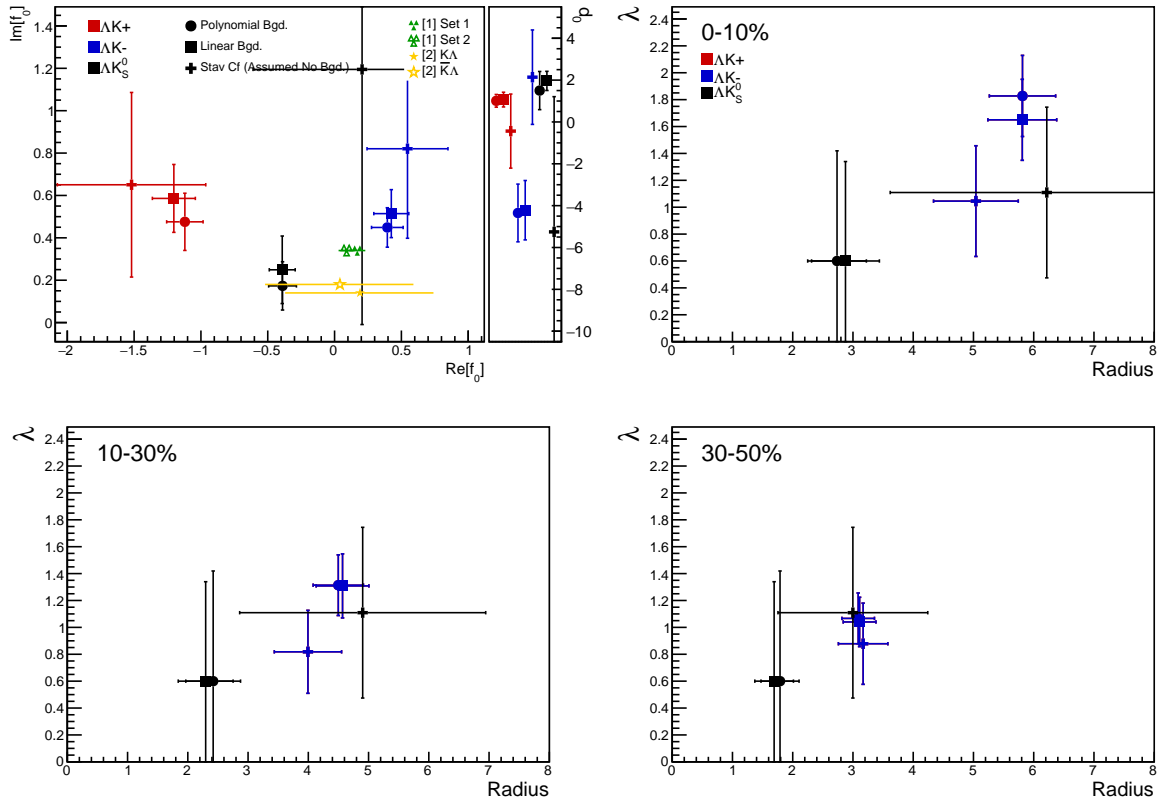


Fig. 49: Compare Fit Parameters: Background treatment: Extracted fit results for all of our $\Lambda(\bar{\Lambda})K^\pm$ systems across all studied centrality bins (0-10%, 10-30%, 30-50%). The $\Lambda K^+(\bar{\Lambda}K^-)$ and $\Lambda K^-(\bar{\Lambda}K^+)$ systems share both a radius and a λ parameter for each centrality bin (i.e. 3 total radius parameters, 3 total λ parameters). The figure shows results for three different treatments of the non-femtoscopic background: a polynomial fit to THERMINATOR 2 simulation to model the background (circles), a linear fit to the data to model the background (squares), and the Stavinsky method (crosses). The green [9] and yellow [10] points show theoretical predictions made using chiral perturbation theory.

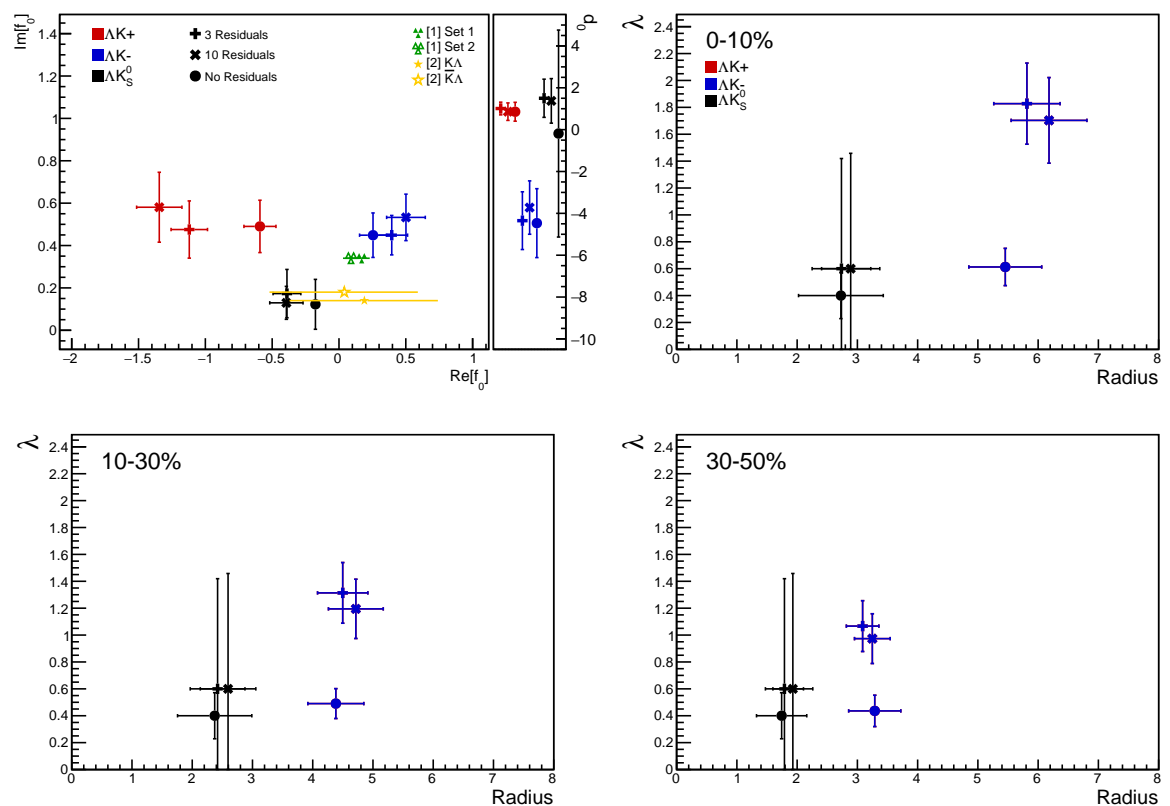


Fig. 50: Compare Fit Parameters: Number of residuals: Results shown for the case of 3 (+), 10 (X), and no (circles) residual contributors.

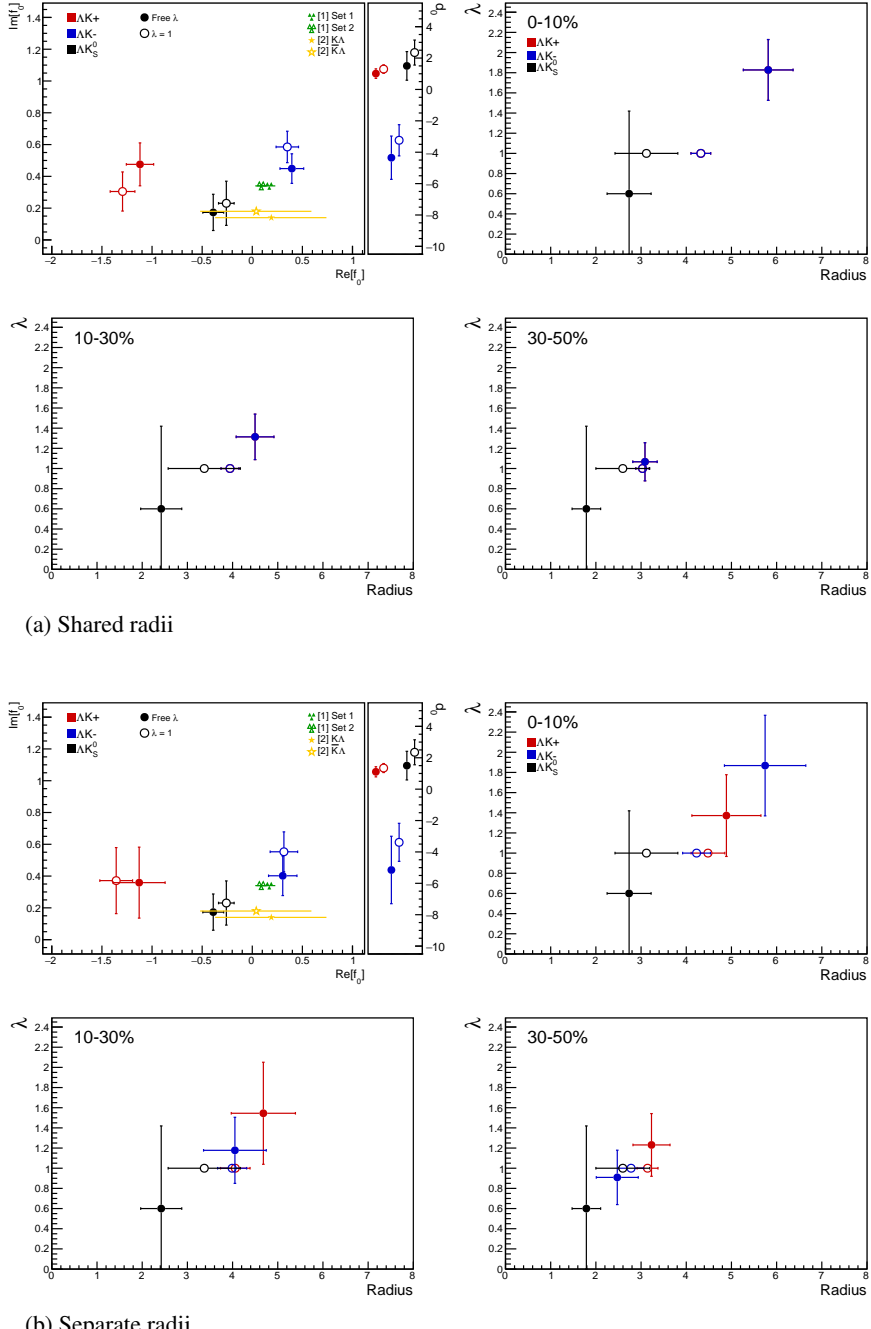


Fig. 51: Compare Fit Parameters: Free vs fixed λ : Results shown for λ parameters left free (filled symbols) and fixed to 1 (open symbols). In the top plot (51a), the ΛK^+ and ΛK^- analyses share radii, whereas in the bottom (51b) they have unique radii.

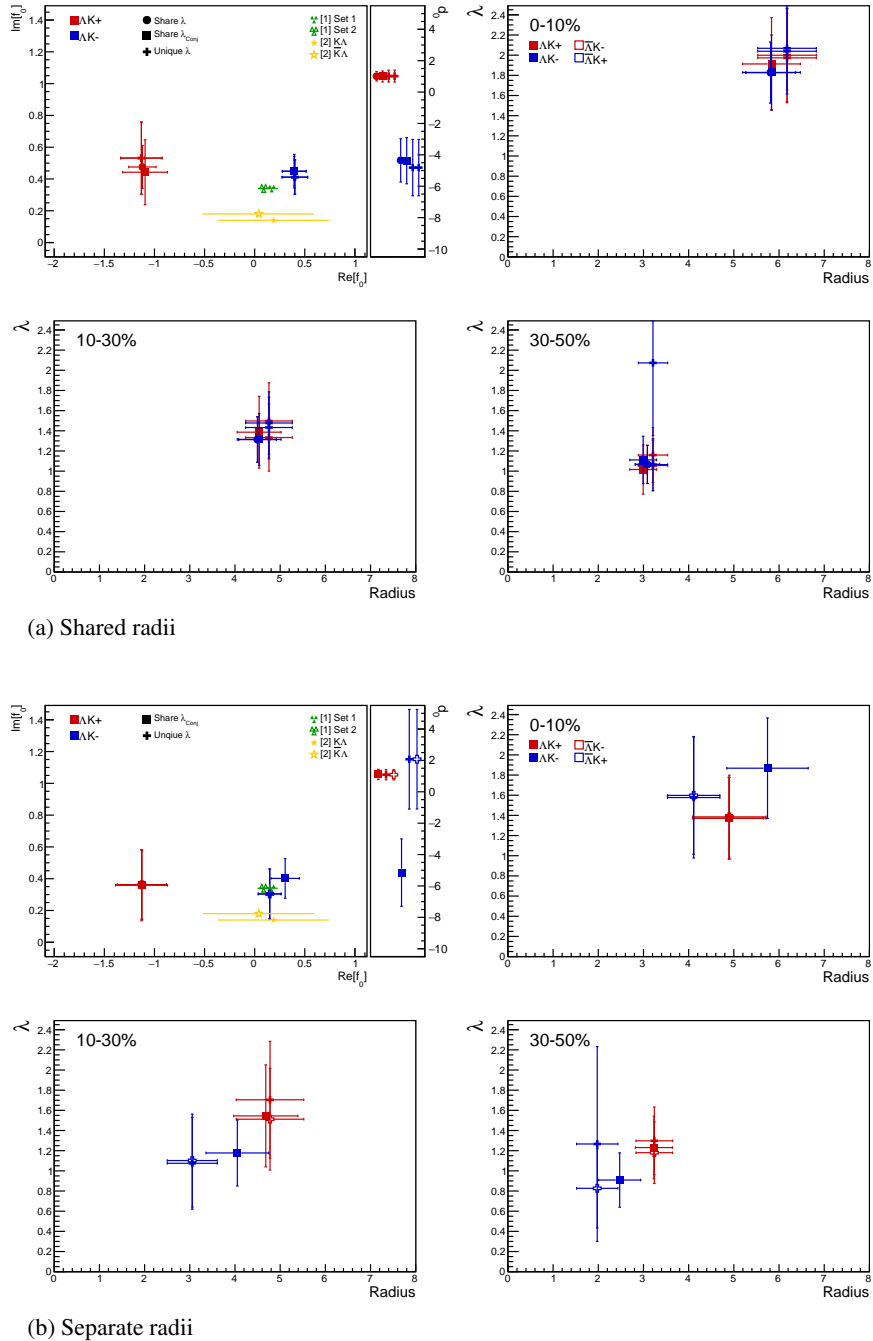


Fig. 52: Compare Fit Parameters: Shared vs unique λ : Results shown for different sharing of the λ parameters between analyses and systems. In the top (52a), the ΛK^+ and ΛK^- analyses share radii, whereas in the bottom (52b), they do not. “Share λ ” (circles) is the case where a single λ is shared amongst all analyses for a given centrality bin (i.e., in 52a, 3 radius parameters and 3 λ parameters). “Share λ_{Conj} ” (squares) means that conjugate pairs (ex. ΛK^+ and $\bar{\Lambda} K^-$) share a λ parameter for each centrality. This corresponds to 6 total λ parameters (for each of the 3 centrality bins, the $\Lambda K^+(\bar{\Lambda} K^-)$ receives a unique λ , as does $\Lambda K^-(\bar{\Lambda} K^+)$). Finally, in “Unique λ ” (+), each analysis received its own unique λ parameter. This corresponds to 12 λ parameters (for each of the 3 centrality bins, each ΛK^+ , $\bar{\Lambda} K^-$, ΛK^- , and $\bar{\Lambda} K^+$ receives a unique λ).

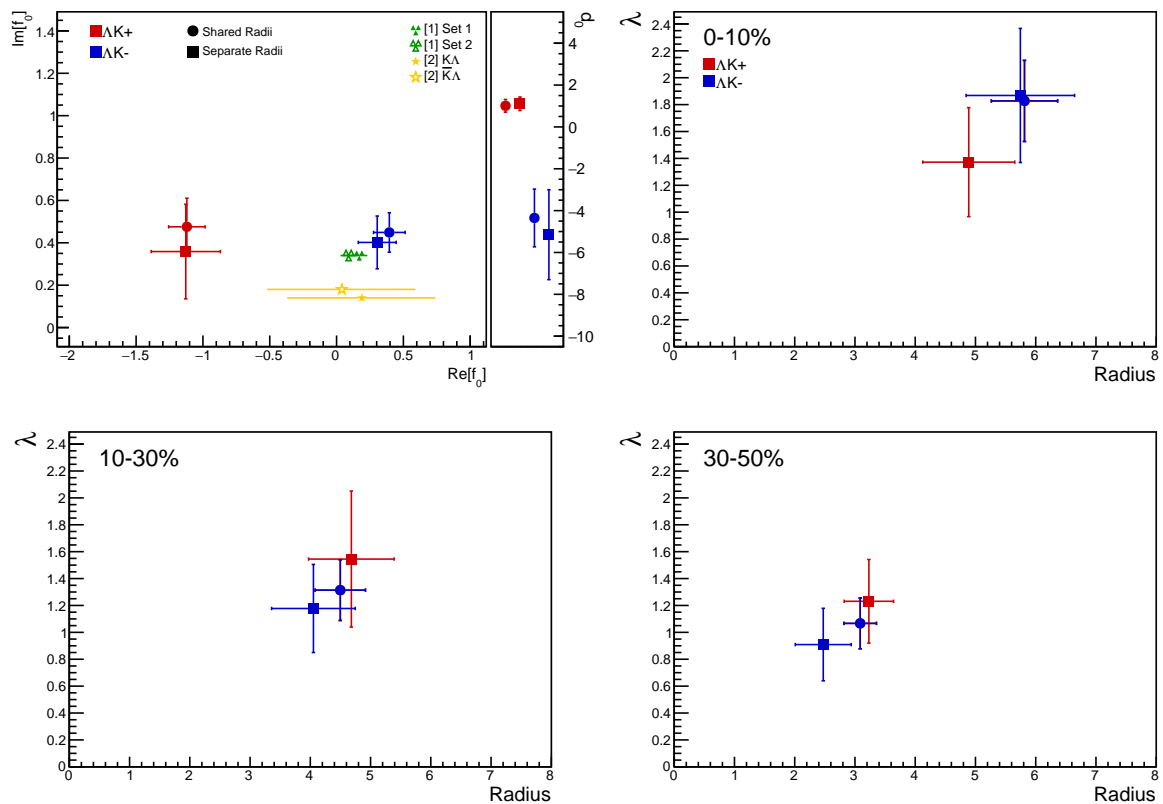


Fig. 53: Compare Fit Parameters: Shared vs. Separate Radii: Results shown for the case of radii being shared between $\Lambda K^+(\bar{\Lambda} K^-)$ and $\Lambda K^-(\bar{\Lambda} K^+)$ (circles) vs not shared (squares).

826 **7.2 Results: ΞK^\pm**

827 Even without any fits to the data, the fact that the $\Xi^- K^+$ data dips below unity (Fig. 54) is exciting, as
 828 this cannot occur purely from a Coulomb interaction. We hope that this dip signifies that we are able to
 829 peer through the overwhelming contribution from the Coulomb interaction to see the effects arising from
 830 the strong interaction.

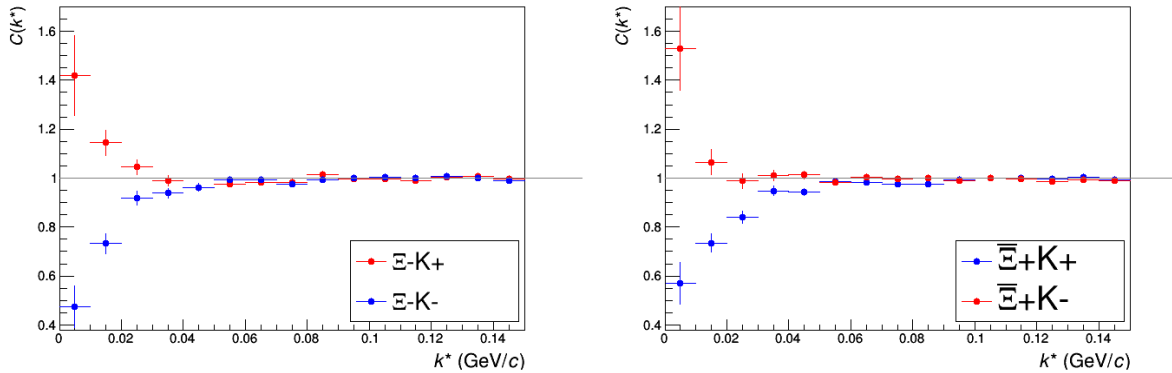


Fig. 54: ΞK^\pm Results for 0-10% Centrality. (Left) $\Xi^- K^+$ and $\Xi^- K^-$ (Right) $\Xī^+ K^+$ and $\Xī^+ K^-$

831 Figure 55 demonstrates graphically, that the $\Xi^- K^+$ results cannot be described by solely the Coulomb
 832 interaction. In this figure, we present the data along with a Coulomb-only band. The Coulomb-only
 833 band is spanned by two Coulomb-only curves, whose parameters are given in the figure. The Coulomb-only
 834 curves were generated using a technique identical to the generation of the fit function, described
 835 in Sec. 5.2, except, of course, with the nuclear scattering parameters all set to zero. The Coulomb-only
 836 curves change monotonically with varying λ or varyin radius parametres, therefore, any curves built with
 837 parameter sets intermediate to those use in the Coulomb-only band will be contained in the band.

838 Including the strong interaction into the simulation can change, sometimes dramatically, the resulting
 839 correlation function, as shown in Figure 56. In the figure, the solid line represents a Coulomb-only curve,
 840 i.e. a simulated correlation function with the strong interaction turned off. The dashed lines represent a
 841 full simulation, including both the strong and Coulomb interactions. The two dashed lines differ only in
 842 the real part of the assumed scattering length: positive in Set 1, and negative in Set 2. In the top figure,
 843 for the $\Xi^- K^+$ simulation, we see that parameter set 2, with a negative real part of the scattering length,
 844 causes the simulated curve to dip below unity, as is seen in the data. If there is a parallel to be drawn
 845 between this analysis and the ΛK analysis, we expect to see similar effects in the ΛK^+ system and the
 846 $\Xi^- K^+$ systems. In these systems, we could have an $s\bar{s}$ annihilation picture. Or, another possible way of
 847 thinking about these systems is in terms of net strangeness. The ΛK^+ system has $S=0$, while the ΛK^-
 848 has $S=-2$. The $\Xi^- K^+$ has $S=-1$, while the $\Xi^- K^-$ has $S=-3$.

849 The author was asked to perform a global Coulomb-only fit to the data, to ensure that the system truly
 850 could not be described simply by the Coulomb interaction. In order words, in the fit, the strong force was
 851 turned off, and the $\Xi^- K^+$, $\Xī^+ K^-$, $\Xi^- K^-$, $\Xī^+ K^+$ systems all share one sinlge radius parameter, while the
 852 pair and conjugate pair systems share a λ parameter. The results of this fit are shown in Figures 57 and
 853 58. In Fig. 57, there was a lower limit of 0.1 fm placed on the radius parameter, and the radius parameter
 854 was initialized to 3 fm (as seems reasonable, when considering the transverse mass of the system and
 855 looking at Fig. ??). As is shown in the results, the radius parameter reached this unrealistic lower bound
 856 of 0.1 fm. In Fig. 58, the parameters were all unbounded, and the radius parameter was initialized to 10
 857 fm. In this case, the radius parameters reamins high, and ends at an unrealistic value of 10.84 fm. In both
 858 cases, the λ parameters are too low. From these figures, we conclude that a global Coulomb-only fit is
 859 not suitable for the data.

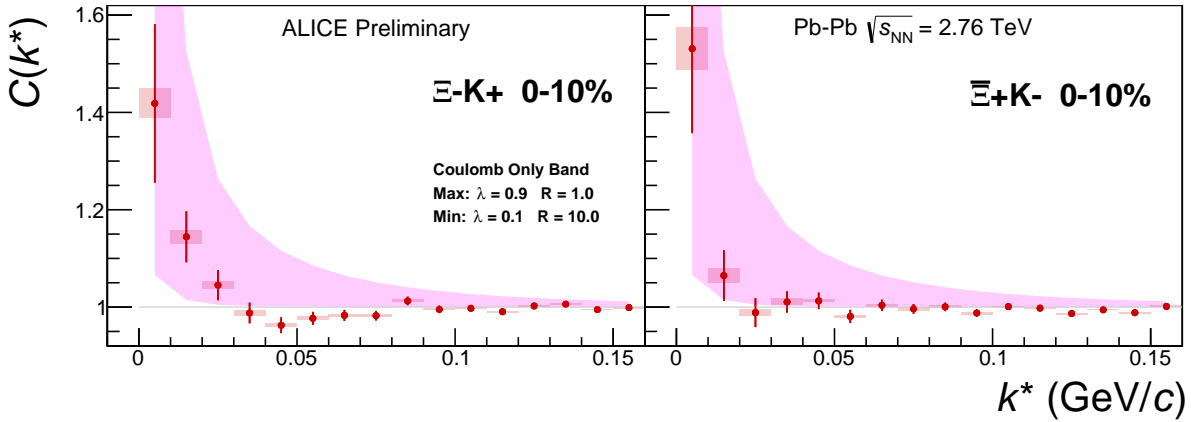
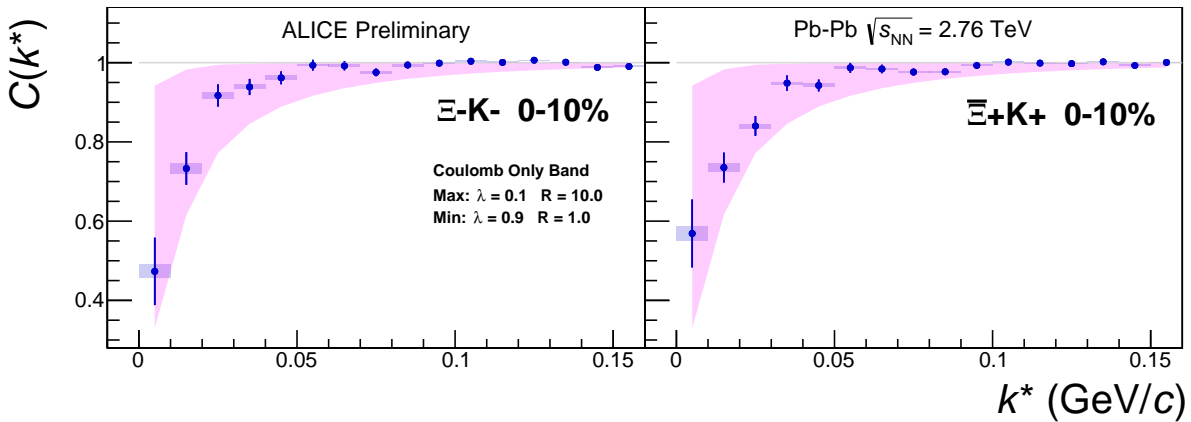
(a) (Left) ΞK^+ and (Right) $\bar{\Xi} K^-$ (b) (Left) ΞK^- and (Right) $\bar{\Xi} K^+$

Fig. 55: ΞK^\pm data with Coulomb-only bands for the 0-10% centrality bin. The Coulomb-only bands span two sets of Coulomb-only curves: (1) $\lambda = 0.9$, $R = 1.0$ fm and (2) $\lambda = 0.1$, $R = 10.0$ fm. The Coulomb-only curves are simulated correlation functions for the respective pair system assuming only a Coulomb interaction, i.e. ignoring the strong interaction. The Coulomb-only curves change monotonically with varying λ and varying R , therefore, any intermediate parameter set will fall within this Coulomb-only band.

Although the global Coulomb-only fit failed, it is possible that a Coulomb-only fit performed on $\Xi^- K^+$ and $\bar{\Xi}^+ K^-$ separately from $\Xi^- K^-$ and $\bar{\Xi}^+ K^+$ could be suitable. The result of such fits are shown in Figures 59 and 60. Figure 59, shows that the fit is not able to describe the dip in the $\Xi^- K^+$ data below unity. Of course, this is obviously true for an attractive Coulomb-only fit. The radius parameter of 8.43 fm extracted from this fit is unrealistically large. In Figure 60 shows the Coulomb-only fit can described the $\Xi^- K^-$ data reasonable well; although the extracted radius of 3.73 fm is somewhat larger than expected.

8 To Do

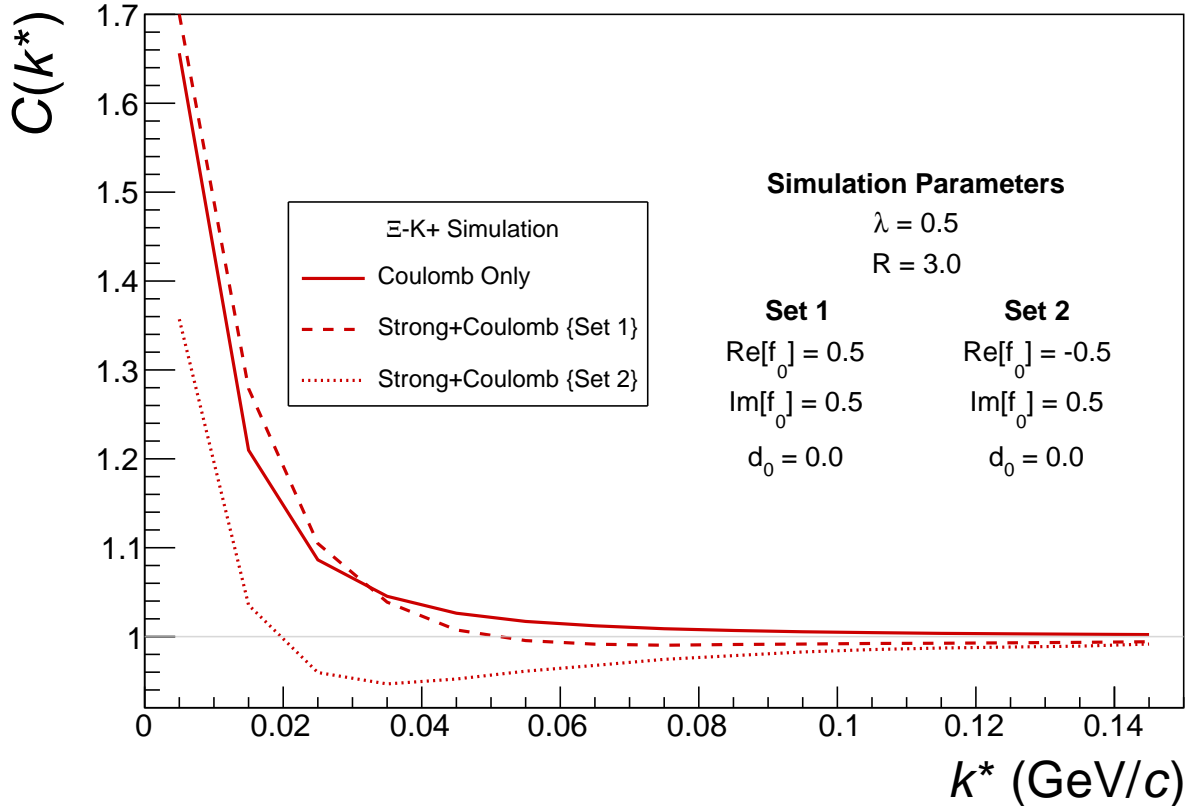
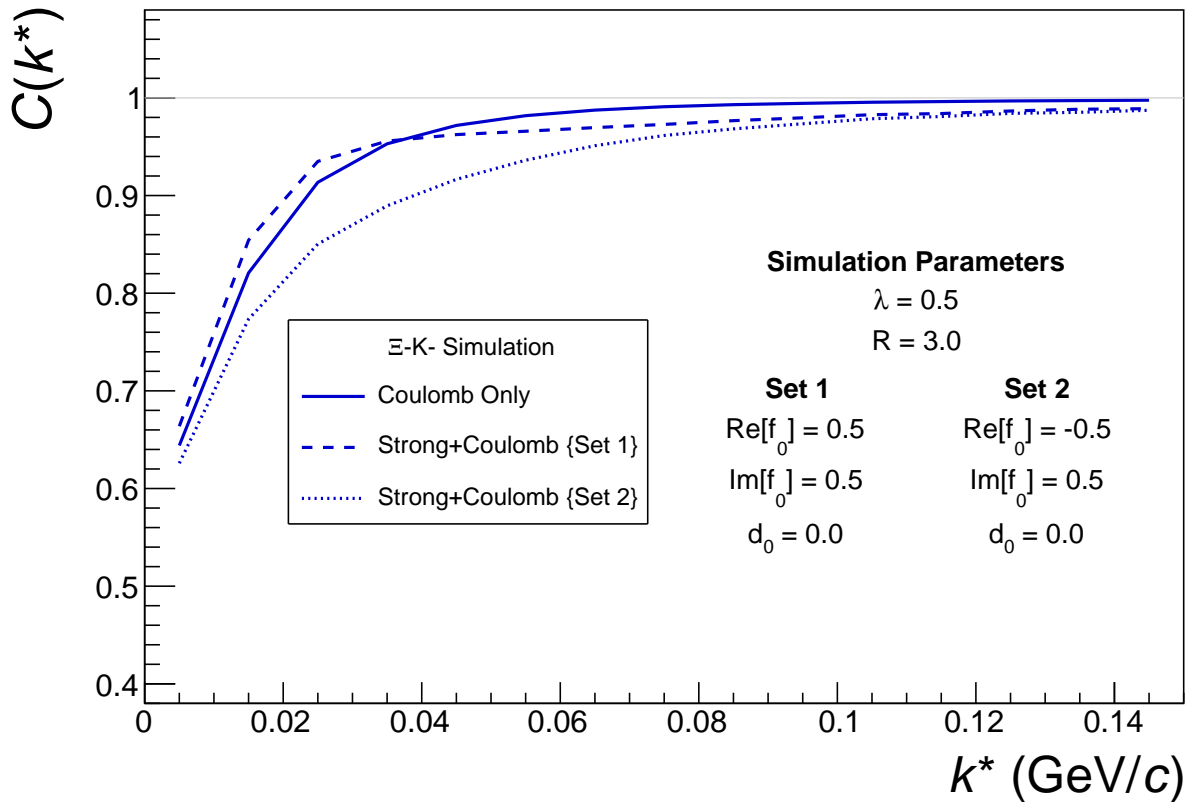

 (a) ΞK^+ and $\bar{\Xi} K^-$ simulation

 (b) ΞK^- and $\bar{\Xi} K^+$ simulation

Fig. 56: Effect on the Coulomb-only curve of including the strong interaction for ΞK^\pm systems. The solid line represents a Coulomb-only curve, i.e. a simulated correlation function with the strong interaction turned off. The dashed lines represent a full simulation, including both the strong and Coulomb interactions. The two dashed lines differ only in the real part of the assumed scattering length: positive in Set 1, and negative in Set 2.

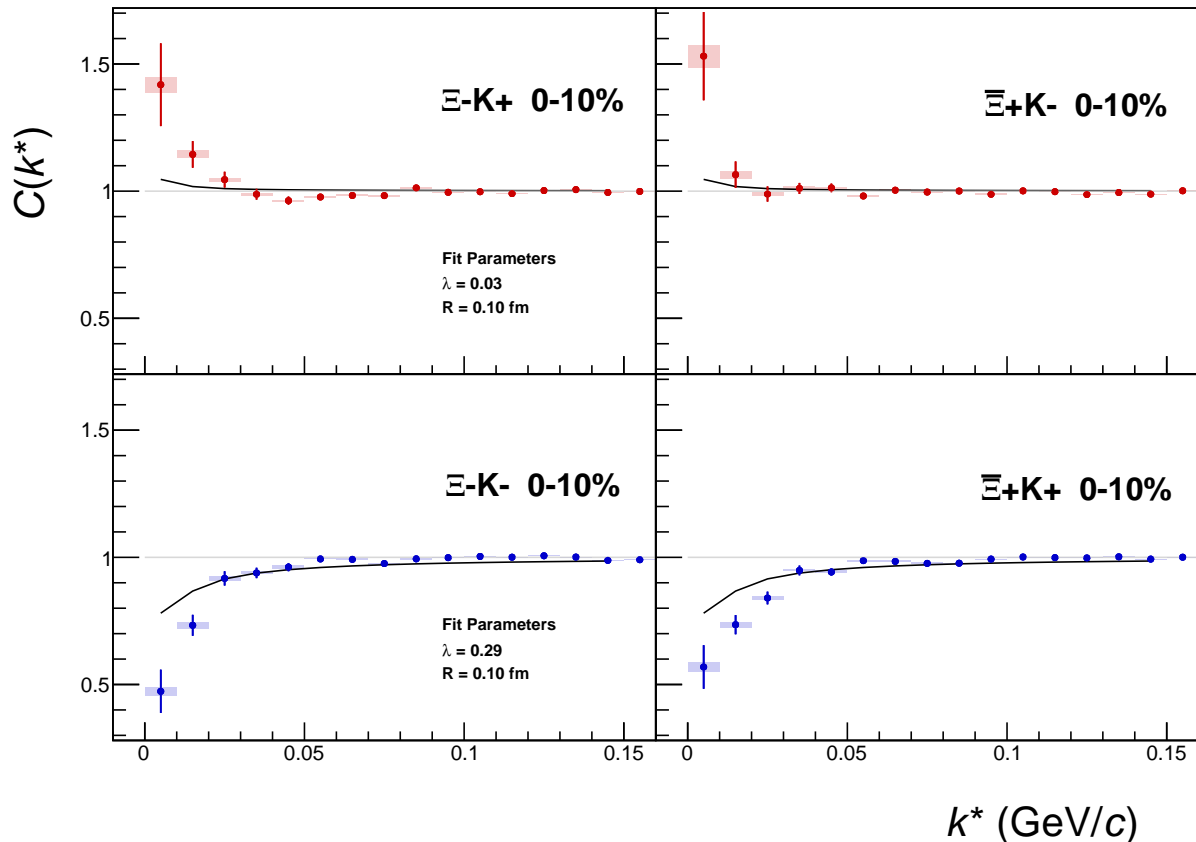


Fig. 57: ΞK^\pm Global Coulomb-only fit (Set 1) for 0-10% centrality. In this fit, there was a lower limit of 0.1 fm placed on the radius parameter, and the radius parameter was initialized to 3 fm (as seems reasonable, when considering the transverse mass of the system and looking at Fig. ??). As is shown in the results, the radius parameter reached this unrealistic lower bound of 0.1 fm. Also, the extracted λ parameters are too low.

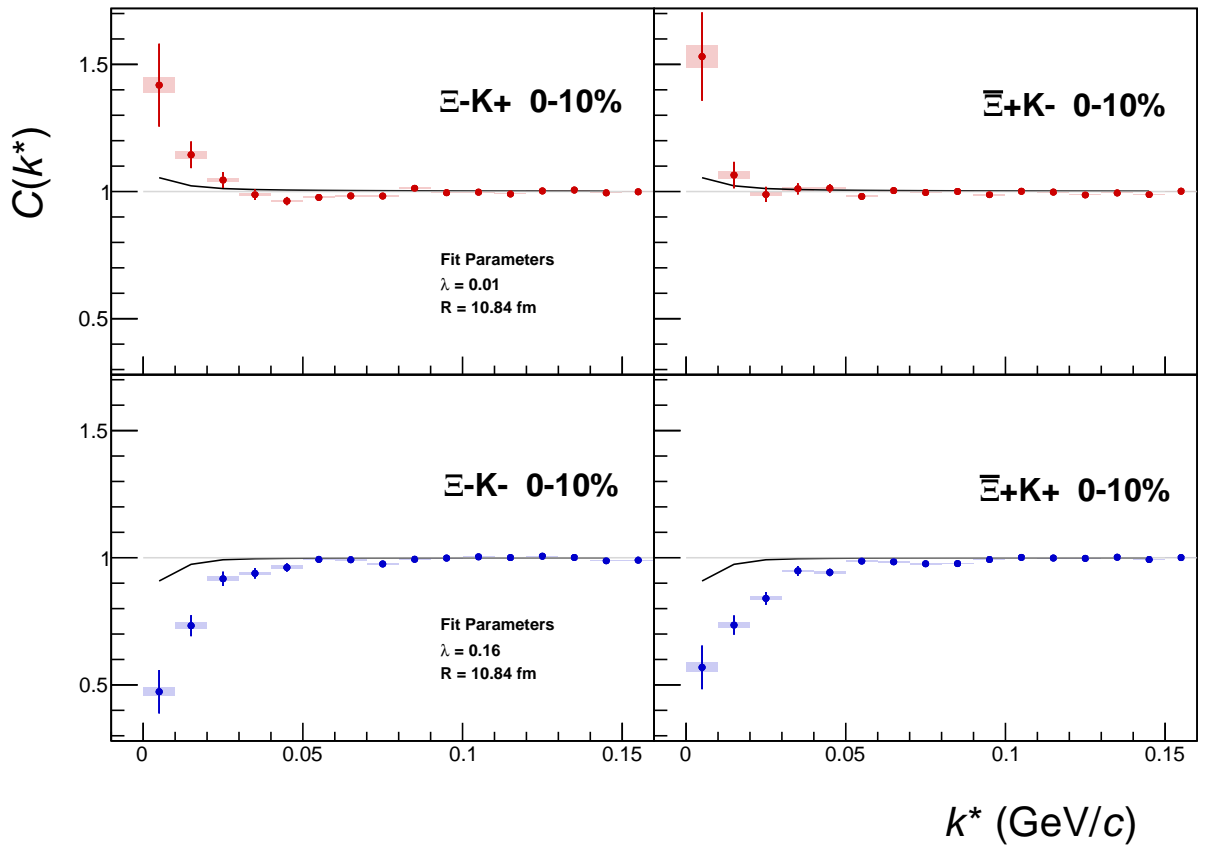


Fig. 58: ΞK^\pm Global Coulomb-only fit (Set 2) for 0-10% centrality. In this fit, the parameters were all unbounded, and the radius parameter was initialized to 10 fm. In this case, the radius parameters remain high, and ends at an unrealistic value of 10.84 fm. Also, the extracted λ parameters are too low.

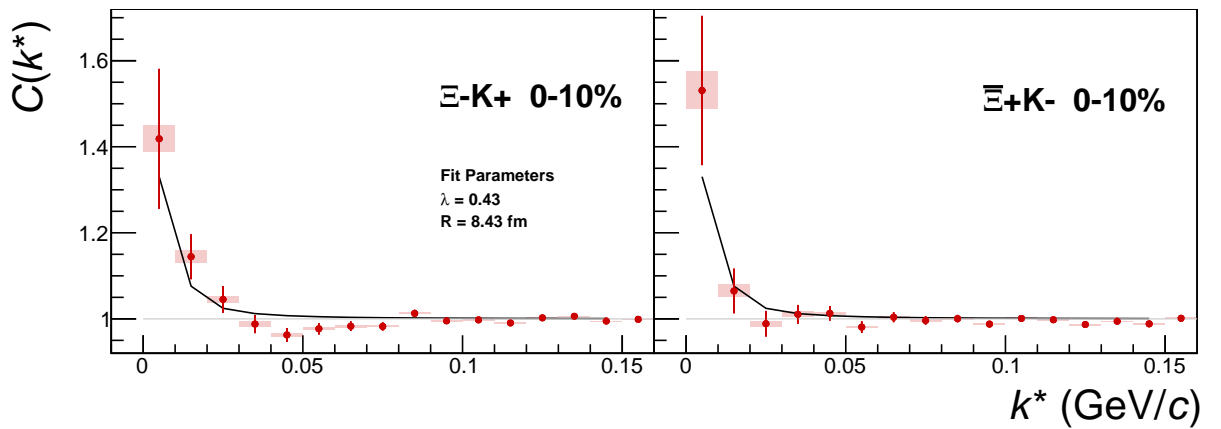


Fig. 59: $\Xi^- K^+$ Coulomb-only fit for 0-10% centrality

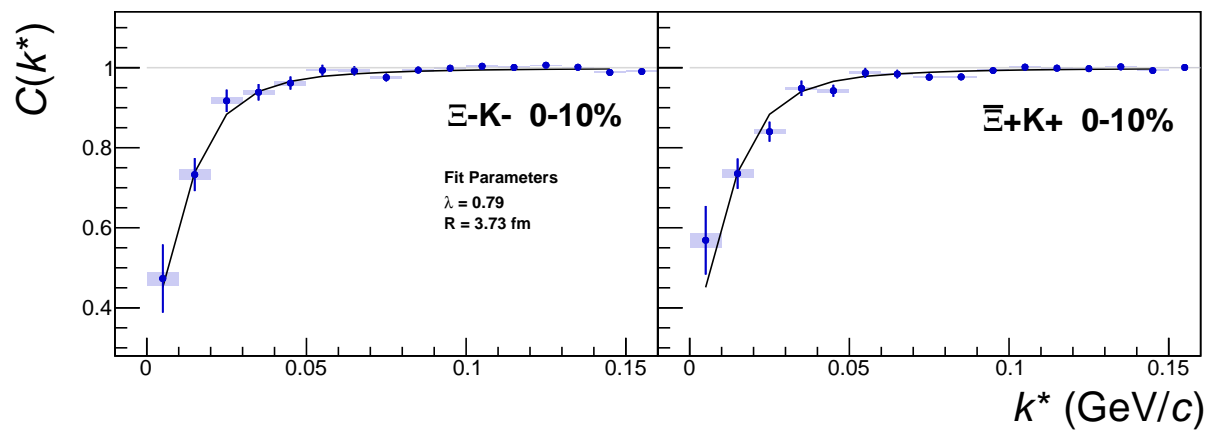


Fig. 60: $\Xi^- K^-$ Coulomb-only fit for 0-10% centrality

868 9 Additional Figures

869 9.1 Residuals

870 9.1.1 ΛK^+ Residuals

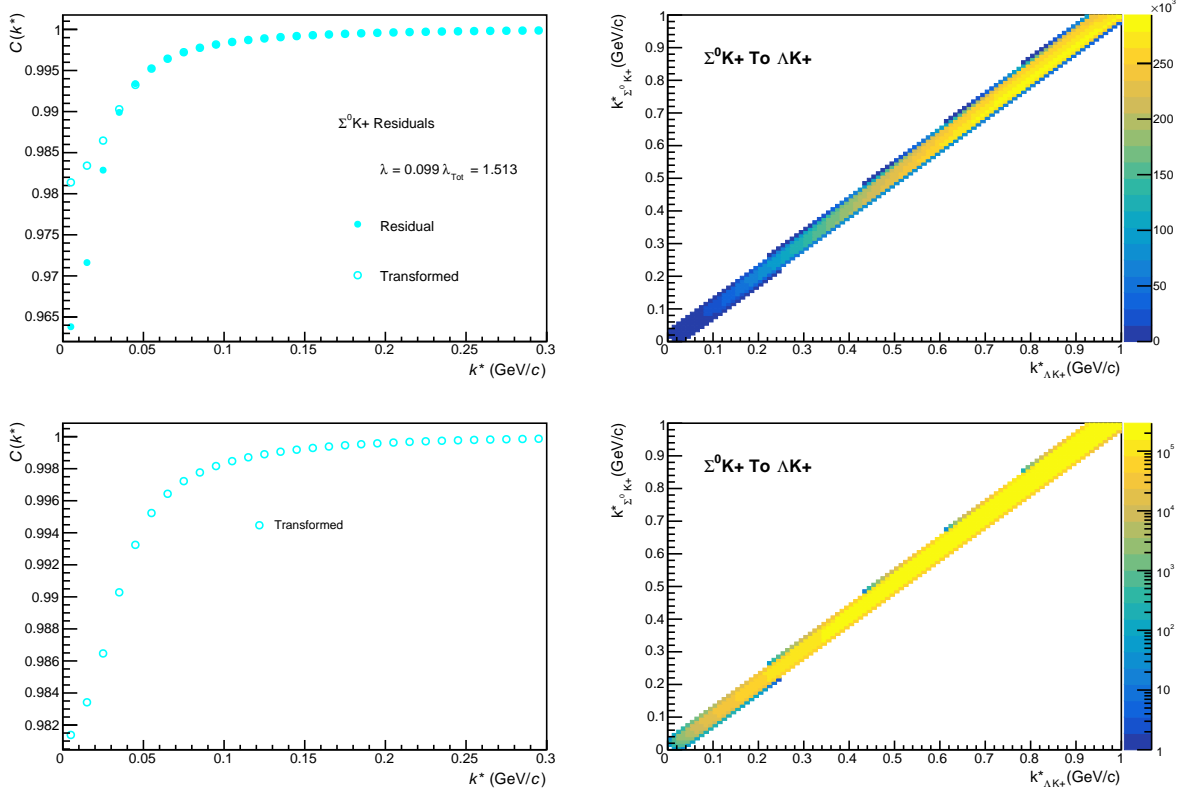


Fig. 61: Residuals: $\Sigma^0 K^+$ to ΛK^+ (0-10% Centrality)

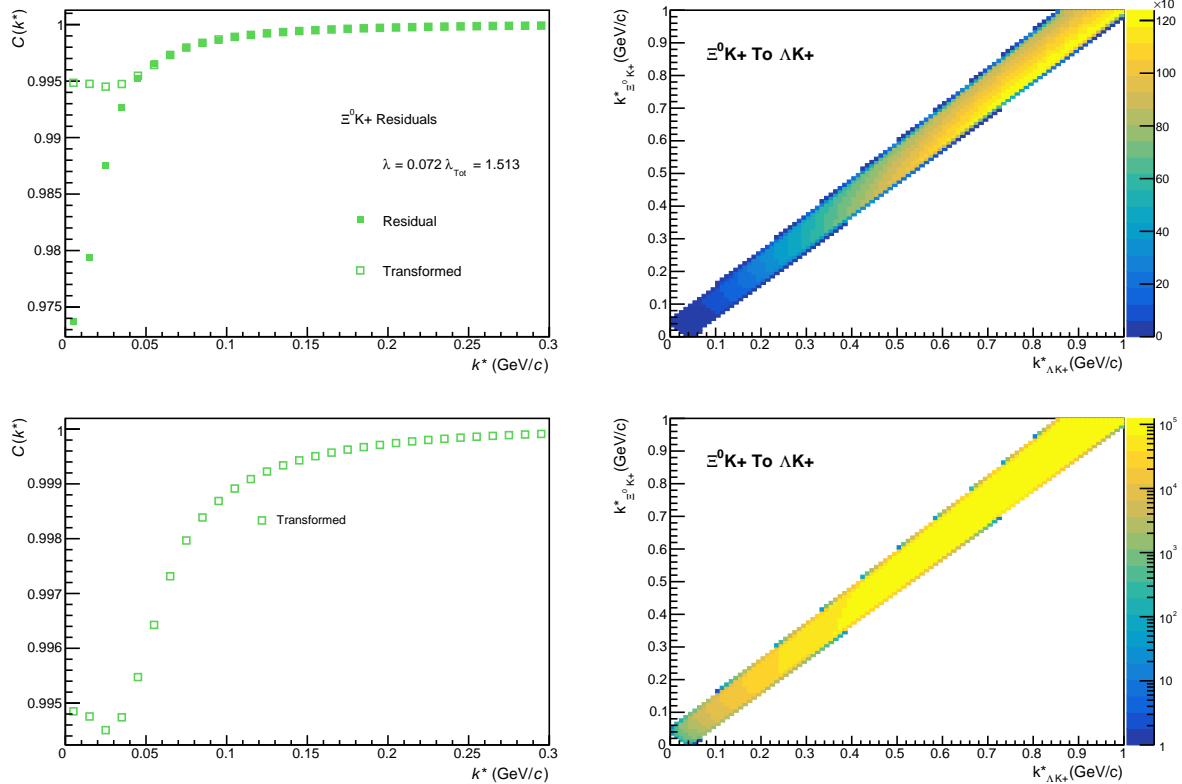


Fig. 62: Residuals: $\Xi^0 \text{K}^+$ to ΛK^+ (0-10% Centrality)

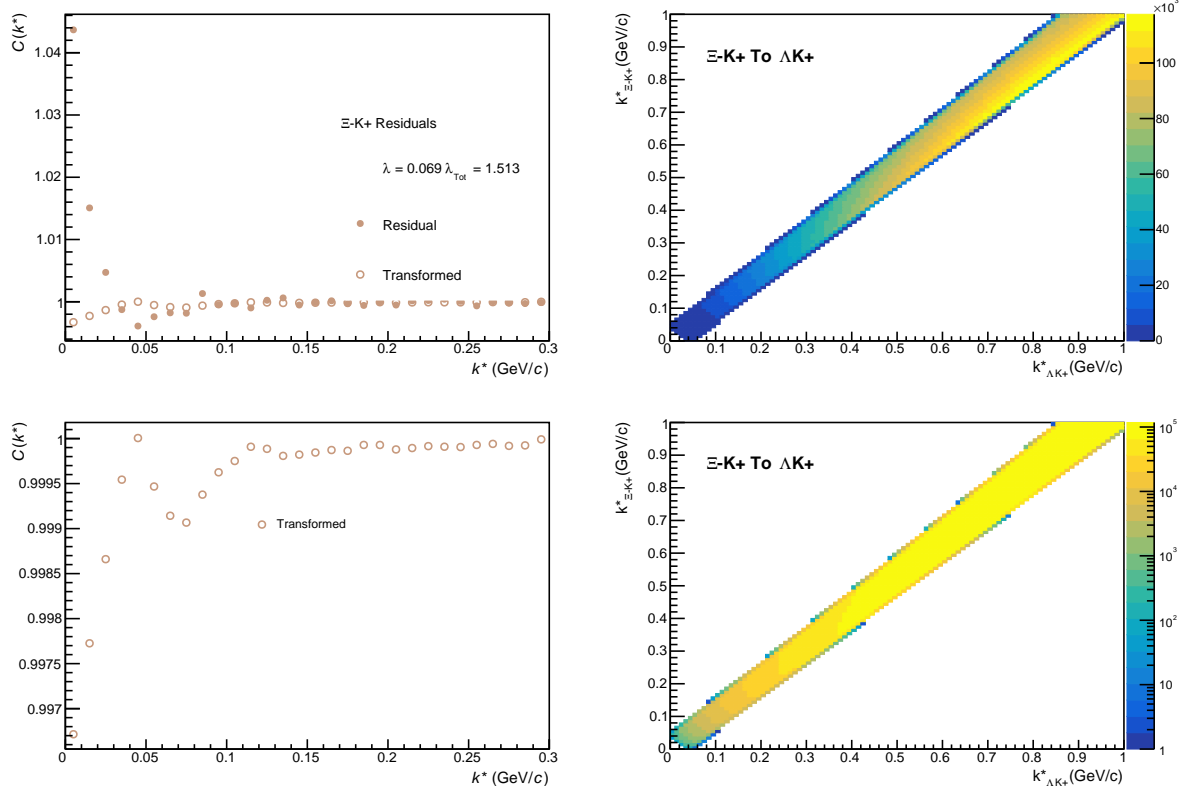
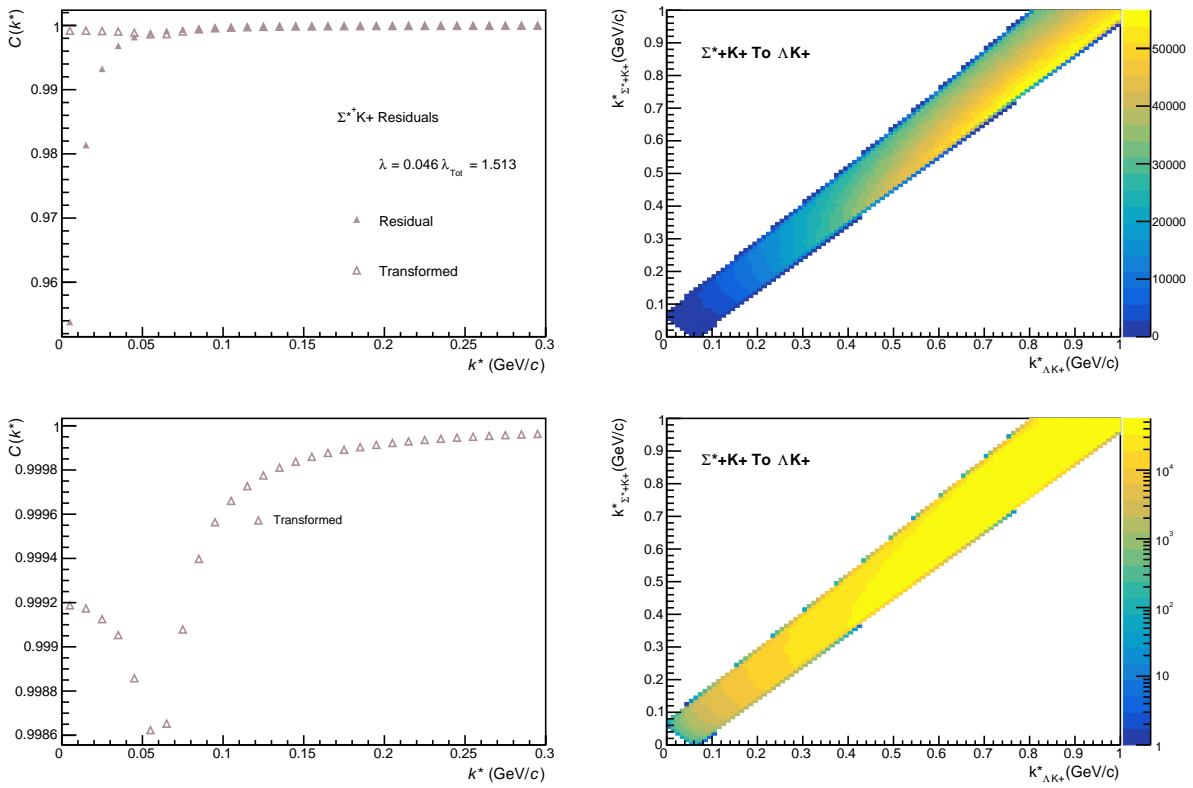
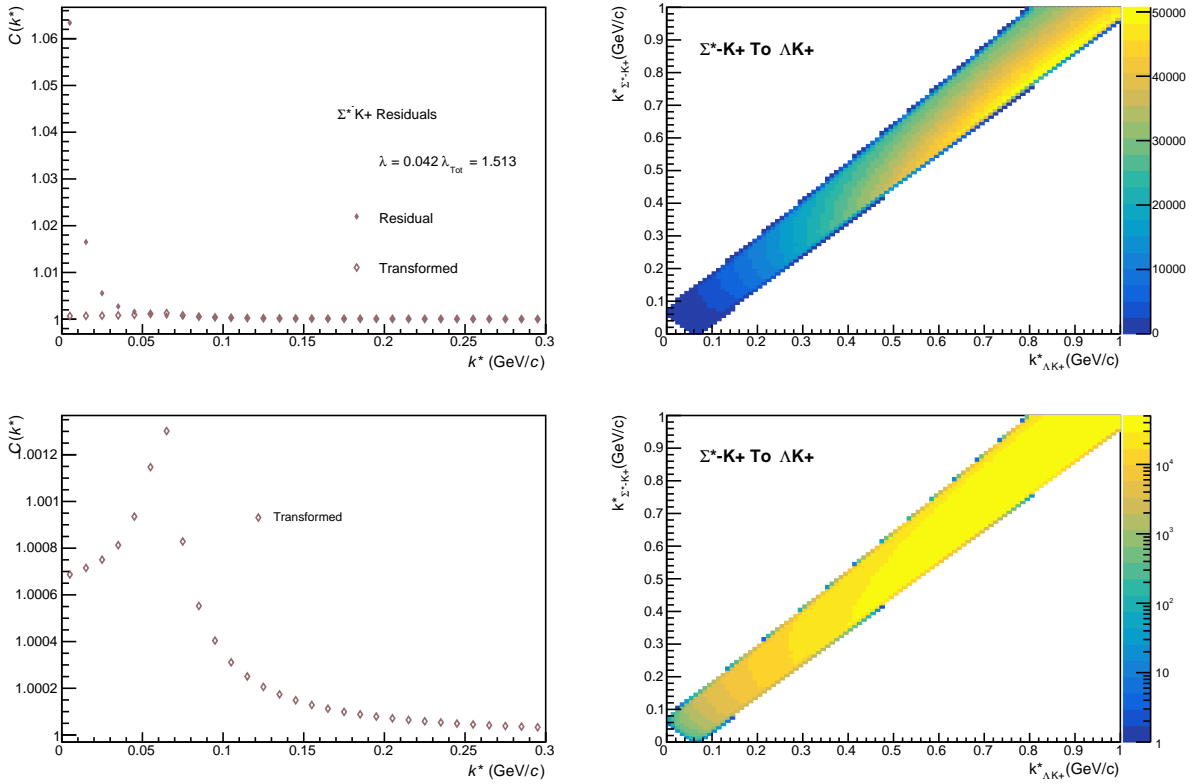


Fig. 63: Residuals: $\Xi^- \text{K}^+$ to ΛK^+ (0-10% Centrality)


 Fig. 64: Residuals: $\Sigma^{*+}K^+$ to ΛK^+ (0-10% Centrality)

 Fig. 65: Residuals: $\Sigma^{*-}K^+$ to ΛK^+ (0-10% Centrality)

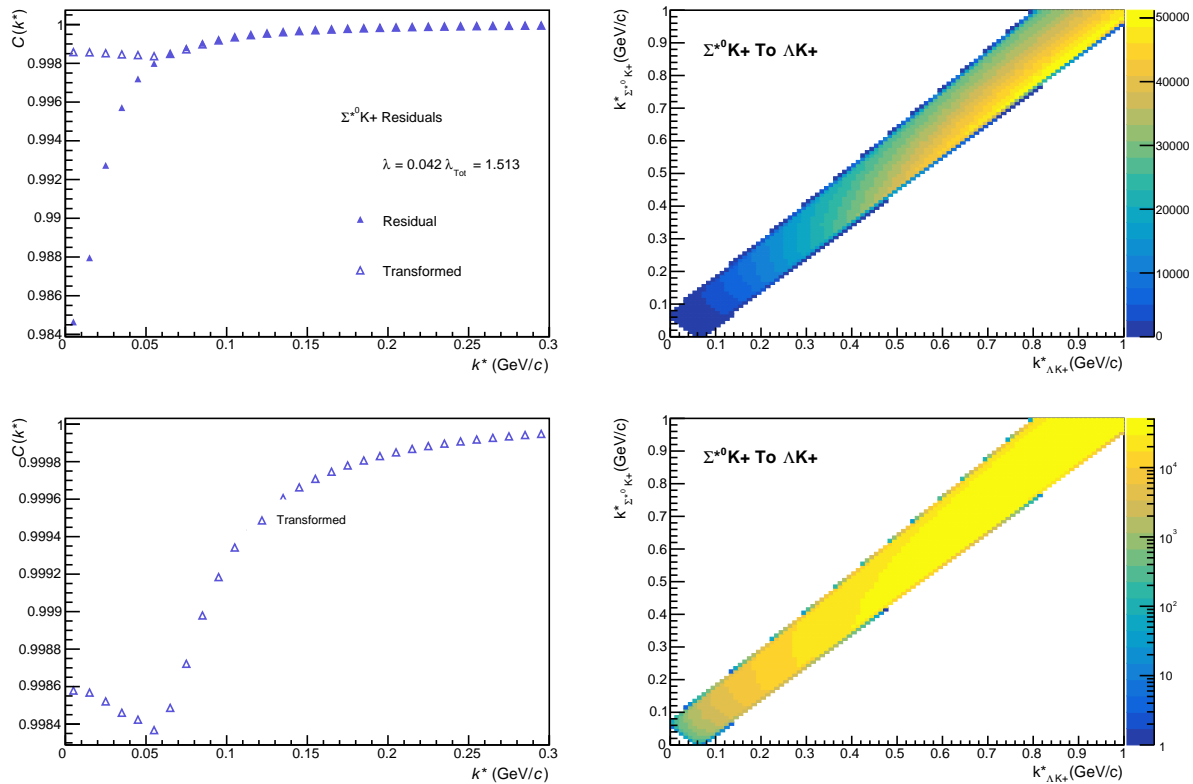


Fig. 66: Residuals: $\Sigma^{*0} \text{K}^+$ to ΛK^+ (0-10% Centrality)

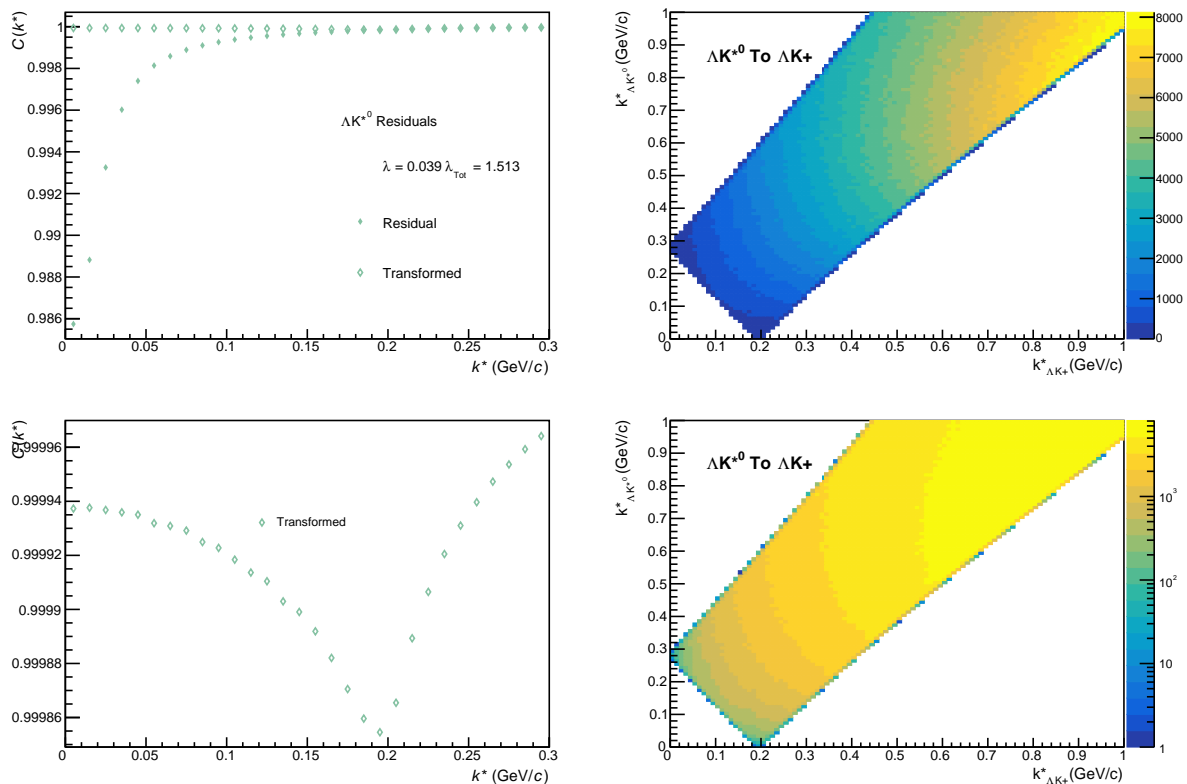


Fig. 67: Residuals: ΛK^{*0} to ΛK^+ (0-10% Centrality)

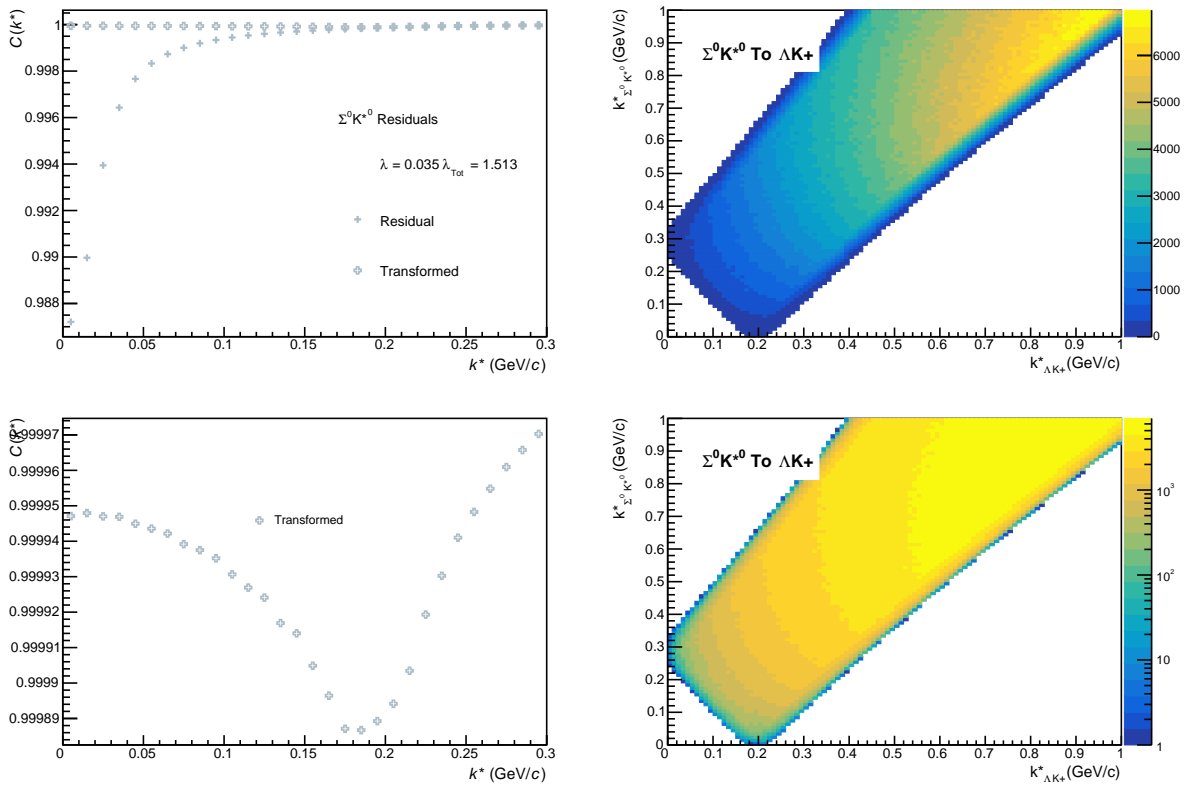


Fig. 68: Residuals: $\Sigma^0 K^{*0}$ to ΛK^+ (0-10% Centrality)

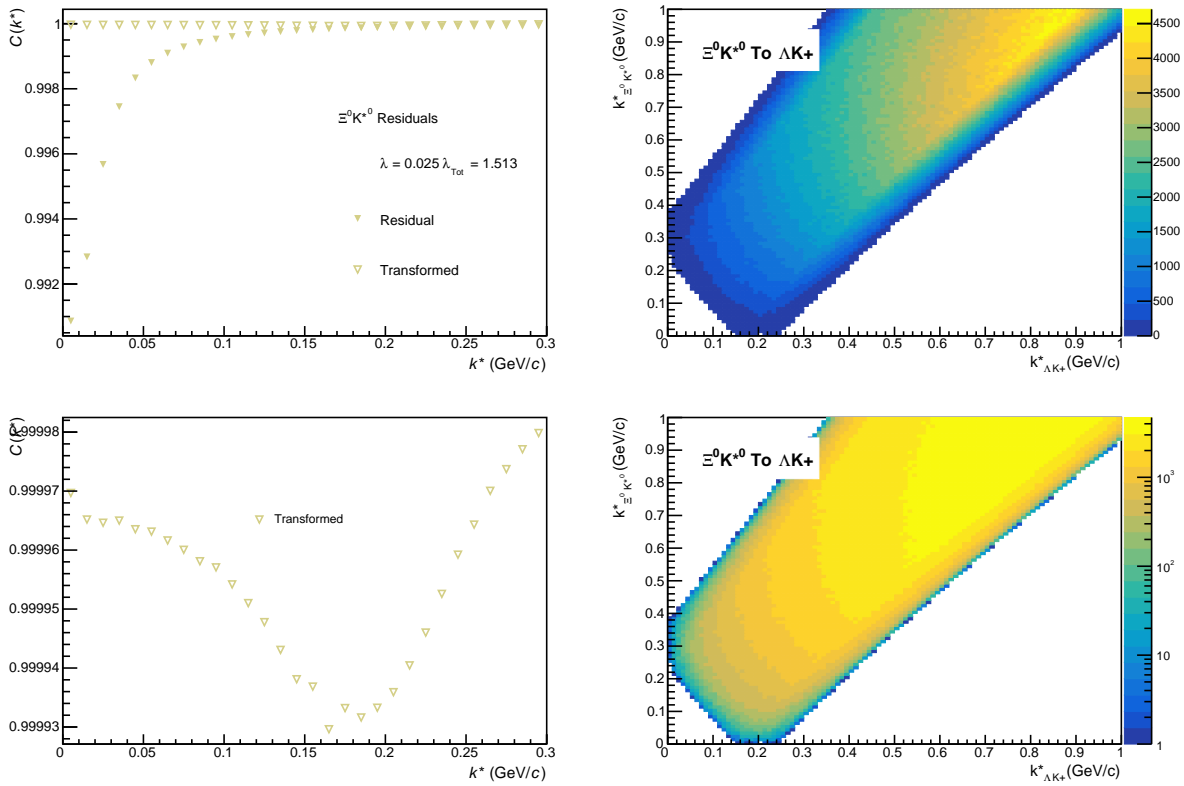


Fig. 69: Residuals: $\Xi^0 K^{*0}$ to ΛK^+ (0-10% Centrality)

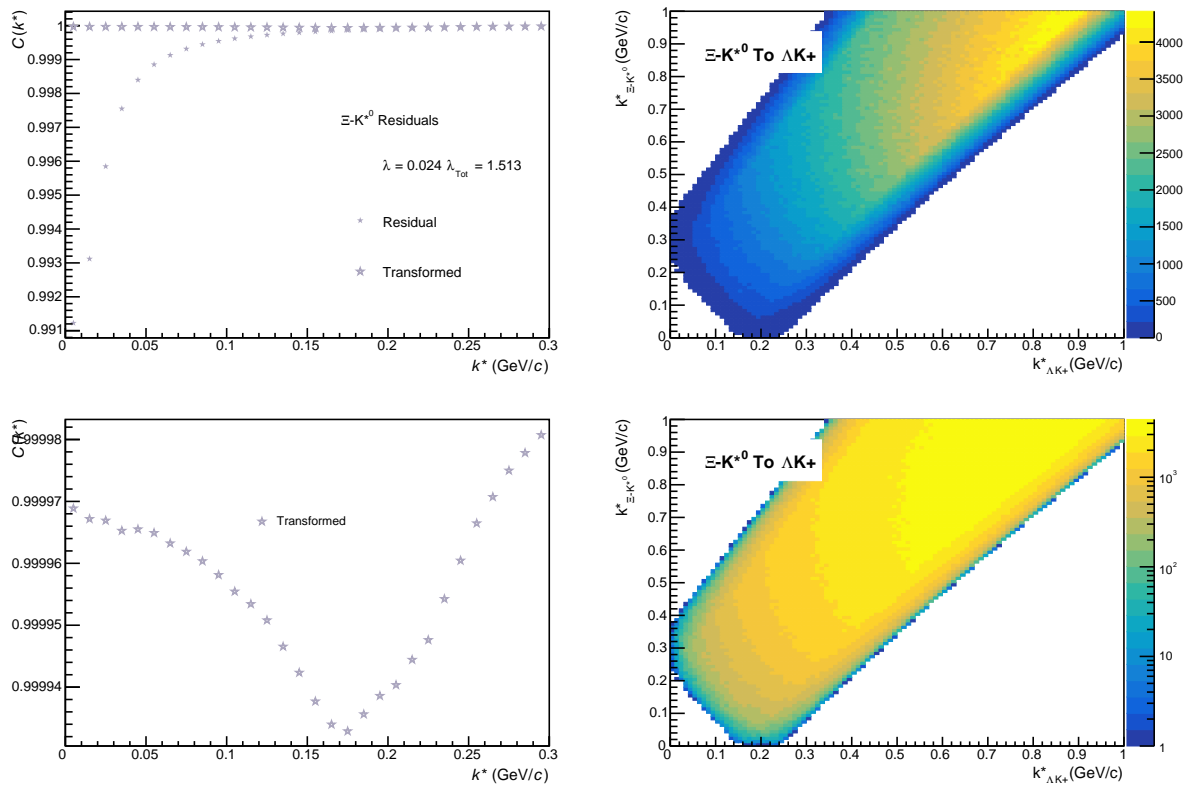
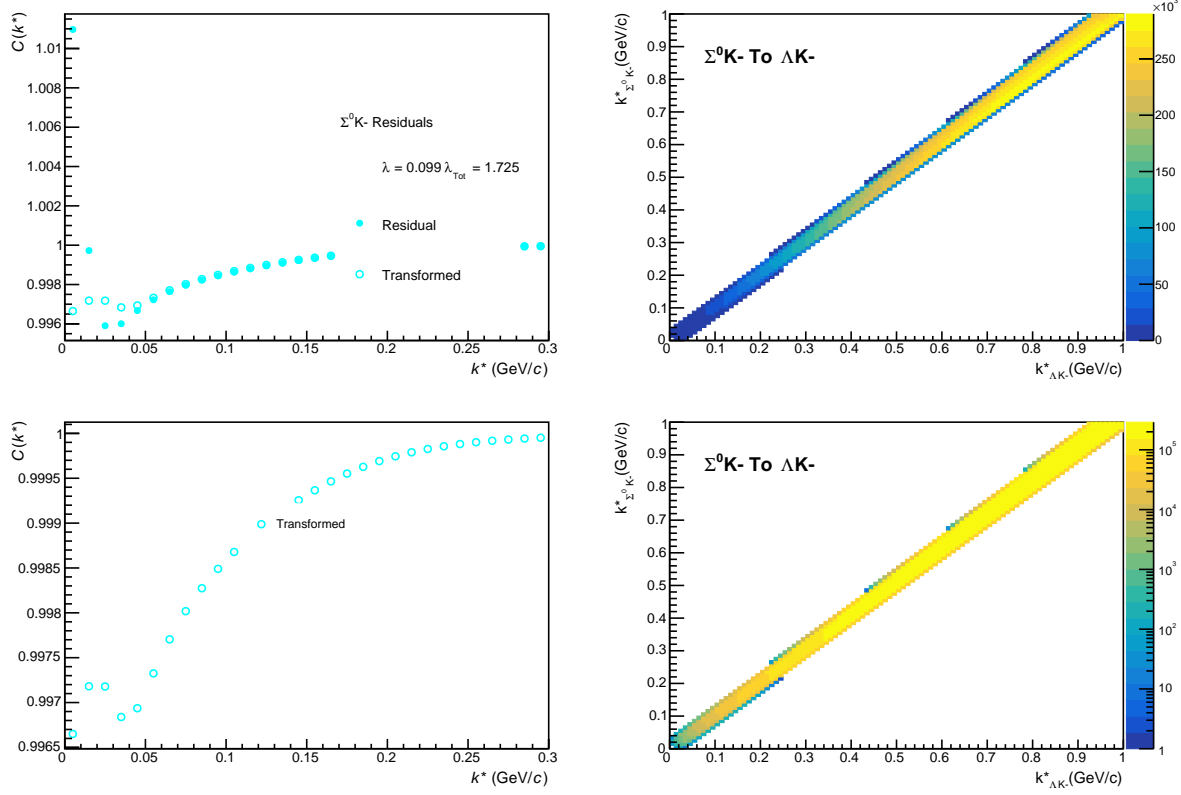


Fig. 70: Residuals: Ξ^-K^{*0} to ΛK^+ (0-10% Centrality)

871 **9.1.2 ΛK^- Residuals****Fig. 71:** Residuals: $\Sigma^0 K^-$ to ΛK^- (0-10% Centrality)

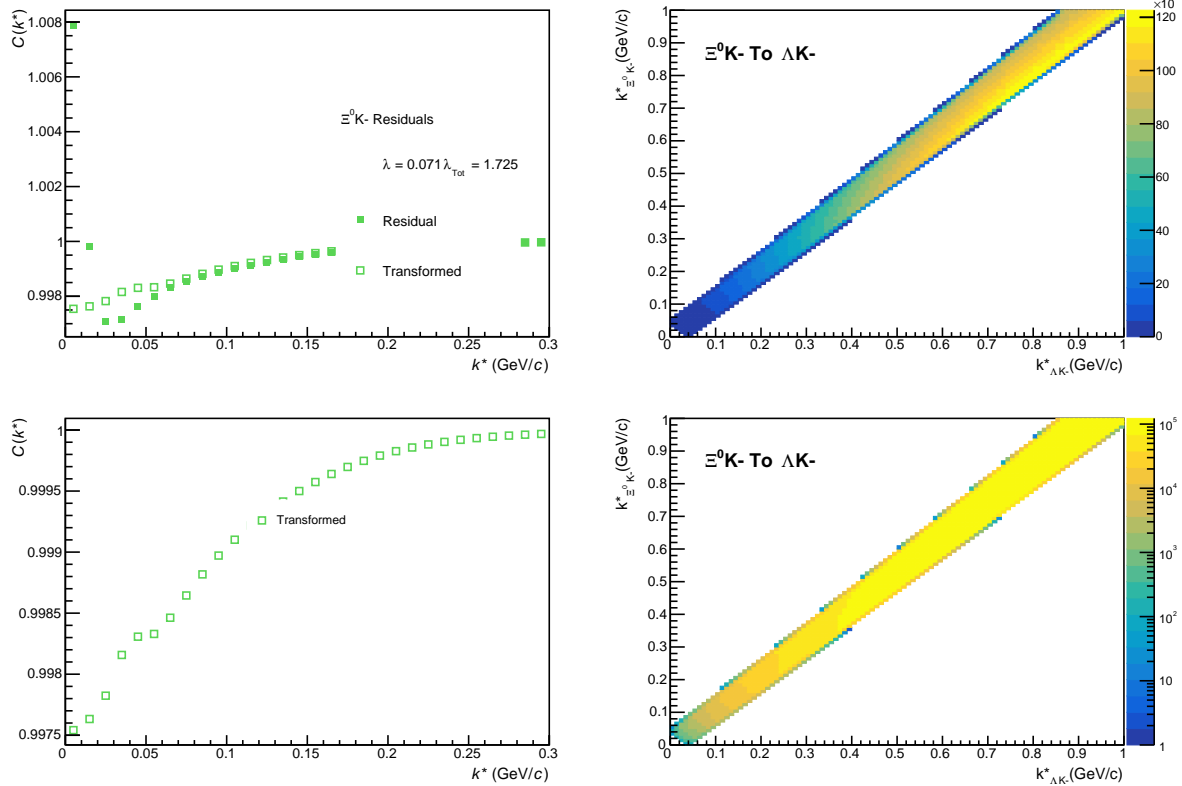


Fig. 72: Residuals: $\Xi^0 \text{K}^-$ to ΛK^- (0-10% Centrality)

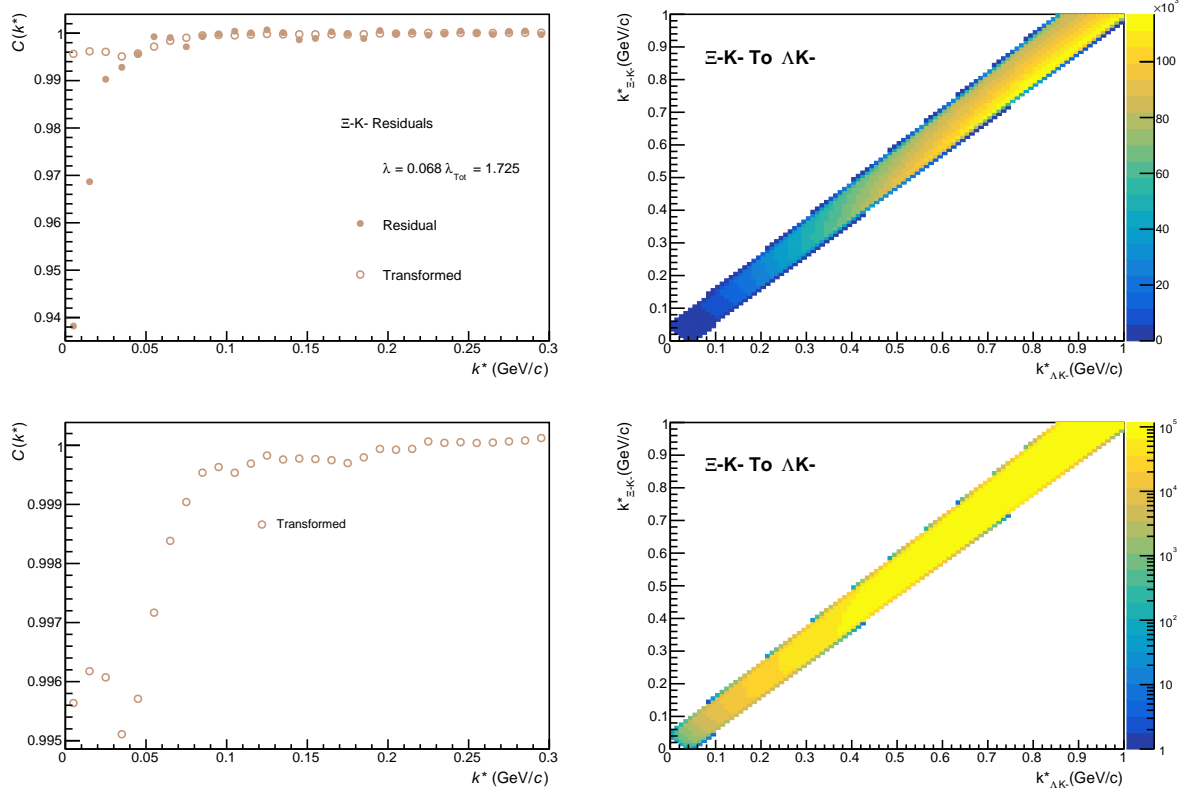
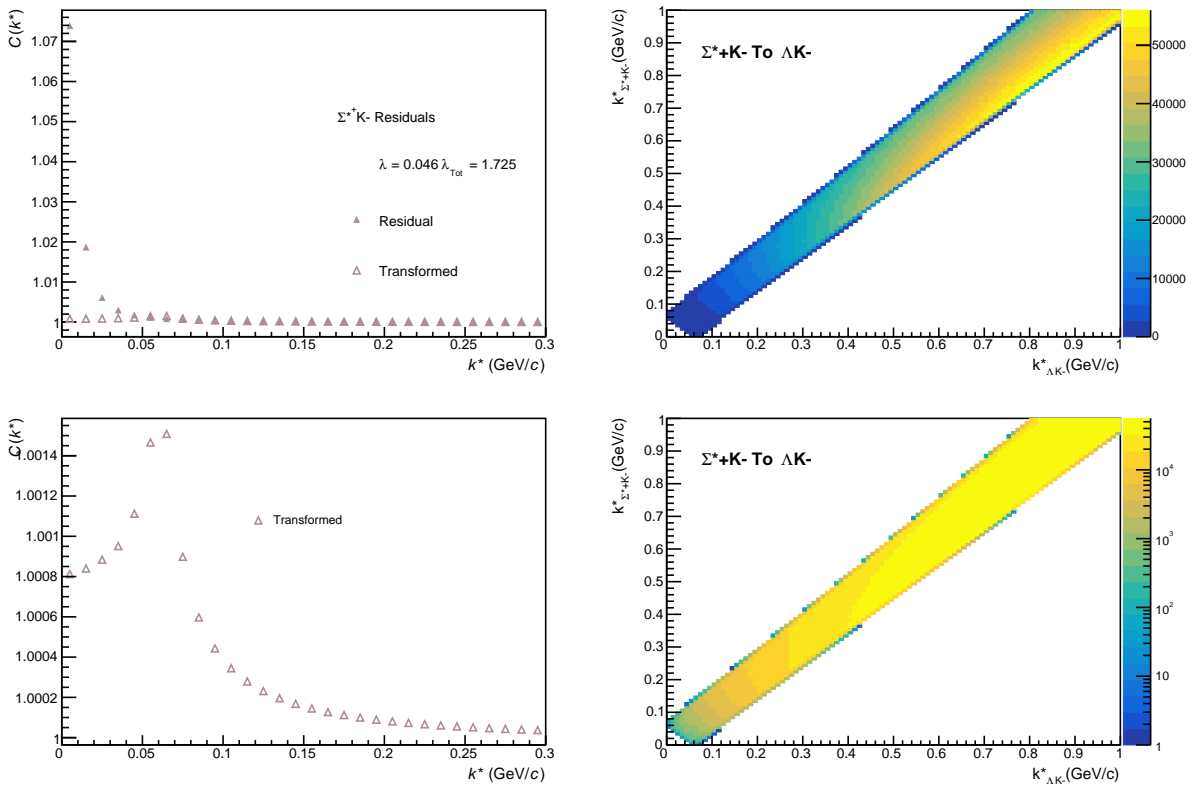
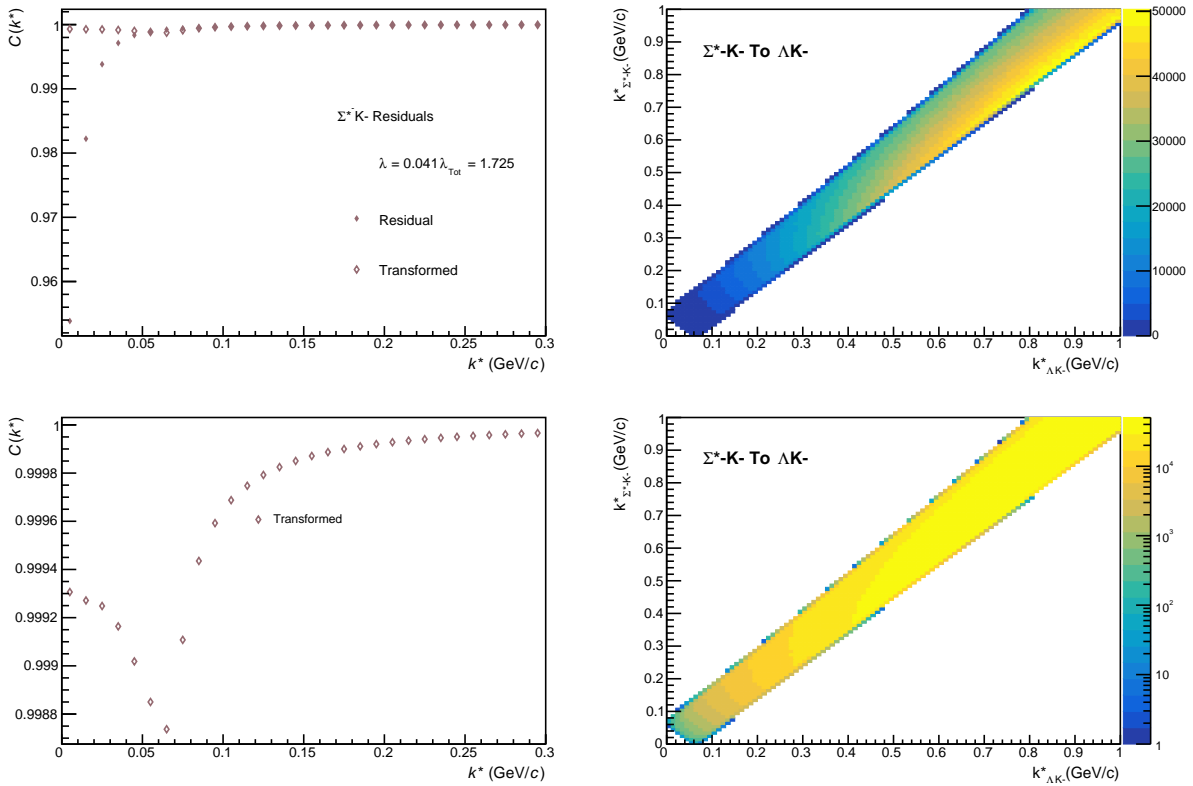


Fig. 73: Residuals: $\Xi^- \text{K}^-$ to ΛK^- (0-10% Centrality)


Fig. 74: Residuals: $\Sigma^{+} K^{-}$ to ΛK^{-} (0-10% Centrality)

Fig. 75: Residuals: $\Sigma^- K^-$ to ΛK^- (0-10% Centrality)

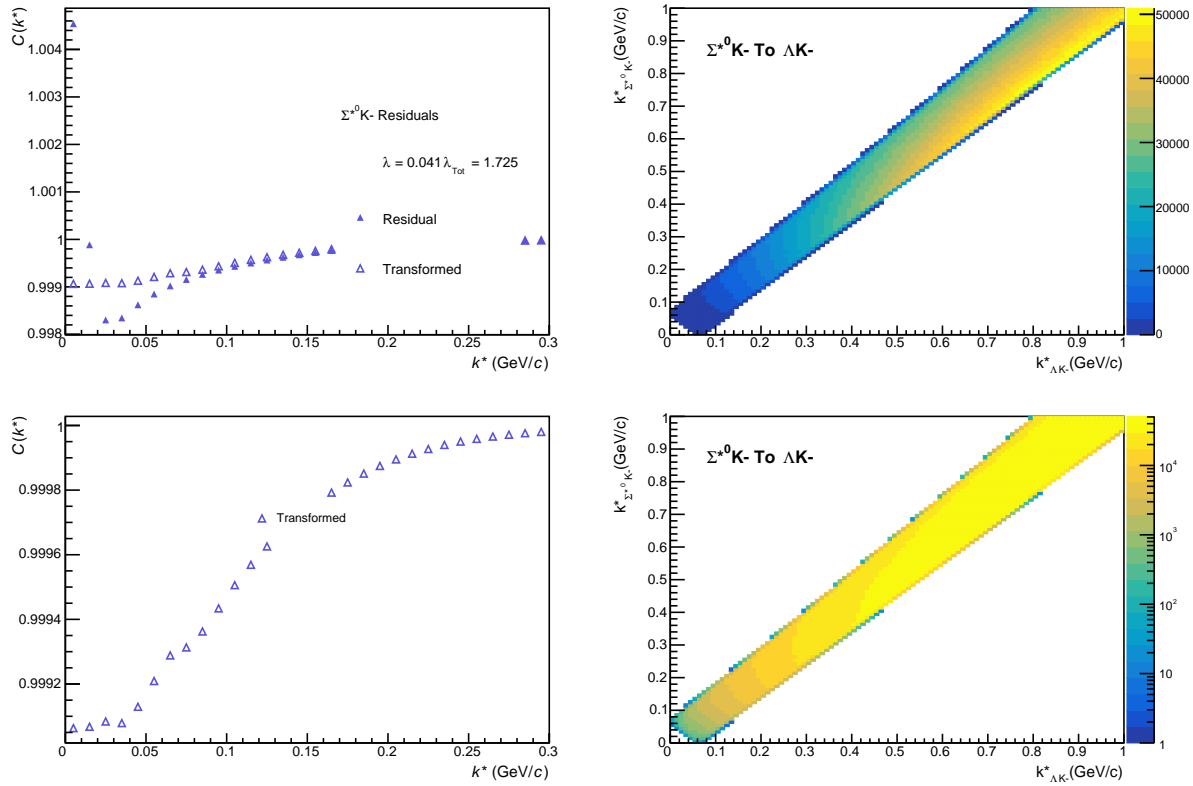


Fig. 76: Residuals: $\Sigma^0 \text{K}^-$ to ΛK^- (0-10% Centrality)

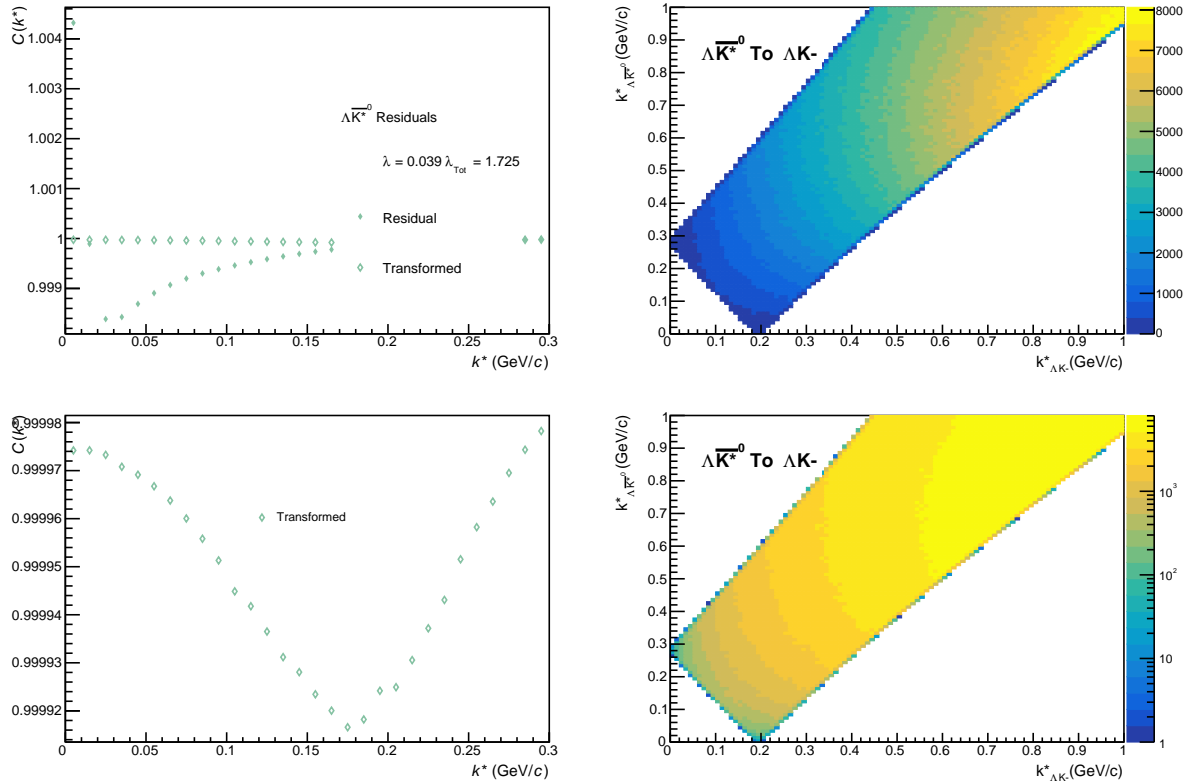


Fig. 77: Residuals: $\Lambda \bar{K}^0$ to ΛK^- (0-10% Centrality)

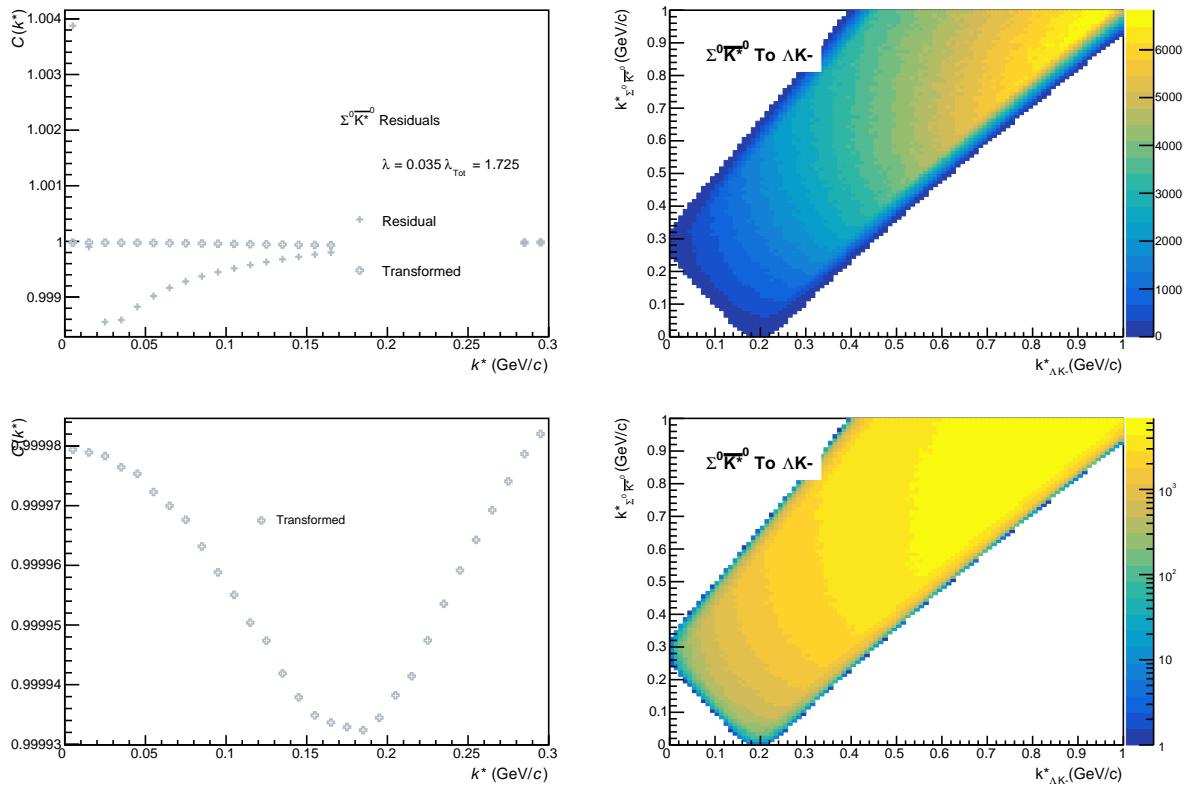


Fig. 78: Residuals: $\Sigma^0 \bar{K}^{*0}$ to ΛK^- (0-10% Centrality)

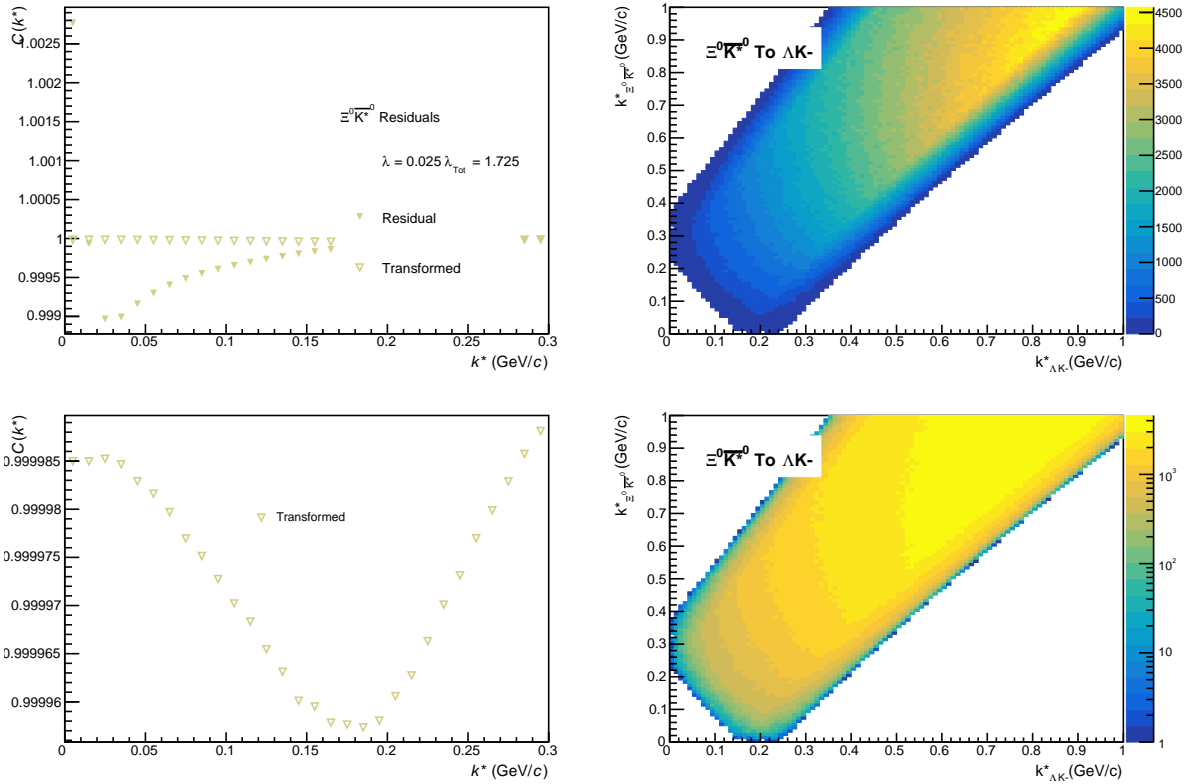


Fig. 79: Residuals: $\Xi^0 \bar{K}^{*0}$ to ΛK^- (0-10% Centrality)

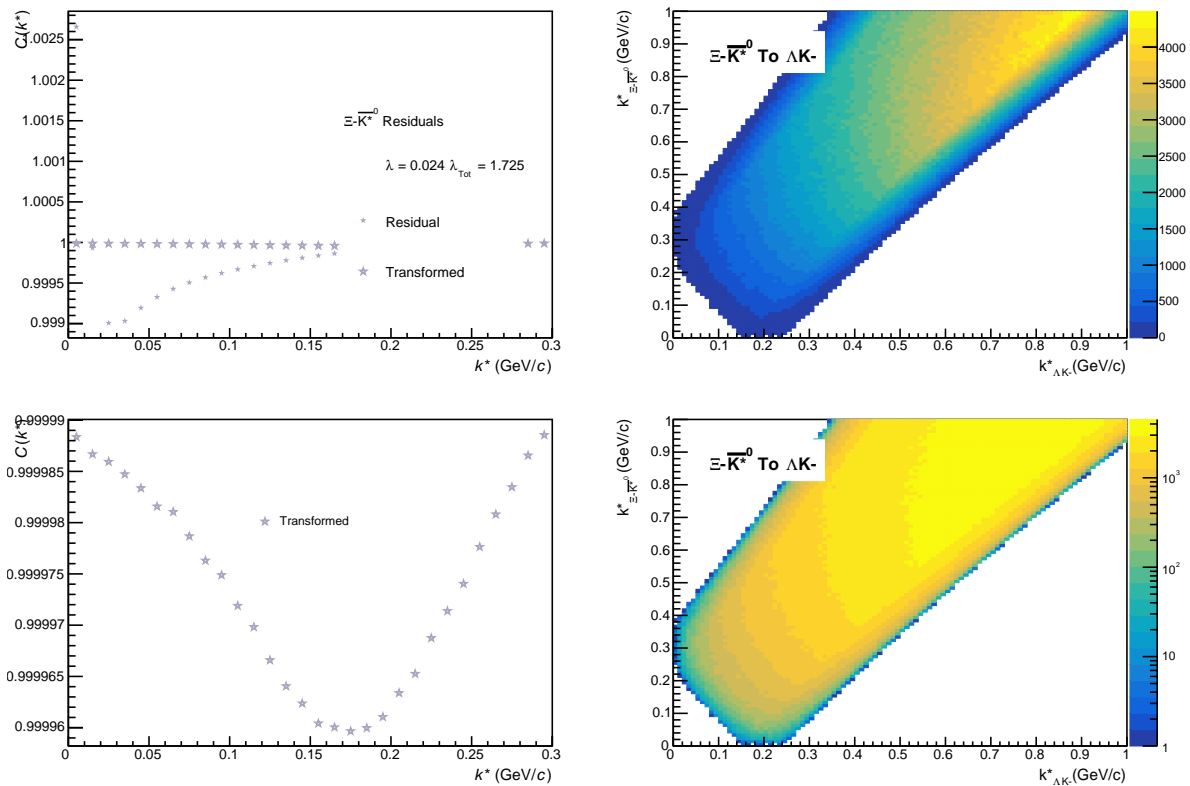
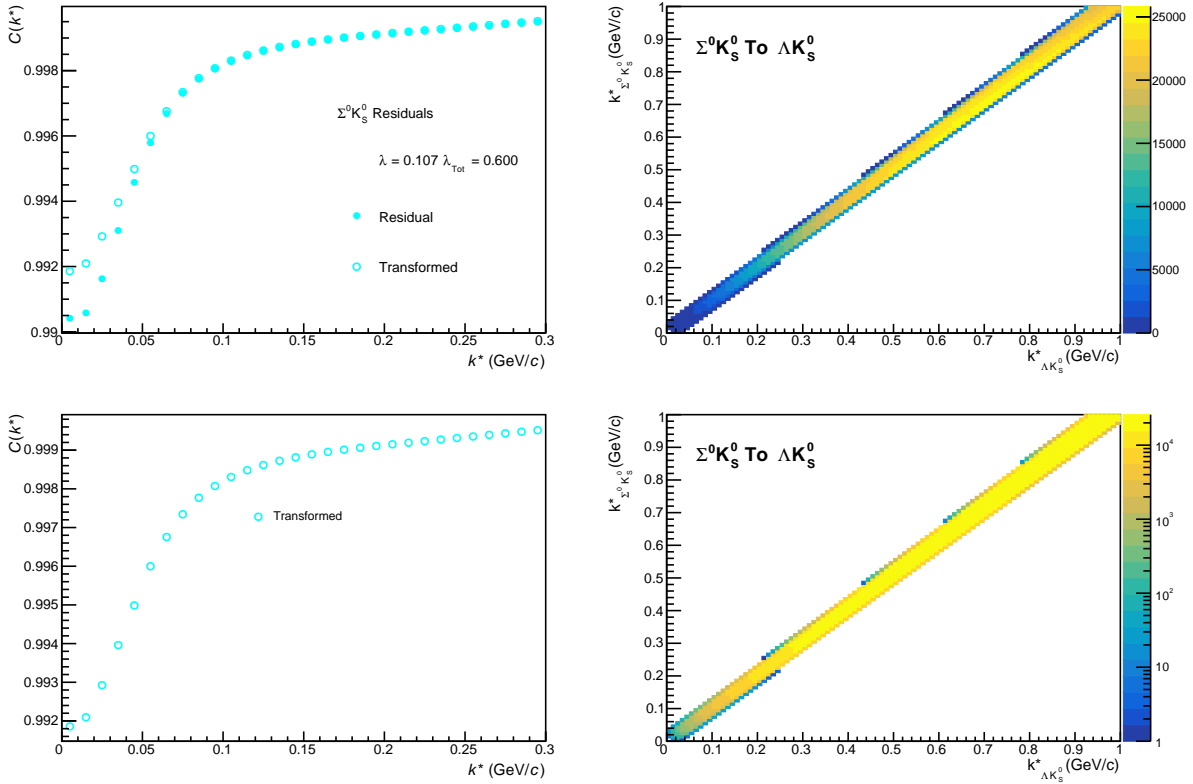


Fig. 80: Residuals: $\Xi^- \bar{K}^{*0}$ to ΛK^- (0-10% Centrality)

872 **9.1.3 ΛK_S^0 Residuals****Fig. 81:** Residuals: $\Sigma^0 K_S^0$ to ΛK_S^0 (0-10% Centrality)

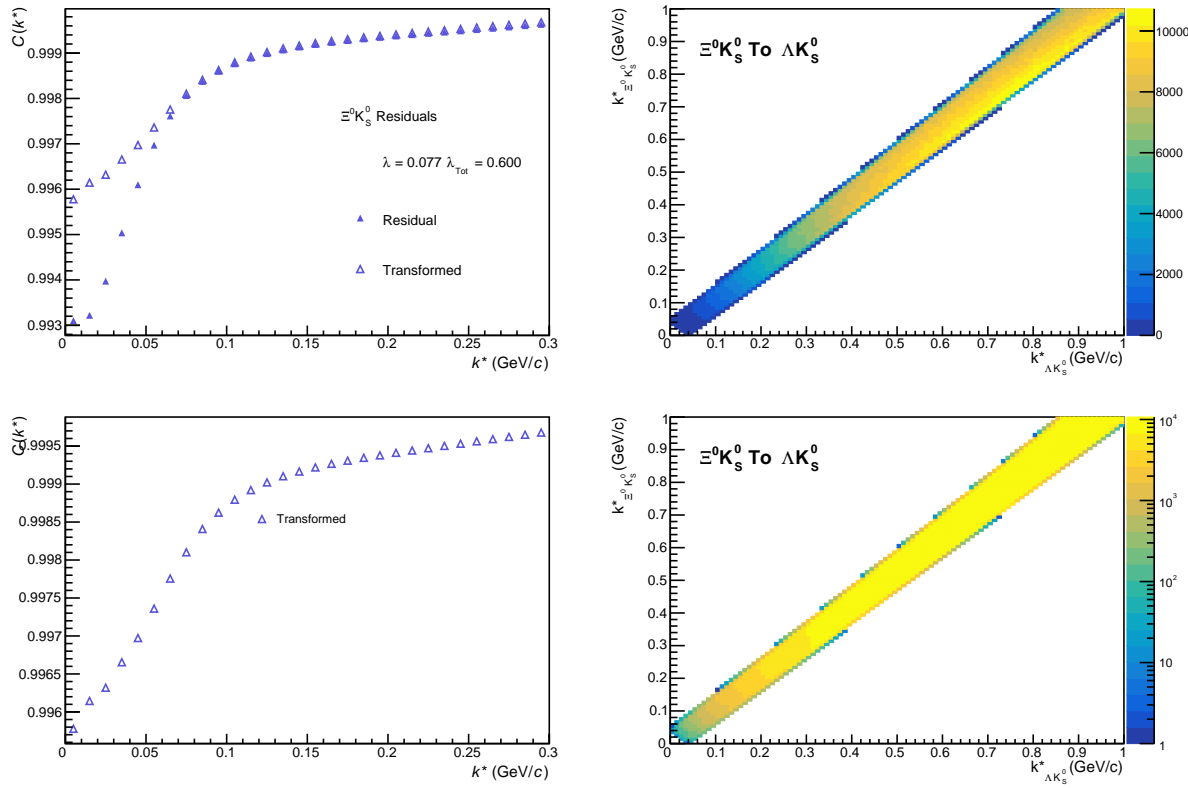


Fig. 82: Residuals: $\Xi^0 K_s^0$ to ΛK_s^0 (0-10% Centrality)

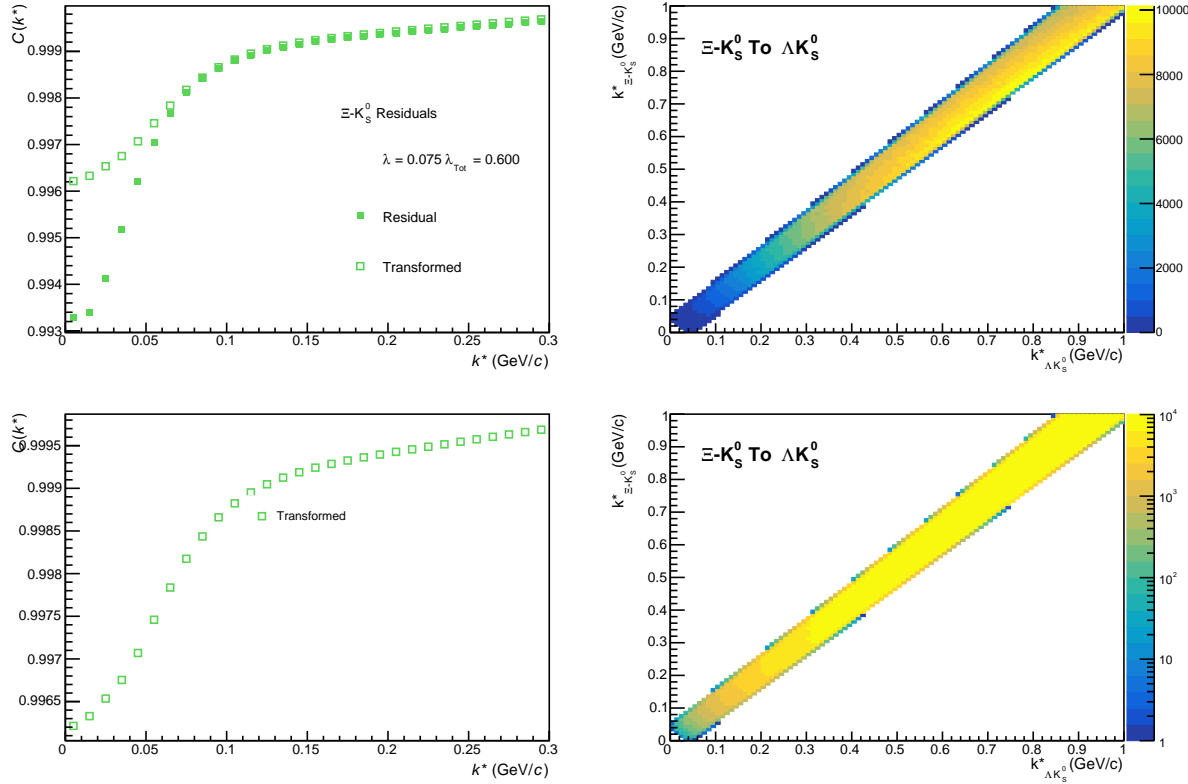
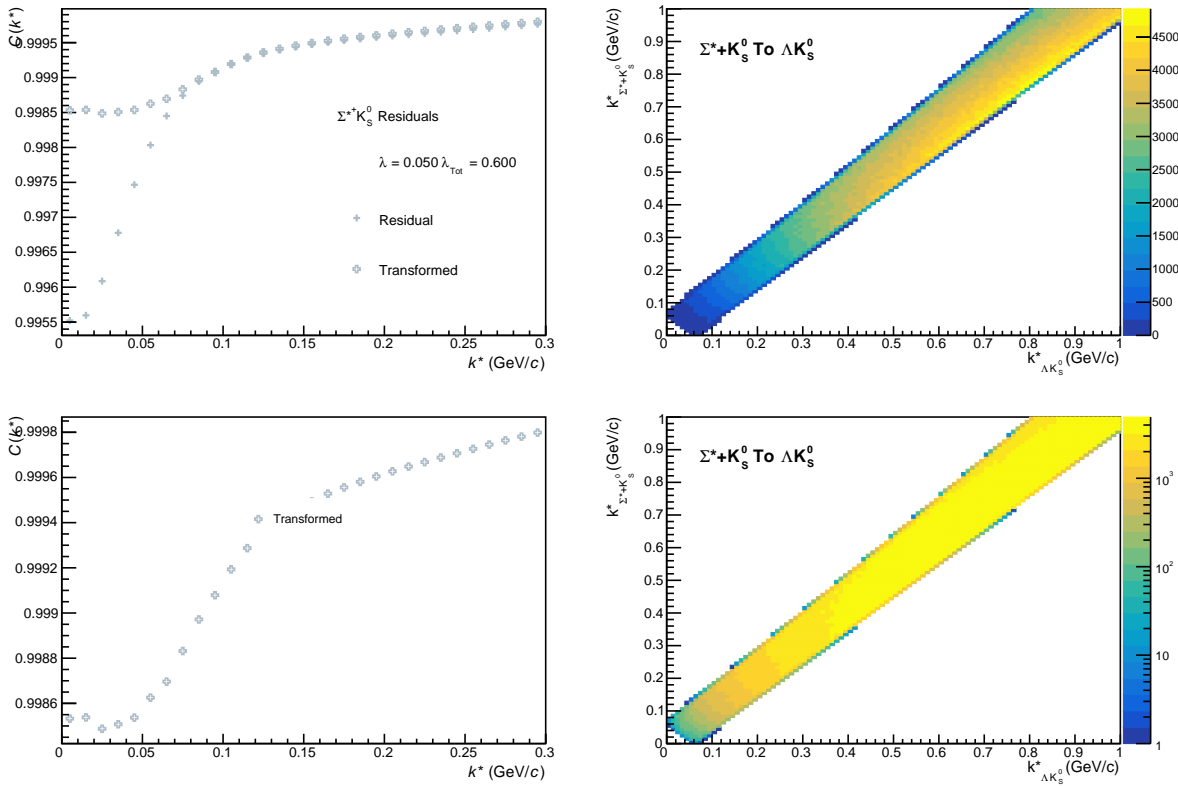
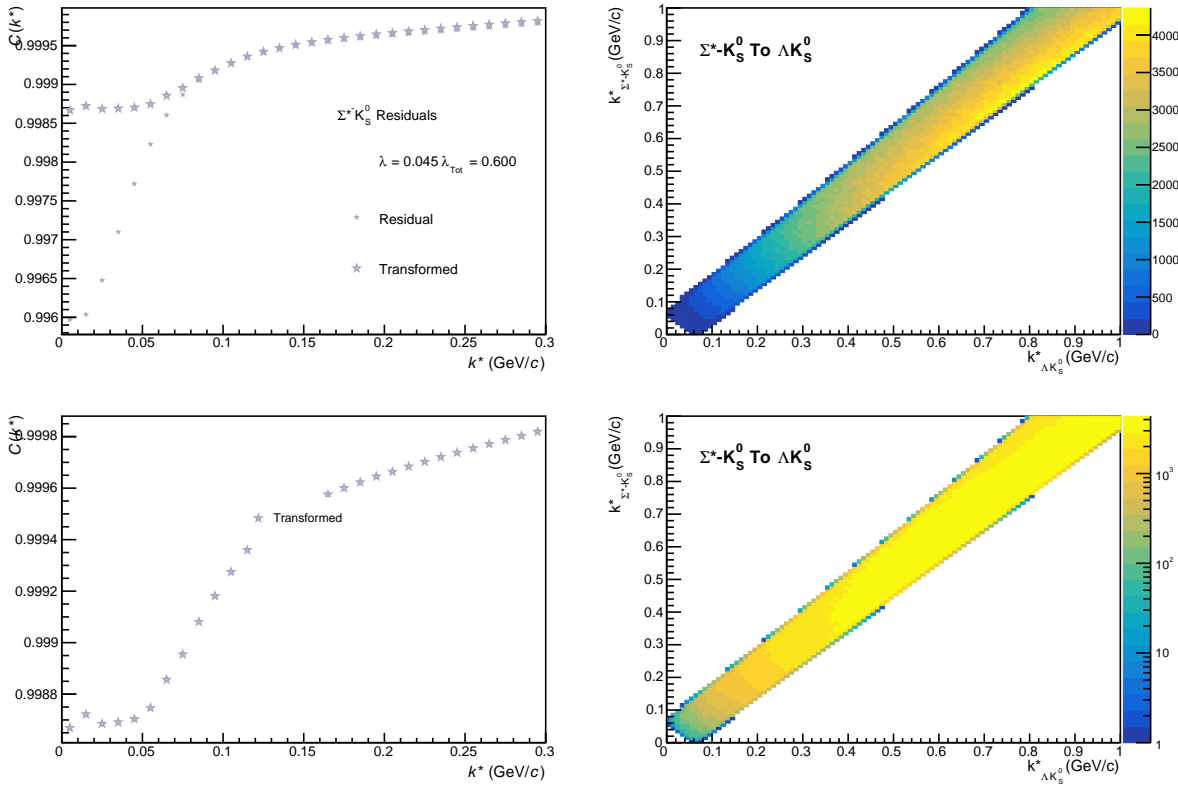


Fig. 83: Residuals: $\Xi^- K_s^0$ to ΛK_s^0 (0-10% Centrality)


Fig. 84: Residuals: $\Sigma^* + K_S^0$ to ΛK_S^0 (0-10% Centrality)

Fig. 85: Residuals: $\Sigma^* - K_S^0$ to ΛK_S^0 (0-10% Centrality)

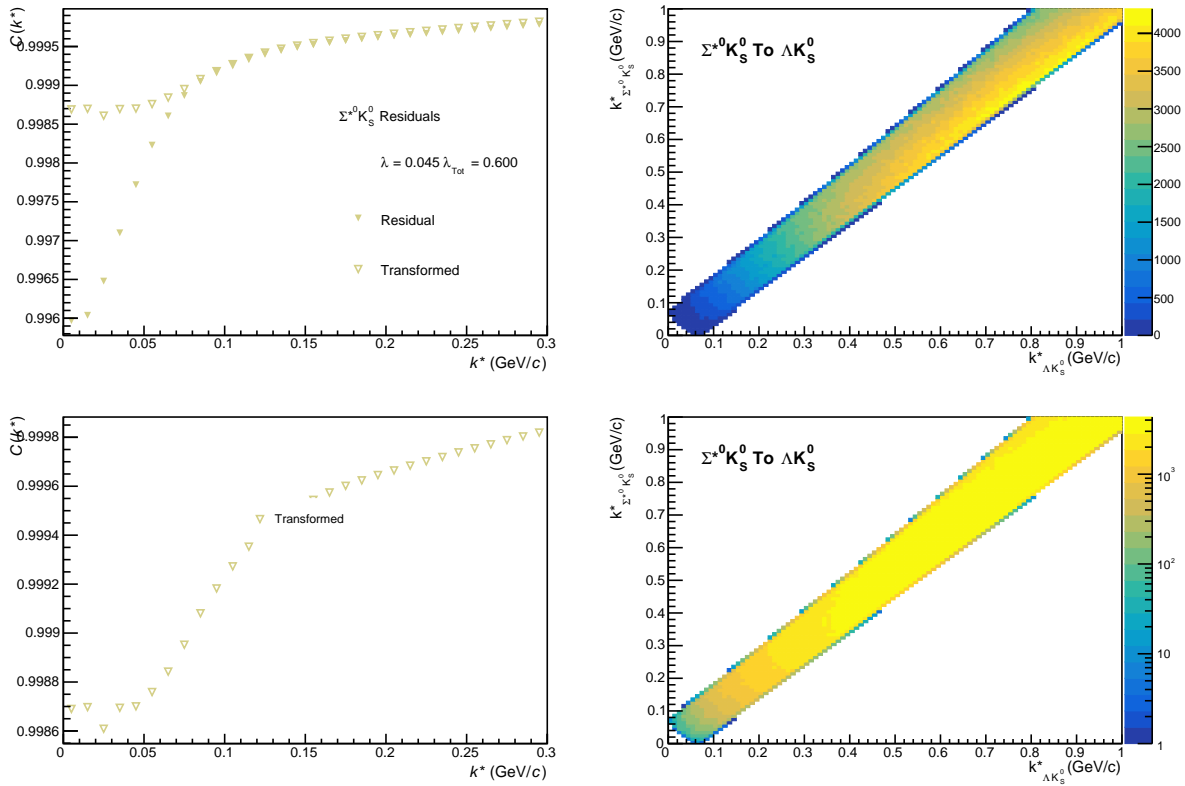


Fig. 86: Residuals: $\Sigma^{*0} K_S^0$ to ΛK_S^0 (0-10% Centrality)

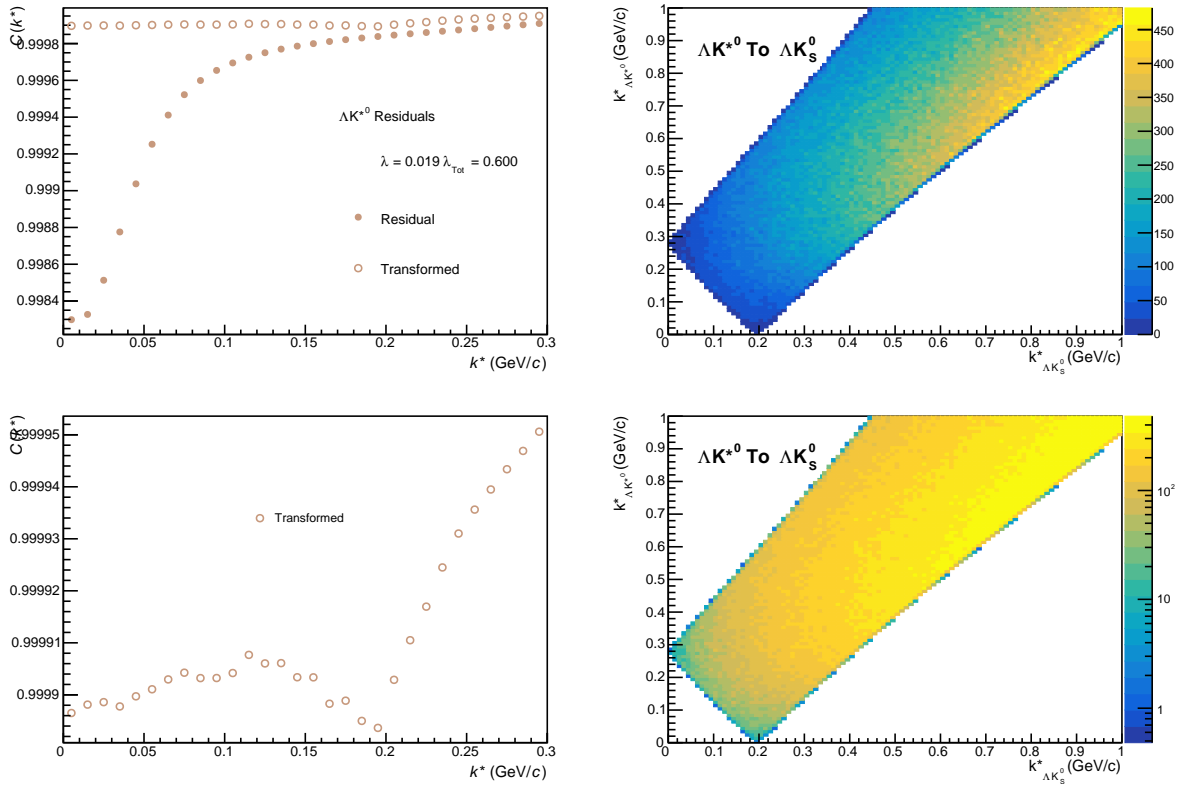
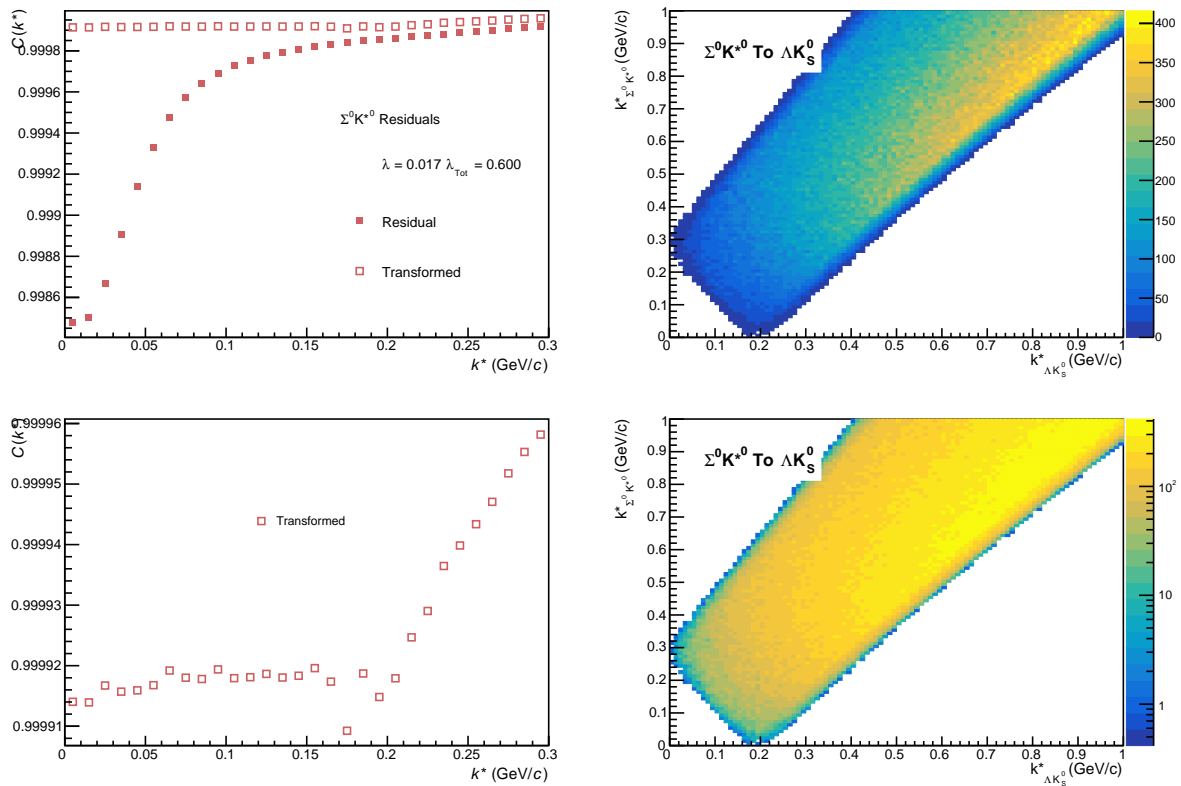
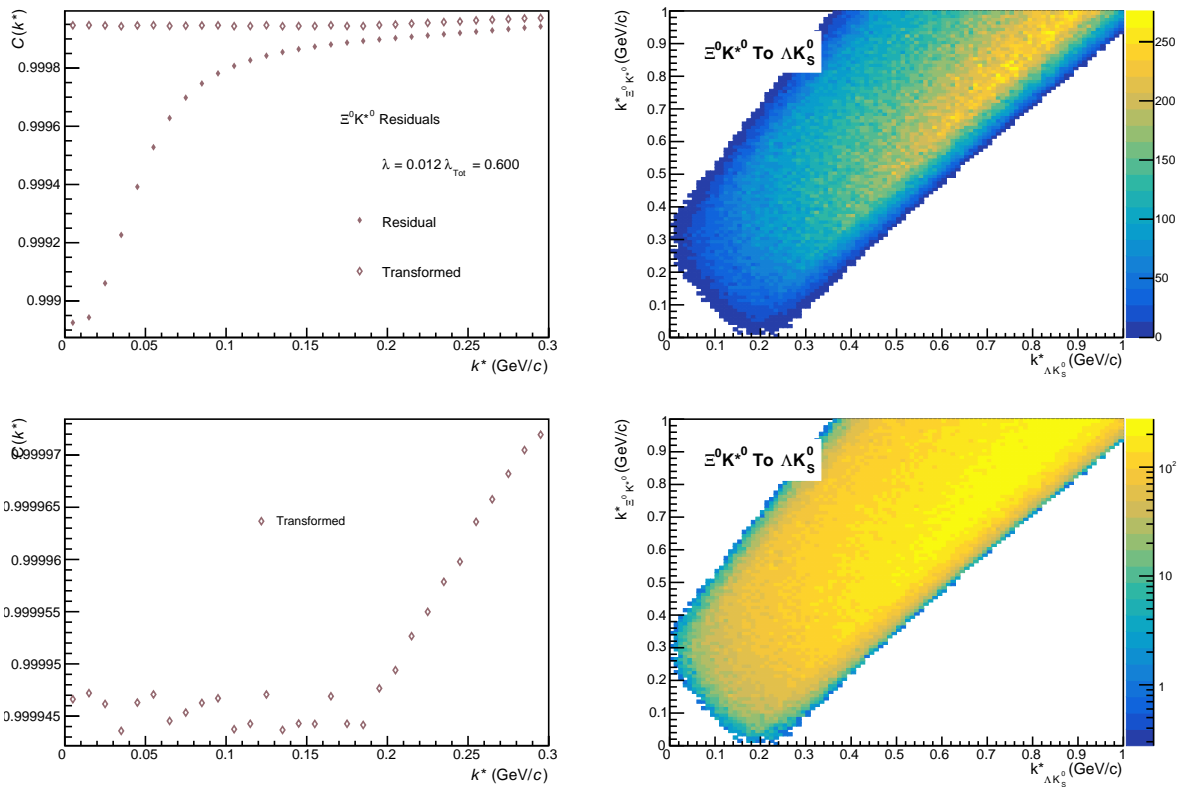


Fig. 87: Residuals: ΔK^{*0} to ΛK_S^0 (0-10% Centrality)


Fig. 88: Residuals: $\Sigma^0 K^{*0}$ to ΛK_S^0 (0-10% Centrality)

Fig. 89: Residuals: $\Xi^0 K^{*0}$ to ΛK_S^0 (0-10% Centrality)

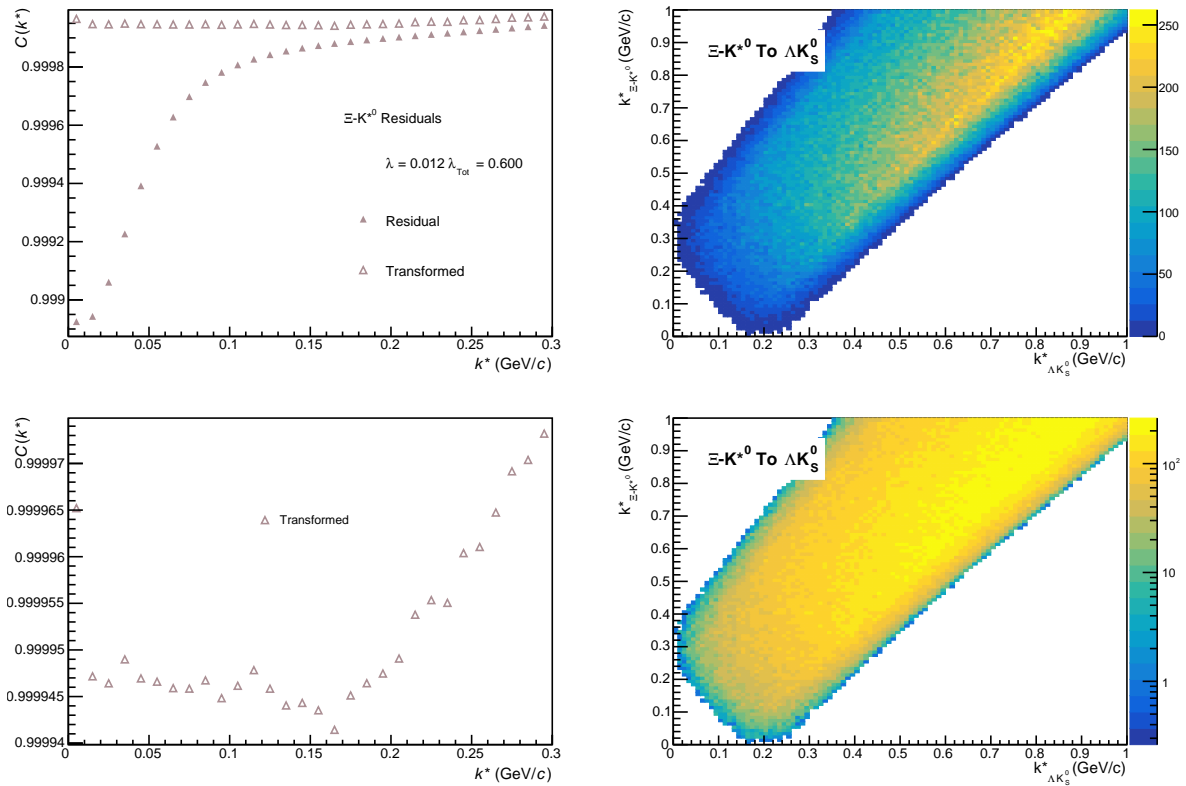


Fig. 90: Residuals: $\Xi^- K^{*0}$ to ΛK_S^0 (0-10% Centrality)

References

- [1] R. Lednický and V. L. Lyuboshitz. *Sov. J. Nucl. Phys.*, 35:770, 1982.
- [2] Michael Annan Lisa, Scott Pratt, Ron Soltz, and Urs Wiedemann. Femtoscopy in relativistic heavy ion collisions. *Ann. Rev. Nucl. Part. Sci.*, 55:357–402, 2005.
- [3] S. E. Koonin. Proton Pictures of High-Energy Nuclear Collisions. *Phys. Lett.*, B70:43–47, 1977.
- [4] S. Pratt, T. Csorgo, and J. Zimányi. Detailed predictions for two pion correlations in ultrarelativistic heavy ion collisions. *Phys. Rev.*, C42:2646–2652, 1990.
- [5] Richard Lednický. Finite-size effects on two-particle production in continuous and discrete spectrum. *Phys. Part. Nucl.*, 40:307–352, 2009.
- [6] Adam Kisiel, Hanna Zbroszczyk, and Maciej Szymaski. Extracting baryon-antibaryon strong interaction potentials from $p\bar{\Lambda}$ femtoscopic correlation functions. *Phys. Rev.*, C89(5):054916, 2014.
- [7] Jai Salzwedel and Thomas Humanic. Lambda femtoscopy in $\sqrt{s_{NN}} = 2.76$ TeV Pb-Pb collisions at ALICE, Jan 2017. Presented 15 Dec 2016.
- [8] A Kisiel. Non-identical particle correlation analysis in the presence of non-femtoscopic correlations. *Acta Physica Polonica B*, 48:717, 04 2017.
- [9] Yan-Rui Liu and Shi-Lin Zhu. Meson-baryon scattering lengths in HB chi PT. *Phys. Rev.*, D75:034003, 2007.
- [10] Maxim Mai, Peter C. Bruns, Bastian Kubis, and Ulf-G. Meißner. Aspects of meson-baryon scattering in three and two-flavor chiral perturbation theory. *Phys. Rev.*, D80:094006, 2009.
- [11] Jaroslav Adam et al. One-dimensional pion, kaon, and proton femtoscopy in Pb-Pb collisions at $\sqrt{s_{NN}} = 2.76$ TeV. *Phys. Rev.*, C92(5):054908, 2015.